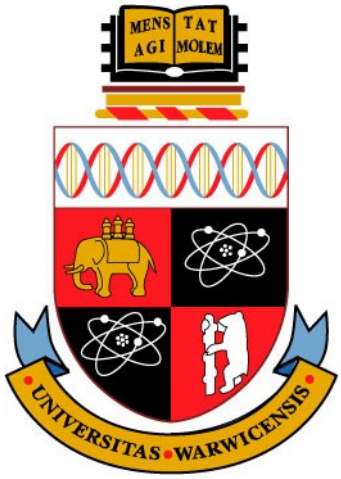

Studies of New Multiferroics

by

Ruth Agnes M^{c}Kinnon

Thesis

Submitted to the University of Warwick

for the degree of

Masters of Science (by research)

Department of Physics

September 2011

THE UNIVERSITY OF WARWICK

Contents

Acknowledgments

I would like to thank Geetha Balakrishnan, my supervisor, for all the help she has given me throughout my M.Sc. My thanks also go to Martin Lees for his guidance with the laboratory measurements and the work completed on the $Gd_{0.9}Lu_{0.1}MnO_3$ single crystal. I would also like to thank Tom Orton, Oleg Petrenko, Dean Keeble, Ravi Singh and Don McK.Paul as well as all the members of the Superconductivity and Magnetism group at the University of Warwick for their advice and assistance thought this past year.

Declaration

The work presented in this thesis was carried out by me, except where explicitly stated. All of the work took place between October 2010 and September 2011 and was carried out at the Department of Physics at the University of Warwick. The experimental data presented in Chapter 4 was collected from a $Gd_{0.9}Lu_{0.1}MnO_3$ single crystal previously grown and oriented by Da-qian Liao at the University of Warwick. All Rietveld refinements of the powder x-ray diffraction data were performed under the guidance of Dean Keeble.

Abstract

Research into multiferroicity has increased dramatically in recent years. A number of new rare-earth oxides have been shown to exhibit a coupling between magnetism and ferroelectricity. Following this area of research, the project investigates the multiferroic properties of $LuFe_2O_4$ and $Gd_{0.9}Lu_{0.1}MnO_3$ in single crystal form.

Multiferroic $LuFe_2O_4$ is a charge ordered ferroelectric which shows a coupling between magnetisation and electric polarisation near room temperature. In order to investigate how sample preparation and crystal growth environment affect final stoichiometry in $LuFe_2O_4$, two single crystals of the rare-earth oxide were grown using the floating zone method. Single crystals of different oxygen stoichiometry were prepared by altering the ratio of the CO_2/CO gas atmosphere used during single crystal growth. The magnetic and electric properties of the oriented single crystals and polycrystalline sample were investigated by measuring the magnetisation, dielectric constant and polarisation in zero and applied magnetic fields. A paramagnetic to ferrimagnetic ordering of the Fe moments along the *c*-axis was observed below 250K in both single crystals and the polycrystalline sample. The presence of this transition in the polarisation data confirms the multiferroic nature of the $LuFe_2O_{4-\delta}$ samples. A magnetostructural transition was also observed below 200K in the polycrystalline sample and the single crystal grown in the CO_2/CO=5 gas atmosphere. The absence of this transition for the single crystal grown in the CO_2/CO=3 gas atmosphere is an indication of poor oxygen stoichiometry within this crystal. A ferroelectric state was observed in the polycrystalline and single crystal samples below 280K. The temperature of ferroelectric transition observed for the $LuFe_2O_{4-\delta}$ samples is lower than the ferroelectric 2D to 3D charge ordering temperature reported in the literature.

Doping at the rare-earth site of the orthorhombic manganites is an effective method for tuning the average Mn-O-Mn bond angle. By adjusting the distortion of the MnO_6 lattice a multiferroic ground state can be induced in a series with a non-multiferroic parent compound. The effect of Lu-doping on the magnetic and electric properties of $GdMnO_3$ has been investigated. Heat capacity, magnetisation, dielectric constant and

polarisation data have been collected from an oriented single crystal of $Gd_{0.9}Lu_{0.1}MnO_3$. Due to the close proximity of $Gd_{0.9}Lu_{0.1}MnO_3$ to multiferroic $TbMnO_3$ in the spin ordering phase diagram a series of features below the incommensurate (IC) antiferromagnetic (AF) ordering temperature, not present in $GdMnO_3$, have been observed in the zero and applied magnetic field experimental data. The absence of a canted A-type AF state below this transition, normally present for the parent compound, and the persistence of a ferroelectric state in magnetic fields applied along the *a* and *b*-axis allow for the suggestion of a new magnetically ordered ferroelectric state, influenced by the ordering of the Gd moments, to occur in $Gd_{0.9}Lu_{0.1}MnO_3$.

Chapter 1

Introduction

The intrinsic coupling between magnetic interactions and the motion of electric charges, two phenomena though to be independent of each other because of their seemingly different origins, was first postulated by James Clerk Maxwell in 1865. The search for materials in which magnetism and ferroelectricity coexist is driven by the prospect of controlling charges by applied magnetic fields and spins by applied voltages [1]. Exploitation of the coupling between these primary order parameters may lead to the development of new multifunctional storage components for microelectronics [2]. The ferroelectric component of many of these materials is already in use in many modern electric devices such as filtering devices and high-performance insulators [3]. In recent years, a number of new rare-earth oxides have been shown to exhibit this type of coupling. Following this area of research, the project investigates the properties of some of these materials in single crystal form.

1.1 Multiferroics

A material that exhibits two or more primary ferroic properties such as ferromagnetism, ferroelectricity, ferroelasticity or ferrotoroidicity is described as a multiferroic. This definition was originally proposed by Schmid in an effort to characterise materials and the effects that allow the formation of switchable domains [4, 5]. All of the primary ferroics described form small regions of order, known as domains, within the material. Domains of different orientation are separated by domain walls. Application of an appropriate field, such as a magnetic field on a magnetic material, can cause the domains to align [6]. The term multiferroic is more commonly associated with magnetic ferroelectrics, examples of which are investigated within this thesis.

The ability to combine magnetic and ferroelectic properties within one material and the potential functionality that can be achieved has resulted in much of the early work on multiferroics being concentrated within magnetic ferroelectrics [7]. Combining these two properties has, however, proven to be difficult. Normally, these two order parameters are mutually exclusive; yet a number of materials have simultaneously presented magnetic and ferroelectric properties. Coupling of the parameters within the multiferroic system tends to be weak. The microscopic mechanisms of magnetism and ferroelectricity are very different from each other therefore do not strongly interfere [1].

The exclusivity between magnetism and ferroelectricity and the microscopic conditions required for the coupling of these different degrees of freedom can be explained using the symmetry requirements shown in Fig 1.1. The magnetic moment within a ferromagnet, depicted as a charge tracing an orbit, is unchanged under spatial inversion, however, the direction of the orbit and therefore the magnetic moment changes under time inversion. The opposite is true for a ferroelectic. Considering a ferroelectric material as a positive point charge lying asymmetrically in a crystal unit cell, spatial inversion reverses the polarisation while time inversion has no effect. A multiferroic shows no spatial or time invariance [8].

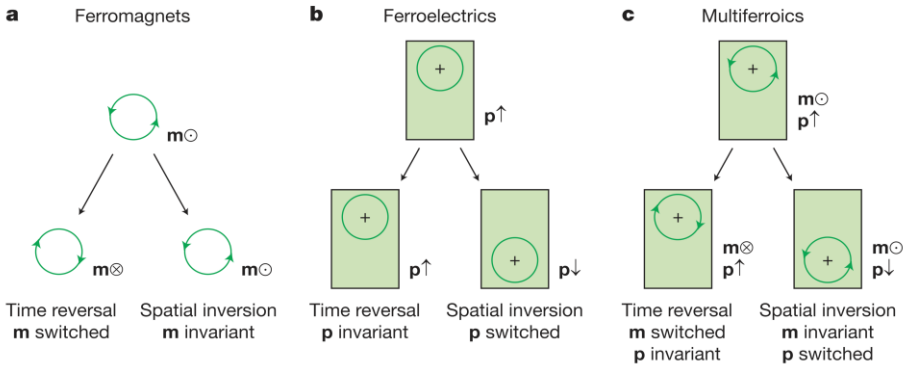

Fig. 1.1: The time-reversal and spatial-inversion symmetry in (a) Ferromagnets, (b) Ferroelectrics and (c) Multiferroics.[8]

A problem when trying to create a new multiferroic material is that multiferroics do not follow one specific theory [9]. The microscopic nature of magnetic ordering is well understood and generally follows the same principles as all insulating magnetic materials [7]. A material will possess a magnetic moment if it contains transition metal or rare earth ions with partially filled d or f electron shells. Ions with full shells are non-magnetic as the spins of the electrons add to zero so do not participate in the magnetic ordering. Long-range magnetic ordering within the material occurs as a result of exchange interactions (virtual hopping of electrons) between the partially filled d shells of different ions [1]. The type of ordering (i.e. ferromagnetic, antiferromagnetic) is dependent on the form of the exchange [6]. The theory of ferroelectricity on the other hand is not as well defined; a number of different mechanisms and types of ferroelectric order exist, many of which are not all fully understood [7]. Most ferroelectrics are transition metal oxides containing transition metal ions with empty d electron shells. Traditionally, these materials become ferroelectric when the positively charged metal ions form covalent bonds with neighbouring negatively charged oxygen ions through the virtual hopping of electrons from the filled oxygen shells to the empty d shells. An electric polarisation is then induced within these materials as a result of a relative diplacment of cations and anions within the periodic crystal. Although magnetism and ferroelectricity share the same mechanism of electron exchange it is the contrast of empty and partially filled d or f electron shells that make the properties mutually exclusive [1]. Consequently, nearly every multiferroic material has to be studied in its own right. The theories defining the mechanisms within one multiferroic can ultimately be very different from the next [9].

Coupling between magnetic and electric degrees of freedom is not a new phenomenon. The induction of magnetisation by an electric field or of polarisation by a magnetic field has long been studied under the name 'magnetoelectric effect' [7]. The linear magnetoelectric coupling term α linking the magnetic and electric degrees of freedom is shown in the relation for the free energy of a material in an electric and/or a magnetic field,[10]

$$F(\mathbf{E}, \mathbf{H}) = F_0 - P_i^s E_i - M_i^s H_i - \tfrac{1}{2}\varepsilon_0\varepsilon_{ij}E_iE_j - \tfrac{1}{2}\mu_0\mu_{ij}H_iH_j - \alpha_{ij}E_iH_j$$

$$- \tfrac{1}{2}\beta_{ijk}E_iH_jH_k - \tfrac{1}{2}\gamma_{ijk}H_iE_jE_k - \ldots \qquad \text{(Eq. 1.1).}$$

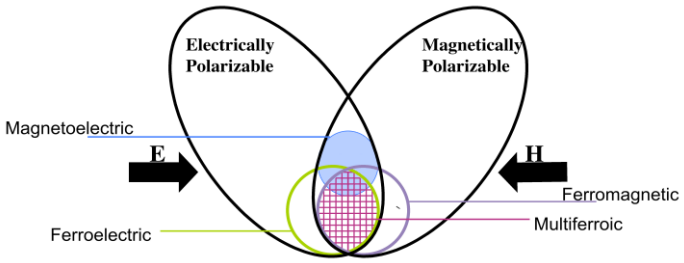

Fig. 1.2: Coupling between magnetic and electric degrees of freedom and the relationship between multiferroics and magnetoelectrics.[11]

A small group of multiferroics display this type of coupling (i.e. $\alpha \neq 0$). This overlap between the magnetoelectric effect and multiferroicity is not surprising as large magnetoelectic responses are expected within materials that display strong internal electromagnetic fields, often found within ferromagnets and ferroelectrics which display the largest magnetic susceptibilities and dielectric constants, respectively. Not all materials displaying the magnetoelectric effect are multiferroic, (Fig. 1.2), the material must break both spatial and time inversion symmetry in order to give a non-zero value for the magnetoelectric susceptibility tensor [10].

Multiferroics can be grouped in various ways according to different characteristics. One method is to classify the materials according to the mechanism that drives the ferroelectricity: proper and improper ferroelectrics (Table 1.1) [9].

Table 1 Classification of ferroelectrics

	Mechanism of inversion symmetry breaking	Materials
Proper	Covalent bonding between $3d^0$ transition metal (Ti) and oxygen	$BaTiO_3$
	Polarization of $6s^2$ lone pair of Bi or Pb	$BiMnO_3$, $BiFeO_3$, $Pb(Fe_{2/3}W_{1/3})O_3$
Improper	Structural transition 'Geometric ferroelectrics'	K_2SeO_4, Cs_2CdI_4 hexagonal $RMnO_3$
	Charge ordering 'Electronic ferroelectrics'	$LuFe_2O_4$
	Magnetic ordering 'Magnetic ferroelectrics'	Orthorhombic $RMnO_3$, RMn_2O_5, $CoCr_2O_4$

Table 1.1: Classification of multiferroics.[1]

In a proper ferroelectric, polarisation is a primary effect when inducing ferroelectricity; driven by hydridization and strong covalency or other purely structural effects. For example, the collective shift of anions and cations within a periodic lattice will give rise to a spontaneous and switchable polarisation. In an improper ferroelectric, polarisation is a secondary effect. Ferroelectricity is driven by an electronic degree of freedom such as spin, charge or orbital ordering producing polarisation as a by-product. The electronic order must lack inversion symmetry if ferroelectricity is to be induced. Magnetoelectric multiferroics are examples of improper ferroelectrics when a polarisation is induced by an internal magnetic field [1,9]. Another method of classifying different multiferroics is to group them according the origin of the magnetic and ferroelectric ordering: type-I and type-II. Within a type-I multiferroic, the two order parameters have different sources. Some coupling exists but the ferroelectric ordering temperature is generally higher than the magnetic one. Ferroelectricity within a type-II multiferroic occurs as a result of magnetic ordering. Strong coupling is expected between the two parameters as ferroelectricity sets in at the same temperature as magnetic ordering and is driven by it. Polarisation is typically smaller within this group [12].

1.2 RFe_2O_4

Crystals of the form RFe_2O_4 (R=Y, In, Sc and Dy to Lu) belong to the rhombohedral system with space group $R\bar{3}m$. Members of this group are described as having a hexagonally layered structure of alternating lattices stacked along the crystallographic *c*-axis, shown in Fig.1.3 [13]. The crystal structure can be separated in to two layers: W

and T. Each W layer is composed of two triangular bilayers of Fe^{2+} and Fe^{3+} ions; the coexistence of these ions creates a mixed valence state. The iron within this layer has fivefold oxygen coordination with a triangular bipyramid structure. The T layers separate the W layers with a single rare earth triangular lattice, where each rare earth ion is positioned in a distorted oxygen octahedron [14].

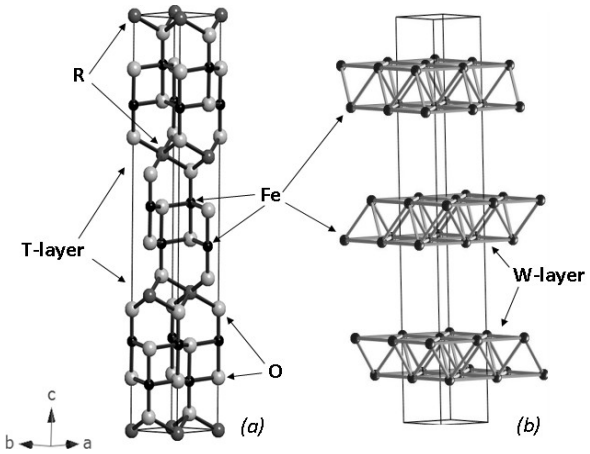

Fig. 1.3: (a) Crystal structure of RFe_2O_4 showing the R, O and Fe triangular layers stacked along the c-axis. (b) The W layer: Fe^{2+}/Fe^{3+} honeycomb. [2]

Ferroelectricity is induced within the RFe_2O_4 group as a result of charge ordering [12]. The general mechanism used to describe how ferroelectricity arises in this way is illustrated in Fig.1.4. Consider a homogeneous crystal represented as a neutral one-dimensional chain, shown in Fig.1.4(a). If the sites become inequivalent, shown in Fig.1.4(b), site-centred charge ordering occurs. Often, a checkerboard charge ordering of transition metal ions with different valencies, or the alternation of extra electrons or holes on a metal sublattice is presented. Alternatively, if the homogeneous crystal dimerizes, as shown in Fig.1.4(c), bond-centred ordering occurs. This type of ordering is commonly found within quasi-one-dimensional systems with partial electron occupation. Such systems are unstable with respect to the Peierls insability which creates a

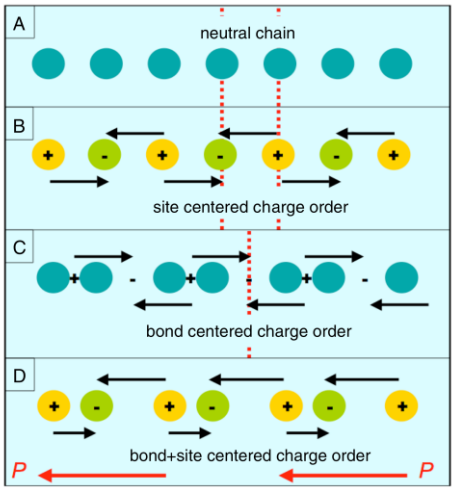

Fig. 1.4: (a) Homogeneous crystal, (b) site-centred charge ordering (c) bond-centred charge ordering and (d) Ferroelectric crystal. The red dashed lines mark the position of the mirror planes and the red arrows indicate the direction of the polarisation.[12]

spontaneous dimerization of the atoms known as a Peierls distortion. Within these systems the sites remain equivalent but the dimerization creates an alternate series of strong and weak bonds, the stronger bond having higher electron density. Site- and bond-centred ordering are both centrosymmetric therefore do not break spatial inversion symmetry. No net dipole moment forms within the two systems, which is made explicit by the presence of mirror planes. Ferroelectricity can only arise when both types of charge order occur simultaneously. Inversion symmetry is broken in this case and each molecule, shown in Fig.1.4(d), develops a net polarisation [7, 12].

Traditionally, charge order induced ferroelectricity arises from the ionic displacement of anions and cations within the crystal lattice, typically observed in multiferroics such as $BaTiO_3$ [12]. This type of charge ordering does not occur in RFe_2O_4. Ferroelectricity within the mixed valence RFe_2O_4 is associated with electron correlations between the iron ions. Charge ordering within the Fe lattice arises from the repulsive property of electrons acting on a frustrated geometry rather than the displacement of ions [3]. RFe_2O_4 is classified as an improper ferroelectric and a type-I multiferroic [1, 12].

The layered structure in RFe_2O_4 gives the system a two-dimensional character. The spin or charge coupling of irons within the *a*-*b* plane is stronger than along the *c*-axis which brings about an anisotropic ordering of the spin and charge. The charge ordering in RFe_2O_4 originates from a charge frustration within the W layer [14]. The usual checkerboard Fe^{2+}/Fe^{3+} is not favourable within this system as a result of the frustrated nature of the triangular iron lattice [12]. Frustration arises when it is not possible to satisfy all the interactions in a system to find a ground state [6]. A two-dimensional hexagonal lattice showing spin and charge frustration is illustrated in Fig.1.5. Arrangement of an equal number of $Fe^{2+}$and Fe^{3+} leads to frustration of the common nearest-neighbour site

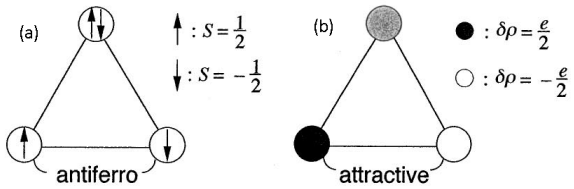

Fig. 1.5: (a) spin frustration and (b) charge frustration on a two-dimensional hexagonal lattice.[15]

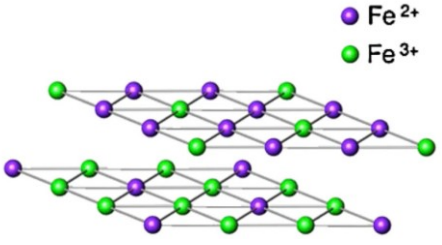

Fig. 1.6: Honeycomb lattice showing Fe^{2+}rich and Fe^{3+} rich bilayers.[16]

of a Fe^{2+}-Fe^{3+} pair. This frustration means that the ground state of the system tends to be degenerate, represented by the grey site in Fig.1.5(b) [15]. It is not possible to create a single unique ground state within these frustrated systems, however, by having a variety of similar low energy states the instability of a non-minimization of energy can be reduced [6]. Since the energy of the ground state is completely degenerate, the spin ordering process is also affected as there is no preference of↑ or ↓ spin at the common nearest-neighbour site in an antiferromagnetic system, shown in Fig.1.5(a)[15]. A polar charged state is stabilized by dividing the bilayers, in each W layer, into a $Fe^{2+}$and Fe^{3+} rich layer. The rare $Fe^{3+}$and Fe^{2+} ions in each bilayer are located at the centre of the $Fe^{2+}$and Fe^{3+} honeycombs (Fig.1.6) [16]. The charge ordered unit cell is depicted in Fig.1.7, this supercell is called a $\sqrt{3}$ x $\sqrt{3}$ structure [3].

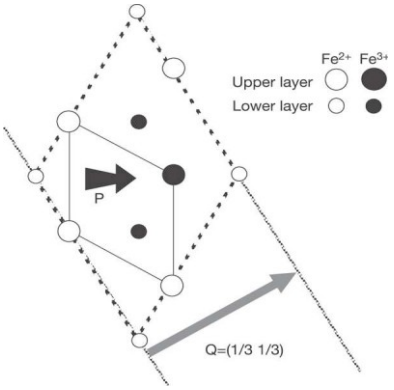

Fig. 1.7: Chemical unit cell and $\sqrt{3}$ x $\sqrt{3}$ superlattice cell marked by solid and dotted lines, respectively. Arrows indicate the direction of the polarisation P and wave vector Q showing the charge wave.[3]

RFe_2O_4 materials show a strong uniaxial magnetic anisotropy with the easy axis along the *c*-axis. The ferrimagnetic ordering of the $Fe^{2+}$and Fe^{3+} ions originates from the fivefold oxygen coordination with the Fe lattice [14]. The Fe^{2+} ions within the system have a large orbital moment and align ferromagnetically with each other. The Fe^{3+} ions have a negligible orbital moment. The overall spin alignment of the Fe triangular lattice is determined by the competition between Fe^{2+}-Fe^{3+} double exchange and Fe^{3+}-Fe^{3+} superexchange interactions [16]. Double exchange interactions favour ferromagnetic order whereas superexchange favours antiferromagnetic order [6]. Consequently, a 1:2 ferrimagnetic spin order, where one Fe^{3+}spin is parallel and the other two spins are antiparallel to the ferromagnetic Fe^{2+} spin, is expected. Two possible spin structures result from these spin alignments: the parallel Fe^{3+} spin can either be in the Fe^{3+} rich plane or in the Fe^{2+}rich plan, illustrated in Fig.1.8 (a) and (b), respectively. X-ray magnetic circular dichroism (XMCD) experimental and theoretical spectra have shown to match well in the case of the parallel Fe^{3+} spin in the Fe^{3+} rich layer. Mössbauer

studies have also concluded that three distinguishable Fe^{3+} sites exist, one of which has an antiparallel spin alignment in the Fe^{3+} layer [16]. This spin structure can be explained by superexchange interactions between the Fe^{3+}-Fe^{3+} ions. Superexchange is defined as an indirect exchange interaction between non-neighbouring magnetic ions which is mediated by a non-magnetic ion positioned between the two magnetic ions [6]. In this example, oxygen is the mediating ion. Superexchange is favoured when there is a large overlap between Fe^{3+} and O orbitals. Consequently, the strength of the exchange is dependent upon the angle of the Fe^{3+}-0-Fe^{3+} bond. The Fe^{3+} ions in separate bilayers form a bonding angle of 97° to each other whereas Fe^{3+} ions in the same Fe^{3+} rich layer bond at an angle of 118°. The optimum bonding angle for superexchange is 180°, this is when the O 2p-orbitals and the Fe 3d-orbitals overlap head-on. Superexchange between the interlayer Fe^{3+} is weak as there is poor overlap of the orbitals where minimum overlap occurs at 90°. On the other hand, the bonding angle between the Fe^{3+} ions in the same bilayer is closer to the optimum value, superexchange is therefore dominant in this magnetic coupling and so the neighbouring Fe^{3+} ions align antiparallel [16].

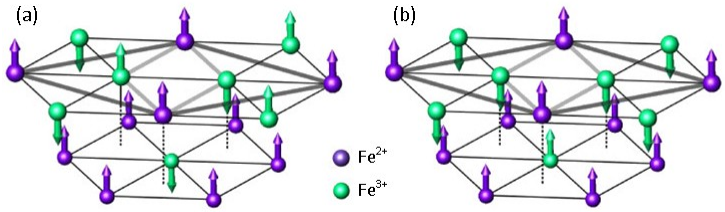

Fig. 1.8: Parallel Fe^{3+} spin in (a) Fe^{3+} rich bilayer and (b) Fe^{2+} rich bilayer.[16]

The RFe_2O_4 structure has an equal number of $Fe^{2+}$and Fe^{3+} ions which gives the iron W layer a nominal valence of +2.5. Applying the average valency to each Fe ion, the $Fe^{2+}$and Fe^{3+} ions behave as negative and positive charges. The weight centre of the $Fe^{2+}$and Fe^{3+} ions do not coincide in the unit cell of the superstructure, consequently the ordering of positive and negative charges indicates the presence of a local electric dipole within the W layer [14]. This indicated the possibility of ferroelectricity originating from the electron density modulation without a dipole of a cation and anion pair [3]. The charge frustration caused by the Fe ions acting as polar charges have already been shown in Fig.1.5(b): the black and white sites are of opposite charge, forming an attractive bond; the grey site is frustrated as it cannot form a similarly attractive bond with both of its nearest neighbours (the black and white sites) [15]. As well as indicating the presence of a polarisation within the W layer, application of the

average valency to each iron site allows for the spin structure shown in Fig.1.8(a) to produce the same diffraction pattern observed in neutron studies [16].

Extensive research into the multiferroic properties of $LuFe_2O_4$ began after the successful growth of a single crystal by Iida et al. [13]. A number of research groups (N. Ikeda [17], A.D. Christianson and M. Angst [18, 19, 20]) have published papers detailing the electronic ferroelectricity and magnetic phase transitions observed in $LuFe_2O_4$. Neutron diffraction experiments as well as ac magnetic susceptibility, dielectric constant and polarisation measurements have provided much information on the structural transitions which occur within the W layer.

IC 3-D CDW	2-D CDW	Disorder
320K	500K	

Table 1.2: Summary of charge order transition temperatures in $LuFe_2O_4$.[15]

$LuFe_2O_4$ has a rhombohedral structure with hexagonal lattice parameters: a=3.4406Å, c=25.28Å, α=β=90° and γ=120° [21]. Charge ordering within $LuFe_2O_4$ first occurs at 500K (Table1.2) [15]. At this temperature, a Bragg line indexed as (n/3 n/3 l), where n is an integer and l is a continuous value, appears in neutron diffraction data, indicating the formation of a two-dimensionally ordered state [3]. Above 500K, $LuFe_2O_4$ is in a state of disorder; all the Fe sites appear to have a charge of $2.5e^-$ caused by the thermal movement of the valence electrons [11]. The transformation of the Bragg line to Bragg spots in electron diffraction, indexed as (n/3 n/3 m+1/2) where m is also an integer, highlights the formation of a three-dimensional charge order below 330K [3]. The Bragg spots were the first indication of long range ordering of the $Fe^{2+}$and Fe^{3+} ions along the *c*-axis. Subsequent electron and non-resonant x-ray diffraction experiments detected the presence of lattice distortions emerging from the charge ordering leading to the development of the $\sqrt{3} \times \sqrt{3}$ superstructure [14].

$LuFe_2O_4$ has been found to undergo two first-order magnetic phase transitions; the first is a paramagnetic to ferrimagnetic ordering at 240K and the second is a magnetostructural transition at 175K. Neutron diffraction measurements by Christianson et al. [18] indicate that three-dimensional magnetic correlations exist below 240K. This work contradicted similar studies by Iida et al. [22] who previously reported a two-dimensional ferrimagnetic ordering below this temperature. The difference in quality of the $LuFe_2O_4$ single crystals is believed to cause this discrepancy

as strong sample dependent behaviour has been observed in other members of RFe_2O_4. For example, YFe_2O_4 exhibits three-dimensional magnetic order in stoichiometric samples and two-dimensional order in oxygen deficient ones [18]. The transition at 175K, first observed by Christianson et al. also coincides with a structural transition. Related systems, such as YFe_2O_4, have shown a transition with a structural component at similar temperatures [23]. Christianson et al. associated this transition to the formation of stacking faults at low temperature along the *c*-axis. The three-dimensional correlations in $LuFe_2O_4$ are sensitive to disruptions along the *c*-axis as the superexchange path between Fe-O bilayers consists of two mediating O ions [18].

Published results for the polarisation of $LuFe_2O_4$ along the *c*-axis show two main features: one at the three-dimensional charge ordering temperature and the other at the ferrimagnetic transition temperature [17]. The polarisation deceases at these transitions, (Fig.1.11). As previously discussed, charge order ferroelectrics exibit a spontaneous electric polarisation when electrons are transferred from anions to cations during the formation of a covalent bond. Ferroelectricity within $LuFe_2O_4$ does not arise from the displacement of anions and cations, consequently the polarisation has a very different nature from the typical displacement-type ferroelectrics. The charge frustration in $LuFe_2O_4$ creates a charge modulation within the Fe lattice which allows the polarisation to be considered as the density modulation of electrons on an average $Fe^{2.5+}$ cation. In this case, the cation does not have an associated anion [14]. A common feature of ferroelectrics is the switching of polarisation with external electric field. In $LuFe_2O_4$ the motion of ferroelectric domain boundaries causing this switching is believed to result from the collective motion of the electrons on the cation. This hopping of electrons between the $Fe^{2+}$and Fe^{3+} ions at the domain boundaries can also be used to explain the large low-frequency dielectric dispersion within $LuFe_2O_4$. The movement of electrons from $Fe^{2+}$to Fe^{3+} can be controlled by the application of an electric field, the frequency of the electron fluctuation coincides with the characteristic

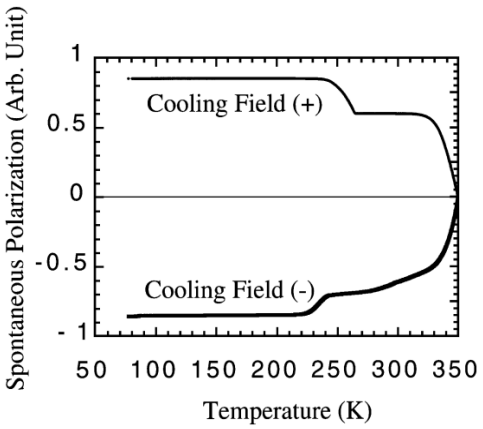

Fig. 1.11: Temperature dependence of electric polarisation along the *c*-axis of $LuFe_2O_4$ single crystal.[17]

time of the dielectric dispersion observed in the high temperature region [14]. The dielectric constant results for $LuFe_2O_4$ along the *c*-axis show the same features as the polarisation data: one at 330K and the other at 240K, this similarity shows the direct relation between dielectric constant and polarisability of the system [17]. The dielectric constant measured by Ikeda et al. perpendicular and parallel to the *c*-axis is shown in Fig.1.12.

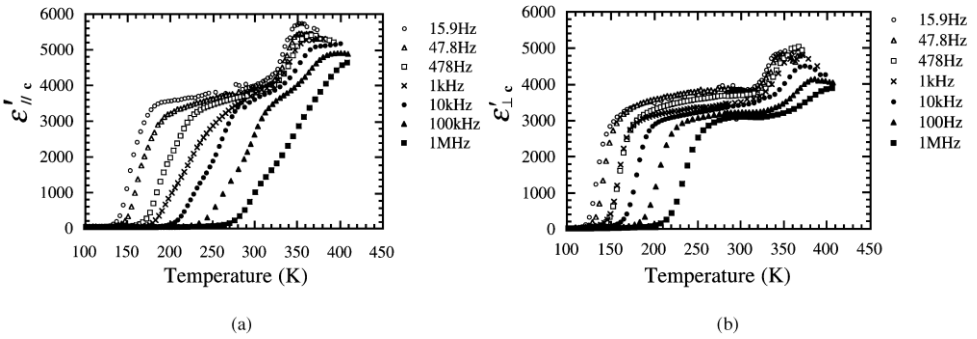

Fig. 1.12: Temperature dependence of dielectric constant measured (a) parallel and (b) perpendicular to the *c*-axis of $LuFe_2O_4$ single crystal.[17]

The features at the ferrimagnetic ordering temperature are thought to be caused by a direct coupling between the charge arrangement and the spin interactions of the iron ions through the superexchange mechanism. The unit cell of the electric polarisation is also the unit cell of the ferrimagnetic polarisation. This coupling demonstrates the multiferroic nature of $LuFe_2O_4$ [3, 14].

A collection of low temperature magnetic transitions exhibiting cluster glass characteristics have recently been observed. The glassy behaviour is attributed to the collective freezing of spins at a well-defined temperature. Cluster glasses results when the spins freeze to form large, ordered magnetic domains which dominate the magnetic behaviour [6]. The collective freezing of nanoscale pancakelike ferrimagnetic domains below 80K was first reported by Wu et al. [24]. D.c. magnetisation and a.c. susceptibility measurements conducted by Wang et al. [25] and Phan et al. [26] show the $LuFe_2O_4$ system entering a glassy state below 225K. In addition to the glass transition at 225K, Phan et al. have reported a change in the cluster glass phase below 170K and the formation of a kinetically arrested glass state below 55K. A phase diagram of the magnetic transitions observed in $LuFe_2O_4$ has been proposed by Phan et al. The

structural transition that occurs at 170K affects the size and distribution of the ferrimagnetic clusters formed at 225K, a new configuration of ferrimagnetic clusters are created altering the spin dynamics of the $LuFe_2O_4$ system.

In order to fully investigate the anisotropic properties of this system, high quality single crystals are required. Few papers have reported the full details of the gas environment used to grow single crystals of $LuFe_2O_4$. The floating zone method is the most common method of growth, however, single crystals of $LuFe_2O_4$ have also been grown by the travelling solvent floating zone method [25]. The single crystal grown by Iida et al. [13] used a gas mixture of CO_2 and H_2 in the heating stages of powder preparation followed by a CO_2/CO=2.5 atmosphere during single crystal growth. The 2D ferrimagnetic ordering observed in this crystal was reported by Iida et al. [22] in a later paper. The stoichiometry of this crystal was criticised by subsequent papers after the discovery of a second magnetic transition and a 3D charge ordering within $LuFe_2O_4$ [18]. The oxygen stoichiometry within $LuFe_2O_4$ can be controlled during growth by oxygen partial pressure tuned using a CO_2/CO mixture. Christianson et al. [18] have grown a number of single crystals using this method. A CO_2/CO ratio close to 2.7 was reported to produce the ideal stoichiometry. The ability to control oxygen stoichiometry with the growth atmosphere has recently been studied by Michiuchi et al. [27]. A series of single crystals of varying oxygen content were grown in gas mixtures of CO_2/CO=2, 4, 5, 6, 7 and 8. The method used to prepare the $LuFe_2O_4$ powders has not been specified. Michiuchi et al. report that the single crystal grown in the CO_2/CO=6 atmosphere has the closest to ideal stoichiometry. Polycrystalline samples of $LuFe_2O_4$ are typically sintered in either CO_2/H_2 or CO_2/CO gas mixtures. A single crystal showing magnetic properties indicative of stoichiometric $LuFe_2O_4$ has been grown by Kim et al. [28] from powders sintered in a CO_2/CO atmosphere. Single crystal growth papers, in general, give very little information about this stage.

Despite the large volume of literature available for $LuFe_2O_4$ there is a general absence of magnetisation, dielectric constant and polarisation data on single crystals along the *a*, *b* and *c*-axes in zero and applied magnetic fields.

1.3 Orthorhombic $RMnO_3$

Multiferroic behaviour within the orthorhombic manganites was first reported by Kimura et al. [29] in 2003. A gigantic magnetoelectric and magnetocapacitance effect attributed to the switching of the electric polarisation induced by magnetic fields was initially reported in $TbMnO_3$. The discovery of spin driven ferroelectricity within this group has sparked a surge in research into understanding the fundamental mechanism of multiferroic behaviour and the development of new multiferroic materials [30].

The heavy rare-earth orthorhombic manganite $RMnO_3$ series, where R=La-Dy, are described as having a distorted perovskite structure [31]. $LaMnO_3$ has a nearly ideal ABO_3 structure with a perovskite tolerance factor close to unity. In this simple structure, each Mn^{3+} ion is surrounded by six O^{2-} ions forming a MnO_6 octahedra. The replacement of La with rare-earths of a smaller ionic radii leads to a successive increase of the orthorhombic distortion, accompanied by a decrease of the Mn-O-Mn bond angles and an increase of the buckling and tilting angles of the MnO_6 octahedra in a $GdFeO_3$-type distortion [32].

The $RMnO_3$ series exhibit a Jahn-Teller (JT) type orbital order at temperatures well above 700K [31]. The orbital order is achieved by a JT distortion of the crystal lattice, illustrated in Fig.1.14. The octahedral MnO_6 structure is distorted by splitting the Mn^{3+} electron energy levels to achieve a lowering of the overall energy of the system. Mn^{3+} can be described as a JT ion. The number of unpaired electrons within the system is important. For example, Mn^{4+} has one more electron than Mn^{3+} but is not a JT ion as there is no net lowering of the electronic energy by a

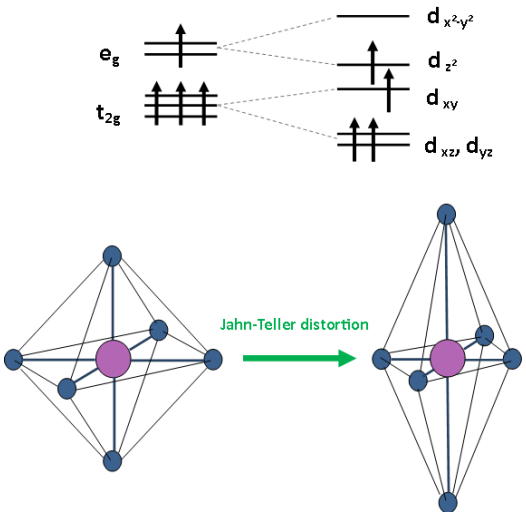

Fig. 1.14: Jahn-Teller distortion of an Mn^{3+} octahedral complex. Splitting of the singly occupied e_g level lowers the overall energy of the system.[6]

distortion [6]. The electron distribution within a JT type orbital order is point symmetric and carries no electric dipole moment. Consequently, any ferroelectricity within $RMnO_3$ cannot be directly due to this superimposed orbital order. The electric polarisation must originate from another form of charge ordering [32]. Ferroelectricity within $RMnO_3$ is therefore regarded as a second order effect [30]. $RMnO_3$ is classified as an improper ferroelectric and a type-II multiferroic [1, 12].

The magnetic phase diagrams for $RMnO_3$ as a function of in-plane Mn-O-Mn bond angle and rare earth ionic radius are shown in Fig. 1.15 (a) and (b), respectively. The rare-earth manganites with larger ionic radii, R=La-Sm, exhibit only one magnetic transition after the disordered-to-ordered magnetic phase. A paramagnetic to A-type antiferromagnetic (AF) ordering occurs above 50K. At this temperature, an anisotropic superexchange interaction occurs [31]. The JT type ordering of the Mn^{3+} orbitals results in a ferromagnetic spin ordering along the *a*-*b* plane and an AF ordering along the *c*-axis [1]. The transition temperature decreases as the radius of the rare-earth decreases. Smaller rare-earths at the R-site cause a decrease the Mn-O-Mn bond angle which increases the tilting of the MnO_6 octahedra, weakening the A-type AF ordering [32].

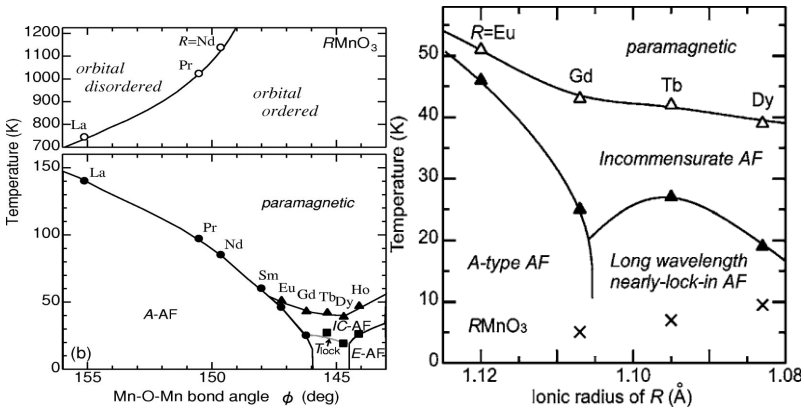

Fig. 1.15: The orbital and spin ordering temperatures of $RMnO_3$ as a function of (a) in-plane Mn-O-Mn bond angle[31] and (b) rare earth ionic radius[33].

The rare-earth manganites with the smallest ionic radii, R=Tb and Dy, do not show an A-type AF ordering in zero magnetic field. $TbMnO_3$ and $DyMnO_3$ show a paramagnetic to incommensurate (IC) AF transition around 40K followed by a long wavelength nearly locked-in AF transition below 28K [31, 33]. The IC and locked-in AF states have a sinusoidal and spiral spin-density wave ordering, respectively [1]. The spin states are

depicted in Fig.1.16. A ferroelectric state is induced within both manganites at the lock-in temperature. The magnetoelectric phase diagrams proposed by Kimura et al. [33] for $TbMnO_3$ and $DyMnO_3$ in different magnetic field are show in Fig.1.17 (i) and (ii), respectively. In zero and weak fields, both manganites have an electric polarisation along the *c*-axis. A polarisation flop from the *c*- to *a*-axis occurs for high magnetic fields. Ferroelectricity in $TbMnO_3$ vanishes when high magnetic field are applied along the *c*-axis. The system then undergoes a transition from the IC state to an A-type AF state.

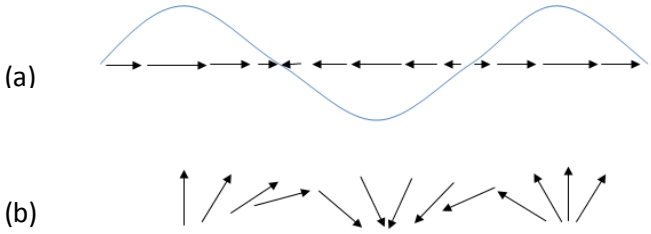

Fig. 1.16: Incommensurate (a) sinusoidal and (b) spiral magnetic ordering.[10]

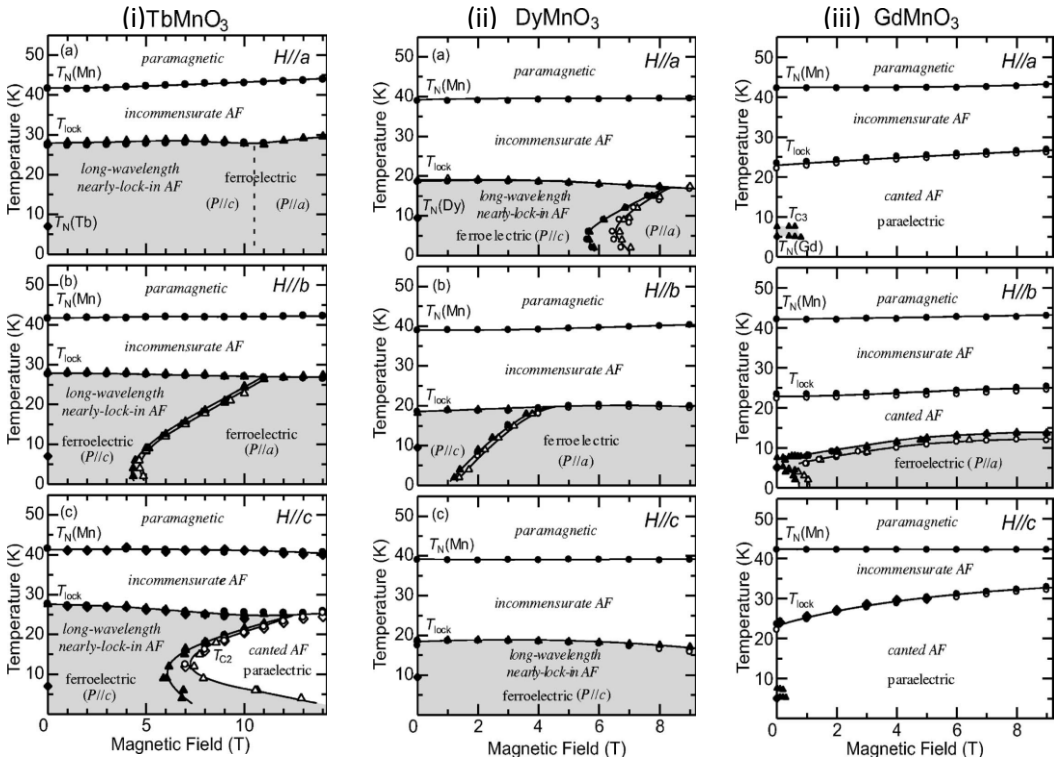

Fig. 1.17: The magnetic phase diagram of (i)$TbMnO_3$, (ii) $DyMnO_3$ and (iii)$GdMnO_3$ as a function of magnetic field. External fields applied parallel to the (a) *a*, (b) *b* and (c) *c* -axes.[33]

$ErMnO_3$ and $GdMnO_3$ are positioned at the boundary of a number of different magnetic phase transitions [31]. Both manganites show a paramagnetic to IC AF transition, followed by an IC to A-type AF ordering. $GdMnO_3$ is also in close proximity to the IC AF-lock-in AF transition which occurs in $TbMnO_3$ and $DyMnO_3$. When a magnetic field is applied along the *b*-axis, $GdMnO_3$ enters a ferroelectric state with an electric polarisation along the *c*-axis. An A-type AF to locked-in AF transition occurs at this temperature. The magnetoelectric phase diagram proposed by Kimura et al. for $GdMnO_3$ is shown in Fig.1.17(iii).

The change in magnetic structure from an A-type ordering to an IC state within the $RMnO_3$ series occurs as a result of the structural distortions created by the decrease of ionic radii at the rare-earth site [34]. The buckling and tilting of the MnO_6 octahedra shortens the distance between the O(2) and O(4) sites, shown in Fig.1.18. This shortening enhances the weak superexchange interactions along Mn- O(2)-O(4)-Mn exchange path between next-nearest-neighbour Mn sites. The distortion, along with the staggered JT orbital order creates inequivalent Mn sites within the *a*-*b* plane. The interaction between the Mn(1) and Mn(3) sites (positioned along the *b* axis) is stronger than that between the Mn(2)-Mn(4) sites (positioned along the *a*-axis). An AF exchange is induced along the *b*-axis weakening the effective ferromagnetic *a*-*b* axes interactions in the A-type AF structure. The simple ordering becomes frustrated and a complex spin state ensues [31]. Frustration, in its basic sense, induces spatial variations in the magnetisation and is often IC with the period of the crystal lattice [1]. When the next-nearest-neighbour AF exchange becomes comparable in strength to the nearest-neighbour ferromagnetic exchange, in the case of Er, Gd, Tb and Dy, a longitudinally modulated sinusoidal structure is stabilized within the system. $TbMnO_3$ and $DyMnO_3$ experience a locking-in of the AF ordering below 28K forming a magnetically transverse spiral state. This state is accompanied by the onset of ferroelectricity [1].

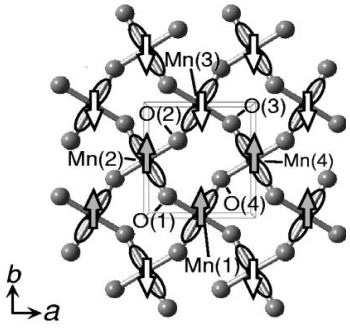

Fig. 1.18: A distorted MnO_6 octahedral lattice showing the position of the Mn (1), (2), (3) and (4) and O(1), (2), (3) and (4) sites.[31]

The on-set of ferroelectricity is connected to the change of the magnetic structure from a collinear sinusoidal modulation to a non-collinear spiral modulation [32]. Non-collinear spin ordering is favoured by Dzyaloshinskii-Moriya (DM) interactions (Fig.1.19) [1]. The exchange interaction occurs between the excited and ground states of neighbouring Mn^{3+} ions. The excited state is not connected to the ground state through a mediating ion, in the case of superexchange, but through a spin-orbital interaction. DM interactions often provide a small canting of the magnetic spins in an AF structure, resulting in weak ferromagnetism [6]. In $TbMnO_3$ and $DyMnO_3$, DM interactions push the negative O^{2-} ions in one direction perpendicular to the spin chain formed by positive Mn^{3+} ions staggering the orbital order. The symmetry of the spiral state therefore allows for an electric polarisation, which has a sign coupled to the direction of spin rotation. The spiral state breaks time inversion symmetry by inverting the direction of spin rotation when the sign of all the coordinates are reversed [1]. A multiferroic state can therefore be achieved within some rare-earth manganites.

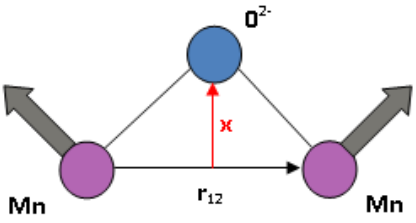

Fig. 1.19: Dzyaloshinskii-Moriya interaction mechanism. The sift in oxygen, x, from the r_{12} unit vector describes the degree of inversion symmetry breaking at the oxygen site.[1]

Ferroelectric order can be induced or suppressed within the rare-earth manganites positioned near different magnetic phase boundaries. External magnetic fields applied along different crystallographic axes appear to move the position of the boundaries (Fig.1.17) [33]. In the case of $TbMnO_3$, a magnetic field applied along the *c*-axis suppresses the ferroelectric state by expanding the A-type AF phase region and shifting the boundary between the A-type AF ordering and the locked-in AF ordering to the right. $DyMnO_3$ is positioned far from this boundary, yet a very large field (H>14T) applied along the *c*-axis suppresses the ferroelectric state by inducing an A-type AF phase. In the case of $GdMnO_3$, weak fields applied along the *b*-axis have induced a ferroelectric state by suppressing the A-type AF phase. A very large magnetic field along this axis may shift the A-type AF- IC AF and A-type AF-lock-in AF boundaries to the left resulting in $GdMnO_3$ having a similar magnetic phase diagram to $TbMnO_3$ [33].

Doping at the rare-earth site can modify the multiferroic properties of the heavy rare-earth manganites. The average radius of the rare-earth site and the parameters related to the Mn-O-Mn bond angle can be continuously adjusted with dopant content

permitting a gradual control of magnetic and electric ground states [35]. A multiferroic state can be generated within manganites that have previously shown no ferroelectricity through substitution at the R-site. Doping at the R-site with smaller ions increases the Mn-O-Mn bond angle. Manganites that are positioned near the spiral magnetic phase boundaries have been found to enter this phase when doped with smaller ions. For example, a ferroelectric state can be induced within $EuMnO_3$ when it is doped with Y. $GdMnO_3$ has also been found to enter a ferroelectric state in zero magnetic field when doped with Y. The doping level required to induce ferroelectricity within $EuMnO_3$ is higher than that needed for $GdMnO_3$. Ivanov et al. [35] report a transition from the IC phase to the locked-in AF ferroelectric state when x≥0.3 for $Eu_{1-x}Y_xMnO_3$ and y≥0.05 for $Gd_{1-y}Y_yMnO_3$.A PhD thesis reporting the effect of doping with Y at the rare-earth site of $SmMnO_3$ and $GdMnO_3$ has recently been completed by D. O'Flynn in the Superconductivity and Magnetism Group at the University of Warwick [10]. The work carried out by O'Flynn was originally motivated by the discovery of a multiferroic state within $R_{1-x}Y_xMnO_3$ (R=Eu, Gd) by groups such as Ivanov et al. [35]. $SmMnO_3$, in its pure form, is a paraelectric which exhibits a commensurate A-type antiferromagnetic order below 58K (Fig.1.15) [31]. A significant change in the magnetic properties of $SmMnO_3$ and the onset of an electric polarisation along the *c*-axis were observed by O'Flynn when the parent compound was doped with Y. A multiferroic state was found to exist for $Sm_{1-x}Y_xMnO_3$ (x=0.4, 0.5). The phase diagram proposed by O'Flynn for Sm_{1-}

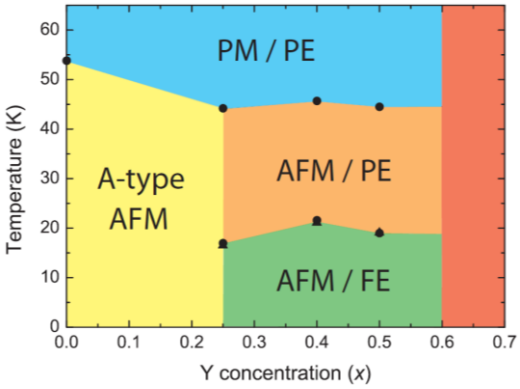

Fig. 1.20: Magnetoelectric phase diagram for $Sm_{1-x}Y_xMnO_3$ as a function of Y concentrated.[10]

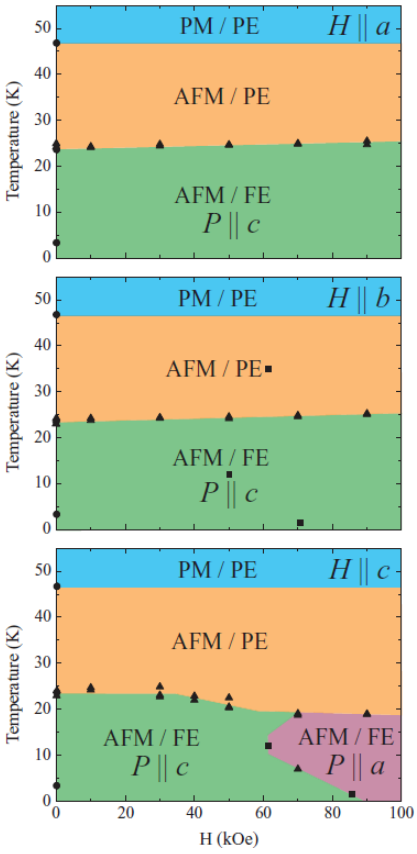

Fig. 1.21: H-T phase diagram for $Sm_{0.5}Y_{0.5}MnO_3$.[10, 36]

$_xY_xMnO_3$ compounds as a function of Y concentration is shown in Fig.1.20. Another phase diagram showing the magnetic field dependence of $Sm_{0.5}Y_{0.5}MnO_3$ is shown in Fig.1.21. In zero magnetic field, O'Flynn observed the electric properties of $Sm_{1-x}Y_xMnO_3$ (x=0.4, 0.5) to be very similar to that of $TbMnO_3$; in both cases the direction of the polarisation is observed along the *c*-axis. The magnetic field dependence, however, is markedly different. Both $Sm_{0.5}Y_{0.5}MnO_3$ and $TbMnO_3$ exhibit a flop from the *c*-axis to the *a*-axis in an applied magnetic field. The flop in the polarisation occurs when the field is applied along to the *b*-axis in $TbMnO_3$ or along the *c*-axis in $Sm_{0.5}Y_{0.5}MnO_3$. O'Flynn linked the magnetoelectric coupling observed within $Sm_{0.6}Y_{0.4}MnO_3$ and $Sm_{0.5}Y_{0.5}MnO_3$ to the alterations in the local structure of the MnO_6 octahedra, in particular the Mn-O-Mn bond angle, induced by a decrease in the rare-earth site volume [10, 36].

The effect of Y doping at the rare-earth site in $GdMnO_3$ was also investigated by O'Flynn [10]. Preliminary measurements on polycrystalline samples of $Gd_{1-x}Y_xMnO_3$ demonstrated a magnetoelectric coupling in x=0.1-0.4. A Mn-O-Mn bond angle close to that of $TbMnO_3$ was also found in $Gd_{0.8}Y_{0.2}MnO_3$. Further work on the $Gd_{1-x}Y_xMnO_3$ series is currently being carried out at the University of Warwick. O'Flynn's findings have further motivated the study of the new $Gd_{1-x}Lu_xMnO_3$ series within the Superconductivity and Magnetism group at Warwick.

Chapter 2

Experimental Methods

The experimental techniques used during sample preparation, single crystal growth and characterisation are described in this chapter. Laboratory measurements used to investigate the magnetic and electric responses of the samples are also detailed here. All measurements were carried out in the Department of Physics at the University of Warwick.

2.1 Sample Preparation

Polycrystalline samples were prepared by solid-state reaction from high purity powders. Stoichiometric ratios of the powdered oxides were mixed and finely ground before furnace heating. The high purity powder mixtures were heated in a gas atmosphere a total of three times. The period of each heating varied between 12 and 24 hours at temperatures up to 1200-1250°C. The loose powder mixtures were heated twice before being compacted into waterproof balloons and compressed isostatically in water at high pressure (>150kg cm^{-2}) to form rods for single crystal growth. The power mixtures, in the form of rods, were then heated for a third and final time.

2.2 Single Crystal Growth: Floating Zone Technique

Single crystals were grown by the floating zone method. This method requires two rods: a seed and a feed rod, for single crystal growth. Single crystals are grown in two and four mirror floating zone furnace, illustrated in Fig.2.1, by crystallization of the molten material on cooling. The feed rod is suspended above the seed rod inside a sealed quartz tube. Platinum wire, which is inert and has a high melting point, is used to suspend the feed rod. The wire allows the feed rod to adjust its position freely above the seed rod, which is fixed to the lower shaft. A molten zone is created between the feed and the seed rods by slowly melting the tips of the rods using heat from two/four halogen bulbs brought to a focus between two/four elliptical mirrors. The stability of the zone can be controlled manually by adjusting the power of the bulbs and vertical positions of the rods. The zone is suspended between the rods by the surface tension of the material. The rods are rotated in opposite directions in order to help homogenise both the temperature and the composition of the zone. Material at the base of the molten zone slowly cools onto the seed rod as the focus of the mirrors is moved upwards along the feed rod. The rate at which the mirrors are moved depends on the particular compound. Different gas atmospheres of pressures of up to 10 bars can be used for the crystal growth.

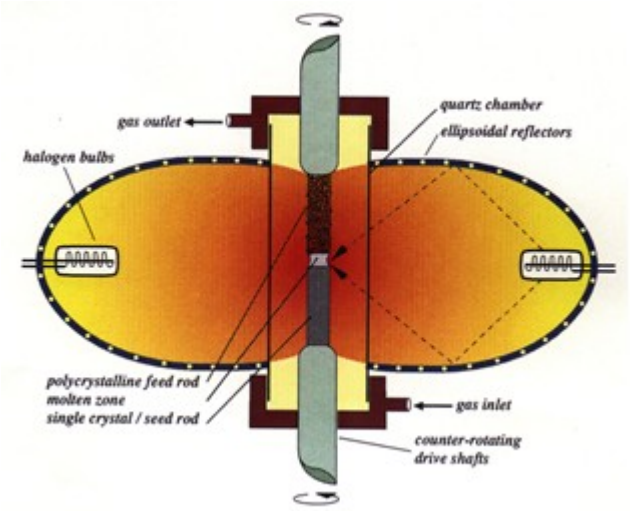

Fig. 2.1: Annotated schematic of a two-mirror floating zone furnace.

$LuFe_2O_{4-\delta}$ and $Gd_{0.9}Lu_{0.1}MnO_3$ single crystals were grown at the University of Warwick using the Crystal Sysytems Inc. F-ZT-10000-H-IV-VPS four mirror furnace and the Canon Machinery SC1MDD-11020 two mirror furnace, respectively. Crystal boules of up to 55mm in length and 5mm in diameter were grown using the floating zone method. The floating zone technique is best suited for the crystal growth of oxides and is particularly suited for the oxides used in the present study.

2.3 Powder X-ray diffraction

The phase formation and impurity levels of the synthesised samples were examined using powder X-ray diffraction. This process was performed at various stages throughout the sample preparation. The diffraction patterns were compared with published results to check for any possible impurity compounds and compounds with different stoichiometric ratios of the primary elements. The patterns were also checked for any phase changes that may have occurred at the different stages.

For powder x-ray diffraction, a beam of x-rays, of wavelength λ, are incident on the surface of the crystalline material at an incident angle θ, depicted in Fig. 2.2. The x-rays are scattered by the sample according to Bragg's law

$$n\lambda = 2d\sin\theta \qquad \text{(Eq. 2.1)}$$

where n is an integer and d is the distance between the crystal planes. When there is coherent scattering from the crystalline planes the Bragg condition is satisfied and a Bragg peak appears in the diffraction pattern.

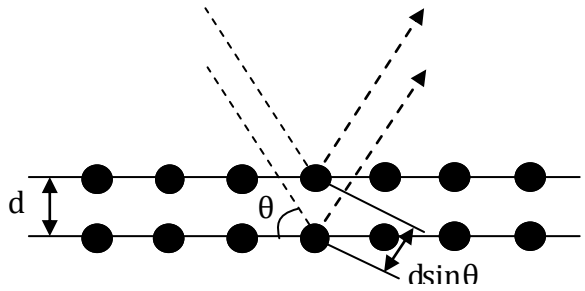

Fig. 2.2: Schematic of the Bragg condition showing scattering of X-rays by atoms in a crystalline solid.[6]

Two different X-ray diffractometers were used to record the patterns presented in this thesis: a Philips PW1720 X-ray generator, which uses Cu K_α radiation (λ~1.54Å); and a Panalytical X'Pert Pro multipurpose X-ray diffraction system, with monochromated Cu $K_{\alpha 1}$ radiation.

2.4 Laue X-ray diffraction

The quality of the single crystals and the orientation of their crystallographic axes were determined using Laue x-ray diffraction.

A crystal is placed within the diffractometer on a stationary triple-axis goniometer. A 'white' beam of x-rays are incident upon the crystal from the centre of a scintillator screen. The wide range of wavelengths in the incident beam allows the Bragg condition for each lattice plane to be satisfied by a different wavelength. The x-rays are then backscattered onto the screen, as depicted in Fig.2.3, where the image is recorded by a charge-coupled device, controlled by Image Pro Express software. The patterns obtained from the crystal are compared with those simulated from the crystal space group and lattice parameters of the material, using OrientExpress software. The crystal can be repositioned, to match the simulated pattern, using the goniometer which enables the precise rotation and translation of the crystal along three orthogonal axes.

Once the crystals are orientated, they are cut along the plane normal to the required axis using a low speed diamond saw.

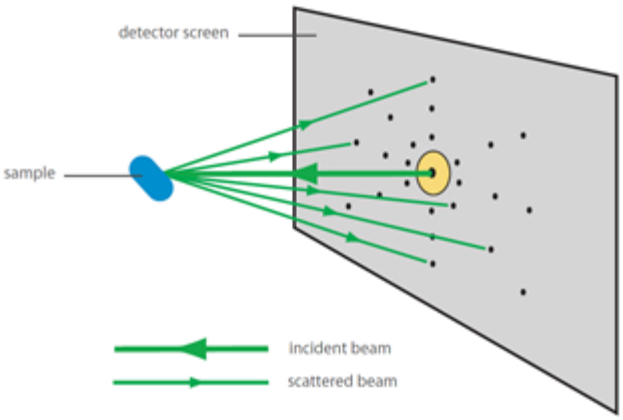

Fig. 2.3: Laue diffraction showing backscattering of X-rays from sample onto detector screen.[10]

2.5 Magnetisation

A Superconducting QUantum Interference Device (SQUID) magnetometer was used to measure the magnetic response of the samples at different temperatures and in different fields. The magnetometer comprises a SQUID attached to pick-up coils which sits inside a superconducting magnet. The sample is positioned within the pick-up coils

of the SQUID at the end of a non-magnetic sample rod, shown in Fig.2.4. The sample is held in alignment with GE (General Electric) varnish which is used to fix the sample to a non-magnetic tufnol holder. The magnetic response of the sample is determined by the SQUID magnetometer which measures the current generated in the pick-up coils as the sample is moved through the coils in a series of 32 steps. Movement of the sample through the pick-up coils induces a current proportional to the sample magnetisation; a magnetic moment value in electromagnetic units is fitted to the measured signal. Zero field-cooled (ZFC) and field-cooled (FC) data was collected while warming for both polycrystalline and oriented single crystals samples. For ZFC measurements the sample is cooled in zero field before a magnetic field is applied. For FC measurements, the sample is cooled in the applied field.

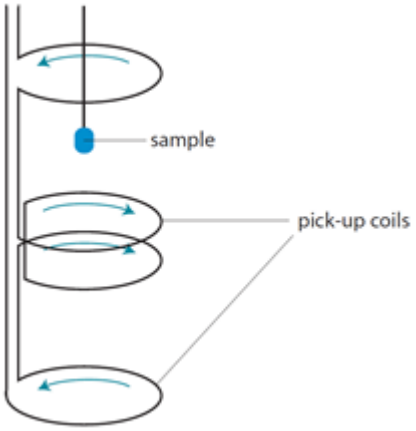

Fig. 2.4: Schematic of sample positioned within the pick-up coils of a SQUID magnetometer.[10]

The SQUID magnetometer used to collect the data for this thesis is a Quantum Design MPMS-5S. This system has a temperature range of 1.8-400K and a magnetic field range of up to ±50kOe.

2.6 Physical Properties Measurements System (PPMS)

The thermal and electrical responses of the samples at different temperatures and in a range of magnetic fields were measured using the PPMS. Heat capacity, dielectric constant and polarisation measurements were conducted using this system. The heat capacity measurement uses a different PPMS insert from the dielectric constant and polarisation measurements consequently sample preparation is different for the thermal and electrical measurements. The PPMS used to collect the data has a temperature range of 1.8-400K and a magnetic field range of up to ±90kOe.

2.6.1 Thermal Response

The thermal response of the sample was determined by measuring the heat capacity as a function of temperature. In order to avoid the effects of a thermal gradient and improve the accuracy of the measurement, the sample is required to be relatively thin (<1mm thick) and have a large surface area, ideally the same size as the 3x3mm^2 platform the sample is mounted on for the measurement. Apiezon N- grease is used to attach the sample to the platform, ensuring good thermal contact between the platform and the sample. A heater and thermometer are also attached to the platform which is suspended by wires from the middle of a 'puck', depicted in Fig.2.5. The wires connect the heater and thermocouple to the puck while isolating the platform from the effect of thermal contact with the outside system. By measuring the relaxation time of the sample after heating, the heat capacity at a particular temperature can be determined. The platform is heated at a constant rate until the system has reached a percentage increase of the set point (typically 5%). The heating power is then removed and the sample and platform cool exponentially back to the set temperature. In order to determine the heat capacity of the sample alone, contributions from the platform and grease are subtracted from the relaxation time by way of an addenda measurement. The addenda is the heat capacity of the platform and grease measured over the same temperature range required for the sample measurement. Heat capacity is a bulk measurement therefore samples can be either polycrystalline or single crystal for zero magnetic field measurements.

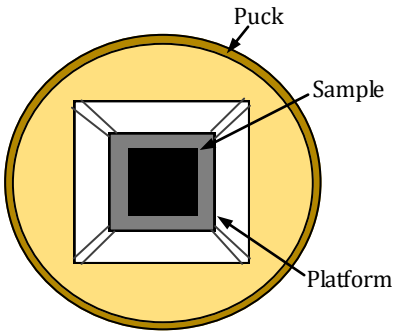

Fig. 2.5: Sample mounted on a PPMS sample 'puck' insert.[10]

2.6.2 Electrical Response

The electrical response of the sample was determined by measuring the dielectric constant and polarisation. Both of these measurements require the sample to be cut into orientated thin plates with their widest faces perpendicular to one of the *a*, *b* and *c*-axes. In order to reduce noise in the measurements the samples must be thin (<1mm thick) and have a relatively large surface area (>5mm^2). Electrical contacts are made by

attaching silver wire to the two parallel flat faces of the samples with silver paste (Du Pont 4929N conductor paste). These faces are sputtered with gold in order to provide good electrical contact between the wire and the sample. The samples are positioned within the sample space of the superconducting magnet at the end of a PPMS insert designed especially for these types of measurements, shown in Fig.2.6.

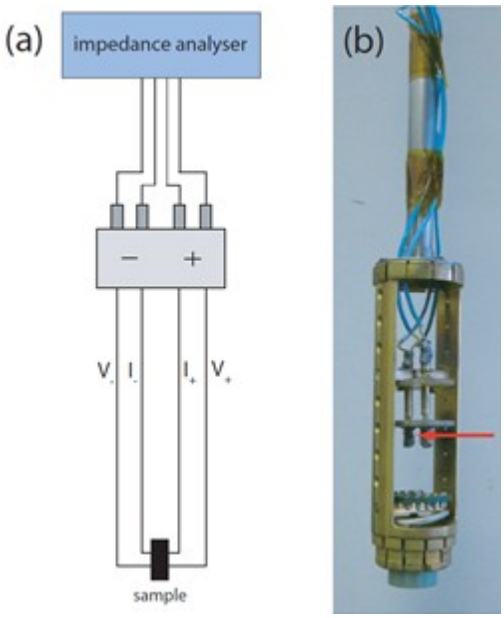

Fig. 2.6: PPMS insert used for electric response measurements, (a) schematic diagram and (b) image. The arrow marks the point where the sample is attached to the holder.[10]

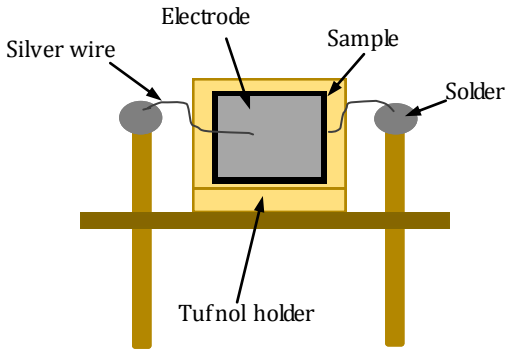

Fig. 2.7: Holder with sample mounted on a tufnol 'seat' used to orientate the sample in a magnetic field.

(i) Dielectric Constant

A material is referred to as a dielectric if it can be electrically polarised upon the application of an electric field.

The dielectric constant of a sample can be determined by measuring the capacitance of the material as a function of temperature. The capacitance, C, is related to the dielectric constant, ε_r, by the parallel plate capacitor expression

$$C = \varepsilon_0 \varepsilon_r A/d \qquad \text{(Eq. 2.2)}$$

where ε_0 is the permittivity of free space (8.854×10^{-12} Fm^{-1}), A is the area of the parallel electrodes and d is the distance between the electrodes. This expression requires the dielectric material, of known dimensions, to be inserted between two electrodes in the parallel plate arrangement illustrated in Fig.2.8 The contacts made with the parallel faces of the sample act as the electrodes; the area of the electrodes is therefore the same as the area of the sample face and the distance between the electrodes is equal to the sample thickness. The capacitance of the sample was measured using an Agilent 4294A impedance analyser connected to the PPMS sample insert.

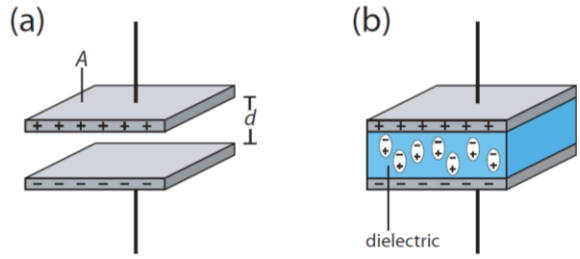

Fig. 2.8: Parallel plate capacitor arrangement showing electrodes separated by a (a) vacuum and (b) a dielectric.[10]

Dielectric constant data was collected for polycrystalline samples and for electric fields applied along the *a*, *b* and *c*-axes of single crystals. The effect of applying external magnetic fields of up to 90kOe along the individual crystallographic axes was also measured. Samples were initially field cooled: cooled down through the transitions of interest in a magnetic field. The capacitance as a function of temperature was then measured during heating at sweeping rates of 1 or 2K/min, depending on the material. In order to determine the dependence of the dielectric constant on the frequency of the electric field, the capacitance was recorded for 5, 10, 20, 30 and 40kHz fields using a LabVIEW programme.

The system was tested by measuring the dielectric constant of the well-known ferroelectric $BaTiO_3$. $BaTiO_3$ is characterised by a large temperature dependent dielectric constant. The capacitance of a single crystal of $BaTiO_3$ was measured during heating and cooling in zero magnetic field and compared with published data [37]. The results are shown in Fig.2.9. Features related to changes in the lattice structure were observed at the appropriate temperatures and the dielectric constant was found to be of the correct

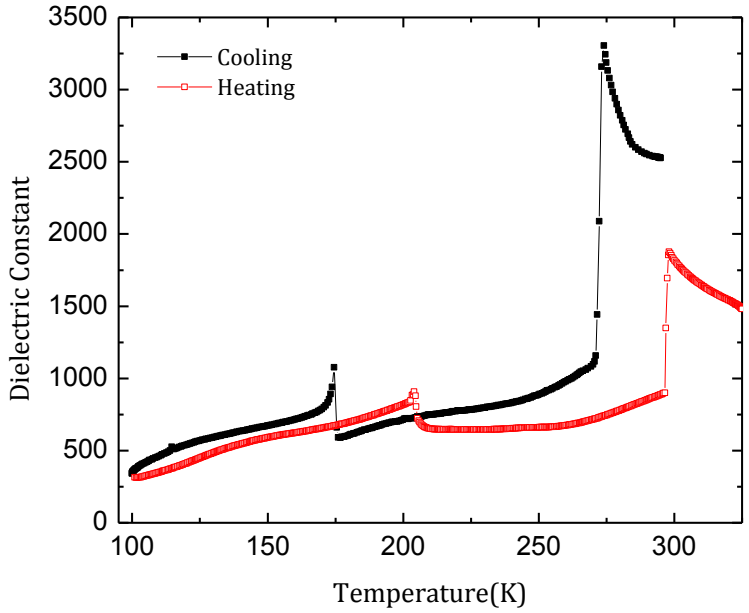

Fig. 2.9: Dielectric constant as a function of temperature for single crystal $BaTiO_3$ in zero magnetic field. Measured at 10kHz during cooling and heating.

order of magnitude. This test calibration was necessary as the dielectric constant for $LuFe_2O_{4-\delta}$ was very large at high temperature.

(ii) Polarisation

The spontaneous polarisation induced within a material as it enters the ferroelectric state can be estimated from an observed pyroelectric current. By integrating the recorded pyroelectric current, I, with respect to time according to the expression

$$P=\int(I/A)\,dt \qquad \text{(Eq. 2.3)}$$

where A is the area of the parallel electrodes, the polarisation as a function of temperature can be determined.

The samples were initially cooled from a temperature above the ferroelectric transition to a low temperature value. During cooling, the samples were poled in electric fields of 150 and 1000 V/mm, depending on the material. Before each measurement the high voltage was removed and the electrodes of the sample capacitor were short circuited through a bleed resistor for 30-60 minutes. Any surface charge built up during the application of the electric field was dissipated through the resistor allowing for a zero-charge state to be maintained. The pyroelectric current was measured during the heating

using a Keithley 6517A electrometer. The data was recorded as a function of temperature and time using a LabVIEW programme. The magnitude of the polarisation expected for the materials studied in this thesis are much smaller than those of standard ferroelectrics. The electrometer used to measure the pyroelectric current must have a very high sensitivity as changes in the signal as small as $0.1pA=10^{-13}A$ need to be detected.

The pyroelectric curves typically show a sharp anomaly at the ferroelectric transition temperature followed by a flattening of the signal above this temperature. Before integration, the pyroelectric current was corrected for background noise by making the current equal to zero above the transition temperature. This ensures that zero polarisation is calculated for the non-ferroelectric phase. The procedure used to obtain the polarisation from the pyroelectric current is outline in Fig.2.10.

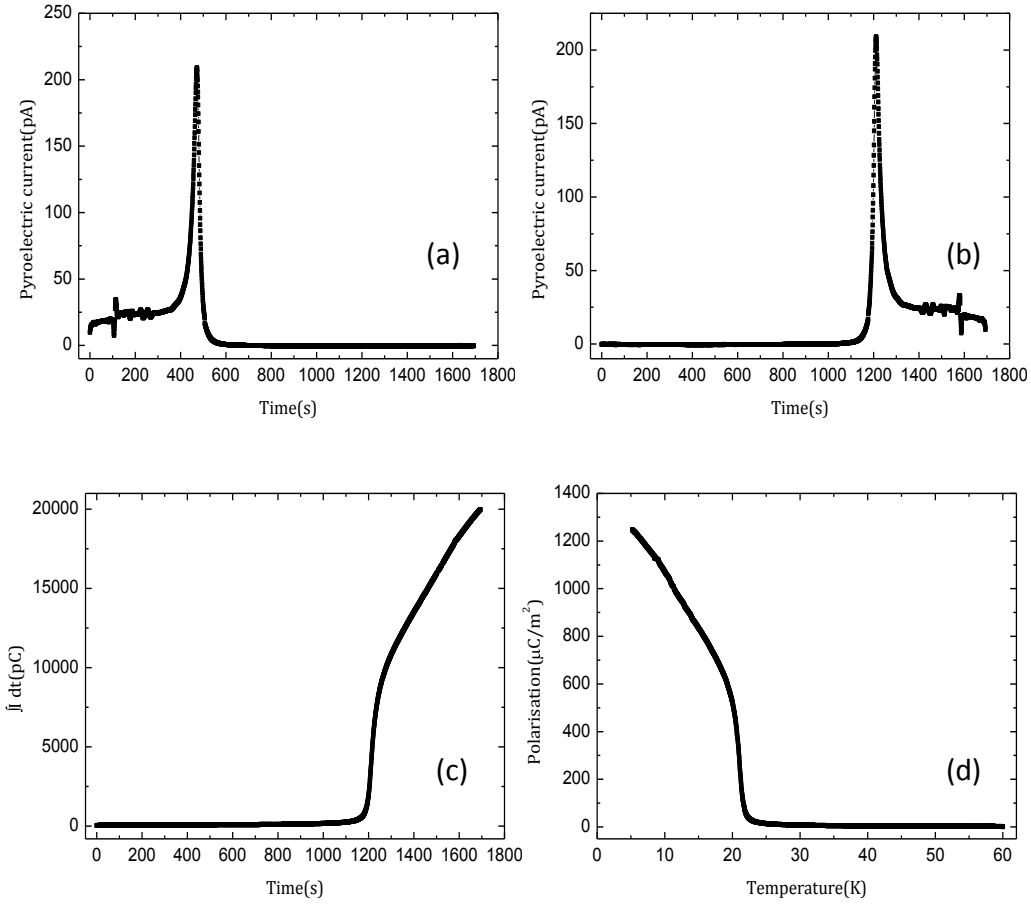

Fig. 2.10: Converting proelectric current into polarisation: (a) the recorded pyroelectric current as a function of time, (b) the pyroelectric current corrected for background current plotted with the time axis reversed, (c) the pyroelectric current integrated with respect to time and (d) the integrated current divided by the sample area, plotted as a function of temperature. The results were on a $Gd_{0.9}Lu_{0.1}MnO_3$ single crystal in a 90kOe magnetic field applied parallel to the *b*-axis.

Chapter 3

Multiferroic Properties of $LuFe_2O_4$

Multiferroic $LuFe_2O_4$ is a charge ordered ferroelectric which shows a coupling between magnetisation and electric polarisation near room temperature [3]. The potential applications of the giant magnetodielectric response observed within this material have resulted in an increase in research within this area [2]. $LuFe_2O_4$ is a well studied multiferroic compound; however, there are several properties that remain unreported in the literature. Magnetisation, dielectric constant and polarisation measurements have not been along the *a* and *b*-axes. Only one set of polarisation data has been reported for $LuFe_2O_4$, no other group have so far been able to reproduce this result. Finally, no magnetic and electric responses have been recorded in applied magnetic fields greater than 1kOe.

In this chapter, the effect of crystal growth environment on final crystal stoichiometry in $LuFe_2O_4$ is investigated. Two single crystals of the rare-earth oxide have been grown using the floating zone method. By altering the atmosphere in which they were grown, single crystals of different oxygen stoichiometry have been prepared. Powder x-ray diffraction and Laue x-ray diffraction have been used to determine the composition and quality of the samples. The multiferroic properties have also been investigated by measuring the magnetisation, dielectric constant and polarisation along the *a*, *b* and *c* crystallographic axes.

3.1 Sample Preparation and Crystal Growth

Polycrystalline powders of $LuFe_2O_{4-\delta}$ were synthesised from stoichiometric quantities of Lu_2O_3 and Fe_2O_3 (99.99%). In total, three batches of $LuFe_2O_{4-\delta}$ powder were prepared. Approximately 15g of material was produced from each batch. The procedure used for heating the powders is given in Table 3.1. After the second heating the powders were compressed into rods, as described in Section 2.1. The purpose of the third heating was to strengthen the rods in preparation for crystal growth. The same sequence of gas atmosphere, $CO_2/CO=5$, Ar then $CO_2/CO=5$, was used to prepare each batch. The only variation between batches was the period of the final sintering: the batch A was heated for 12 h whereas batches B and C were heated for 24 h. Single crystals of $LuFe_2O_{4-\delta}$ were grown using the floating zone method, as described in Section 2.2. In order to form single crystals of $LuFe_2O_{4-\delta}$, a slow growth of ~ 1 mm/h was used. Crystals were grown in two different CO_2/CO atmospheres: $CO_2/CO=3$ and $CO_2/CO=5$.

	Sintering Stage (Temperature, Time and Gas Atmosphere)			
Powder Batch	**1st**	**2nd**	**3rd(Rod)**	**Single Crystal Growth Atmosphere**
A	1200°C, 12h, $CO_2/CO=5$	1200°C, 24h, Ar	1250°C, 12h, $CO_2/CO=5$	$CO_2/CO=3$
B	1200°C, 12h, $CO_2/CO=5$	1200°C, 24h, Ar	1250°C, 24h, $CO_2/CO=5$	$CO_2/CO=3$
C	1200°C, 12h, $CO_2/CO=5$	1200°C, 24h, Ar	1250°C, 24h, $CO_2/CO=5$	$CO_2/CO=5$

Table 3.1: Synthesis process for $LuFe_2O_{4-\delta}$.

Single crystal growth is very challenging. It is preferable if the seed rod is itself a single crystal. In order to form a large single crystal it is important that the material moving out of the molten zone picks up a strong orientation in which to crystallize; if the seed is well oriented the growing crystal will follow this orientation. In the first floating zone growth a polycrystalline seed rod was used. The density of the feed rod presented an issue during the first growth and only a small boule, ~15mm, of single crystal was grown. The crystal obtained from this growth was used as the seed rod for subsequent growths.

In order to resolve the issue of rod density and ensure the stability of the molten zone two changes were made to the crystal growth procedure. The polycrystalline feed rods were sintered for twice as long and a fast zone was then run through the rod using the

floating-zone furnace at a rate of ~10-15mm/h prior to the single crystal growth. This is too fast to form single crystals, the purpose of the run was to strengthen the feed rod for the slow single crystal growth. The atmosphere used for the quick run was the same as the atmosphere used for the successive single crystal growth.

Using this adjusted growth procedure, two $LuFe_2O_{4-\delta}$ single crystals have been successfully grown, the first in an atmosphere of $CO_2/CO=3$ and the second in an atmosphere of $CO_2/CO=5$.

Fig.3.1: Single crystal boules (a) $CO_2/CO=3$, (b) $CO_2/CO=5$. Red arrows mark the facets formed during cooling.

The single crystal boule grown in the $CO_2/CO=3$ atmosphere was ~55mm in length and 5mm in diameter. A single crystal boule of ~50mm in length and 5mm in diameter was grown in an atmosphere of $CO_2/CO=5$. Pictures of the boules are shown in Fig.3.1. Both boules formed flat facets during cooling. The facets formed in the crystal grown using the $CO_2/CO=3$ atmosphere were irregular and small. In contrast, the crystal grown in the $CO_2/CO=5$ atmosphere formed two large parallel facets along opposite sides of the boule, forcing the crystal to take on an oblong cross section for ~30mm of the growth.

The quality of the single crystals and the orientation of their crystallographic axes were determined using Laue x-ray diffraction. The patterns obtained from the crystals, shown in Fig.3.2, were compared with those simulated by OrientExpress software from the crystal space group and lattice parameters of $LuFe_2O_4$. From the Laue patterns and the consistency of the plate like facets formed on the outside of the crystal it was apparent that the quality of the $CO_2/CO=5$ single crystal was far superior to that of the $CO_2/CO=3$ crystal. The $CO_2/CO=5$ boule was one single crystal grain for most of its length whereas the $CO_2/CO=3$ boule was found to be made up of many smaller single crystal volumes. Both crystals had the growth axis along the crystallographic *b*-axis. The high quality of

the $CO_2/CO=5$ crystal may well be attributed to the seed crystal used. The crystal formed in the $CO_2/CO=5$ growth readily picked up a strong orientation along the *b*-axis allowing for a large single crystal to be grown. Both crystals were orientated with respect to the three principle axes. Using a low speed diamond saw, flat platelets measuring typically 4mm x 3mm x 0.5mm were cut from the single crystals in preparation for magnetic and electric property measurements. Due to the shape and size of the $CO_2/CO=3$ single crystals only plates along the *c*-axis could be correctly identified and cut.

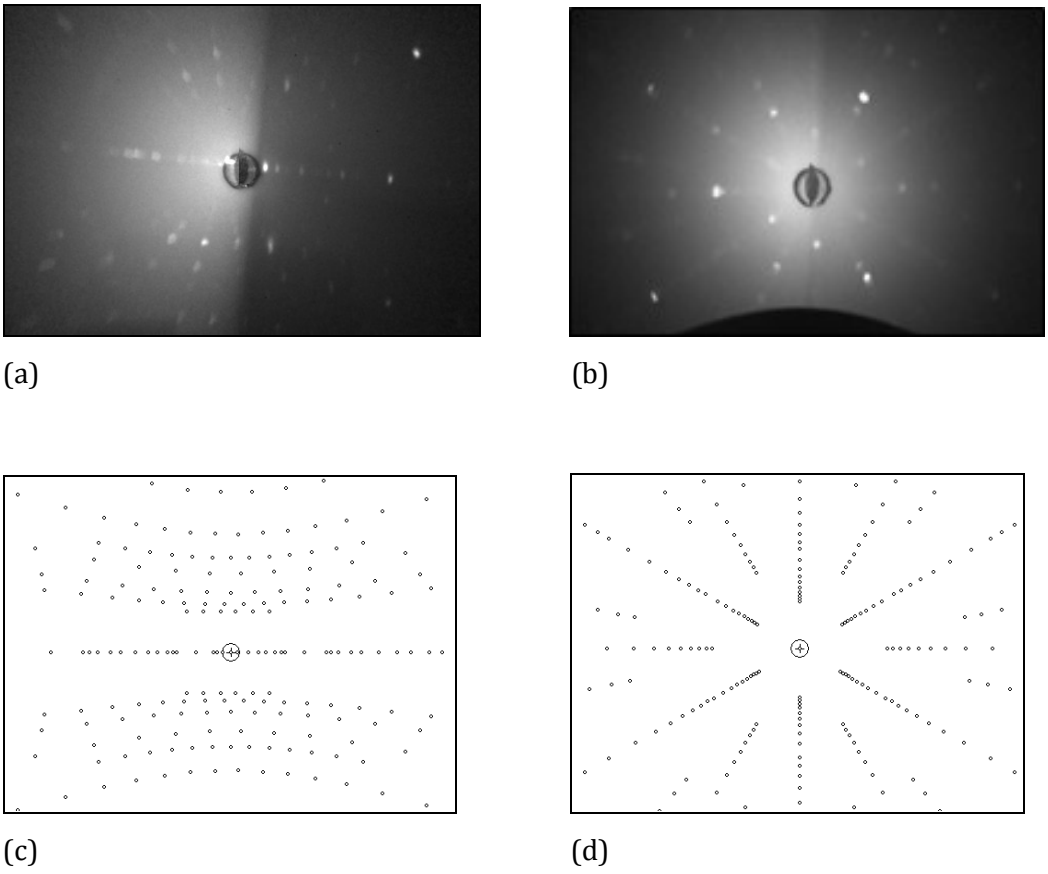

Fig.3.2: Laue patterns obtained from the $CO_2/CO=5$ single crystal along the (a) *b* and (b) *c*-axes. $LuFe_2O_4$ Laue patterns generated using OrientExpress software for (c) *b* and (d) *c*-axes.

3.2 Powder X-ray Diffraction

In order to check the phase formation and impurity levels of the synthesised $LuFe_2O_{4-\delta}$ samples, powder x-ray diffraction patterns were taken at various stages throughout the crystal growth process. Preliminary measurements were taken during the sintering stage using a Philips PW1720 x-ray generator, with 0.05° increments and a counting time of 2s/step. More detailed diffraction data was collected at the end of the crystal growth process using a Panalytical X'Pert Pro multipurpose x-ray diffraction system.

The preliminary x-ray diffraction patterns taken at the end of the sintering stage, prior to crystal growth, are shown in Fig. 3.3. At this stage all three powders were prepared in the same way and heated in the same gas environments, the only difference being the period of the final sintering, as described in Section 3.1.

The diffraction patterns were initially matched with the $LuFe_2O_4$ data published by Iida et al. for their oxygen deficient $LuFe_2O_4$ single crystal. A comparison was also made with the Lu_2O_3 and Fe_2O_3 patterns, the starting compounds, to check for incomplete synthesis. The diffraction patterns were then compared with data available in the database for oxygen deficient compounds such as $LuFe_2O_{3.95}$ and with compounds with different stoichiometric ratios of Lu, Fe and O such as $LuFeO_3$ and $Lu_2Fe_3O_7$. The diffraction patterns were also checked for impurity compounds such as Fe_3O_4. Only the high intensity peaks of possible impurity compounds are expected to be present in the diffraction patterns as the percentage of impurity is expected to be low.

A number of impurity peaks have been identified in the diffraction pattern of powder batch A. The pattern matched well with the expected pattern of $LuFe_2O_4$, however, many of these peaks are split into doublets especially the high intensity reflections. The Lu_2O_3, Fe_2O_3 and Fe_3O_4 high intensity peaks do not appear to closely match any of the impurity peaks. Many of the low angle reflections can be associated with the diffraction peaks published for $LuFeO_3$ and $Lu_2Fe_3O_7$ compounds. $LuFeO_3$ and $Lu_2Fe_3O_7$ impurities also account for a number of the secondary/split peaks. The intensity of these impurity peaks are relatively high, ~30%, compared to the maximum peak associated with a $LuFe_2O_4$ reflection.

The x-ray diffraction pattern obtained from the powder batch B fits very closely with the $LuFe_2O_4$ data. The number of peaks present in this pattern is much less than the number recorded for the batch A; the peaks are not split into doublets as before and there are

very few impurity peaks. The intensity of any impurity peaks present in the scan is very low, 8%. Some very small low angle peaks indicate the presence of a $Lu_2Fe_3O_7$ impurity. A very narrow peak present at 23.7° may be associated with a $LuFeO_3$ impurity, however, this peak may simply be noise as it is of very low intensity and no other peaks matching the $LuFeO_3$ pattern can be clearly identified.

Batch C has a similar x-ray diffraction pattern as batch B. The scan in general is much noisier than batches A and B. Background noise often results in samples with a large grain size, obtained as a result of sintering at high temperatures. Unlike batches A and B, no low angle $LuFeO_3$ or $Lu_2Fe_3O_7$ impurity peaks are observed. The sample was definitely of a higher purity at this stage of the synthesis.

It is not possible to accurately determine the oxygen content of the $LuFe_2O_{4-\delta}$ powders using powder x-ray diffraction. The $LuFe_2O_4$ and $LuFe_2O_{3.95}$ diffraction patterns are almost identical, the only credible difference being a small shift in the position of the reflections. The diffraction data published by Iida et al. [13] has been taken from a non-stoichiometric $LuFe_2O_4$ single crystal, however, the exact oxygen deficiency has not been disclosed.

Using the Philips PW1720 x-ray generator a second powder x-ray diffraction scan was taken from the batch A. A section of the feed rod that had passed through the molten zone was cut and finely ground into a powder. The resulting diffraction pattern, shown in Fig.3.4, has fewer impurity peaks than the pattern obtained from the same powder at the end of the sintering stage. The $Lu_2Fe_3O_7$ impurity peaks are no longer observed.

The high resolution x-ray diffraction patterns of the powdered $CO_2/CO=3$ and $CO_2/CO=5$ single crystals, recorded using the Panalytical X'Pert Pro multipurpose x-ray diffraction system, are shown in Fig.3.5. Both single crystals have very similar x-ray patterns to the published $LuFe_2O_4$ data from the database. No $LuFe_2O_4$, $Lu_2Fe_3O_7$ or any other impurity peaks are present in the scan. The peaks are not split like the polycrystalline data and very little background noise has been recorded making the patterns much clearer and the peaks better defined. Both of the single crystal patterns show high intensity peaks at *c*-axis reflections indicating that a high proportion of the crystallite planes are oriented along the *c*-axis. A Rietveld refinement of the x-ray powder diffraction data was conducted for each crystal. The hexagonal lattice parameters estimated from the data are shown in Table 3.2.

	$CO_2/CO=3$ Single Crystal	$CO_2/CO=5$ Single Crystal
a(Å)	3.44520(5)	3.44255(7)
b(Å)	3.44520(5)	3.44255(7)
c(Å)	25.29401(39)	25.28104(52)

Table 3.2: Lattice parameters for $CO_2/C0=3$ and $CO_2/CO=5$ $LuFe_20_{4-\delta}$ from refined powder x-ray diffraction data.

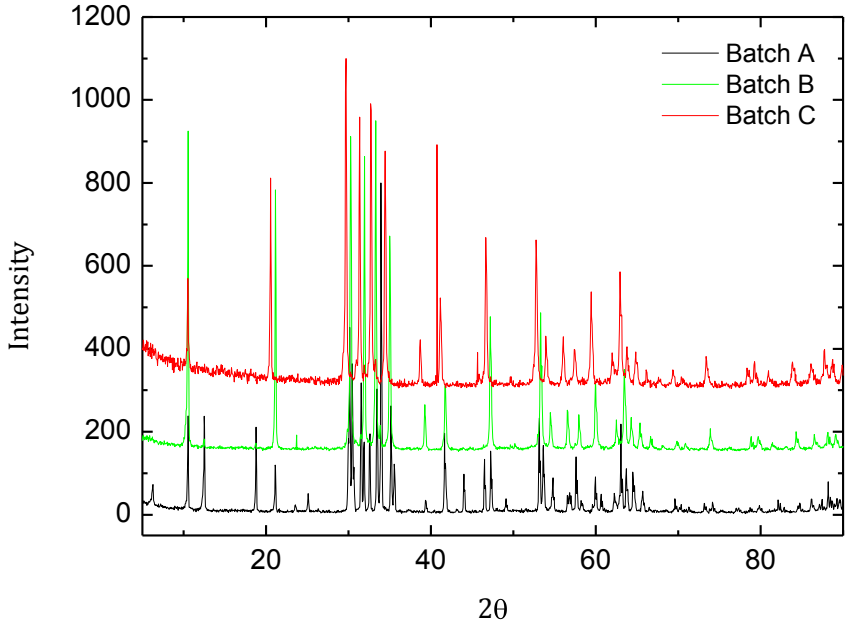

Fig. 3.3: Powder x-ray diffraction patterns for polycrystalline $LuFe_2O_{4-\delta}$.

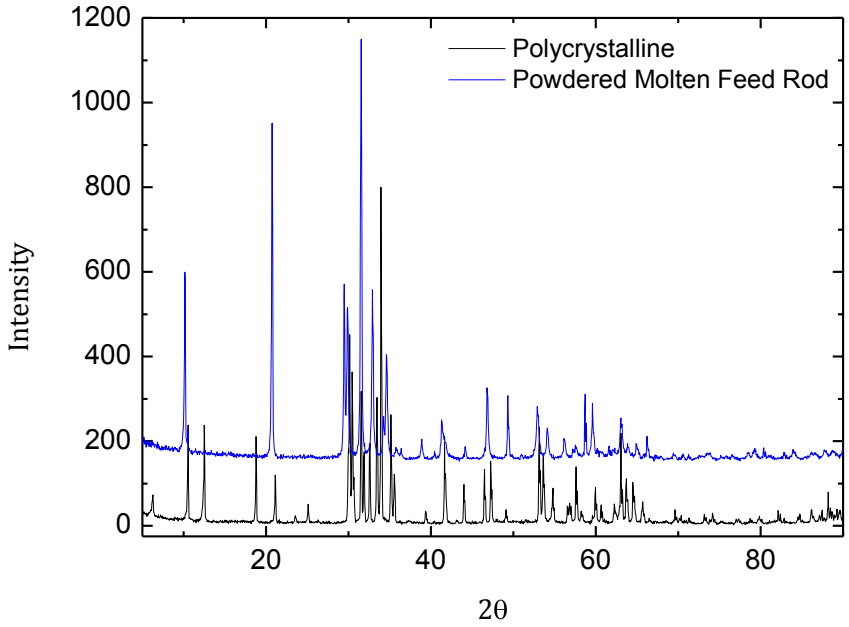

Fig. 3.4: Powder x-ray diffraction patterns for $LuFe_2O_{4-\delta}$ Batch A: Polycrystalline and Powdered Molten Feed Rod.

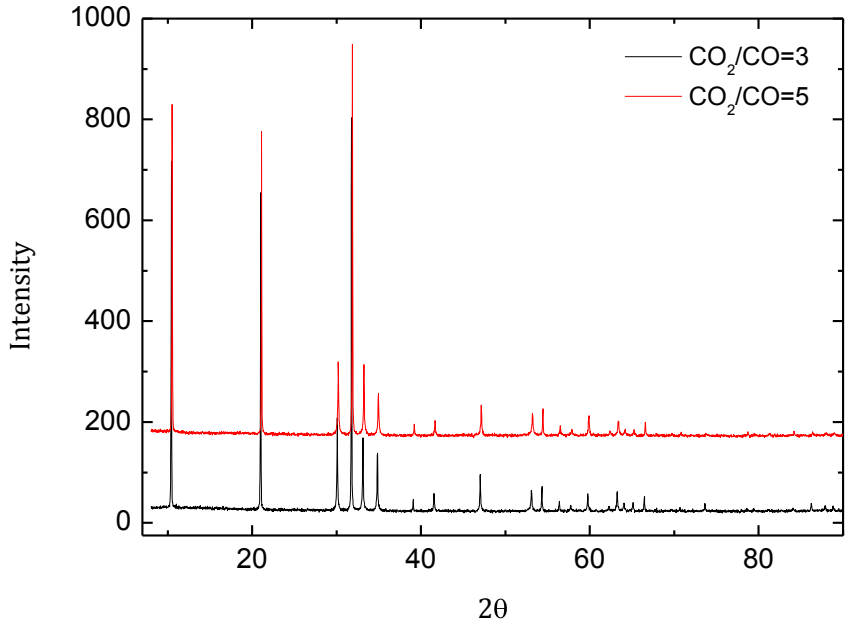

Fig. 3.5: Powder x-ray diffraction patterns for single crystal $LuFe_2O_{4-\delta}$ grown in $CO_2/CO=3$ and $CO_2/CO=5$ gas environment.

3.3 Magnetic Properties

The SQUID, described in Section 2.5, was used to measure the magnetic response of the samples at different temperatures and in different fields. The magnetisation as a function of temperature was measured during heating from 2K to 300K at a sweep rate of 3K/min in magnetic fields ranging from 1 to 50kOe. Zero field-cooled (ZFC) and field-cooled (FC) data was collected for both the polycrystalline and oriented single crystal samples. The magnetisation was plotted in units of emu/g, allowing a comparison to be made with the data reported by Kim et al. [28].

(i) Polycrystalline Samples

The temperature dependence of the ZFC and FC magnetisation for polycrystalline $LuFe_2O_{4-\delta}$ is shown in Fig.3.6. In a relatively low external field of 1kOe, the magnetisation increases markedly below 260K. The ZFC magnetisation reaches a peak value of ~1.3emu/g at 241K. Below this temperature the ZFC and FC magnetisations separate. A plateau is observed in the ZFC data between 190 and 225K. The FC data undergoes a notable change in gradient at a similar temperature. At low temperatures, the ZFC magnetisation decreases to close to zero whereas the FC magnetisation continues to increase reaching a maximum value of ~4.8emu/g below 50K. The features in the ZFC magnetisation are stretched out over a larger temperature range when fields greater than 1kOe are applied across the polycrystalline sample. The features become less defined and merge together in high magnetic fields, for example the peak and the plateau in the ZFC data can no longer be defined resulting in a single broad feature. The maximum values of the magnetisations reached also increases with increasing magnetic field. For example, in a 50kOe field the ZFC magnetisation reaches a maximum value of ~18.5emu/g at 116K and the FC magnetisation reaches a low temperature maximum of ~24 emu/g.

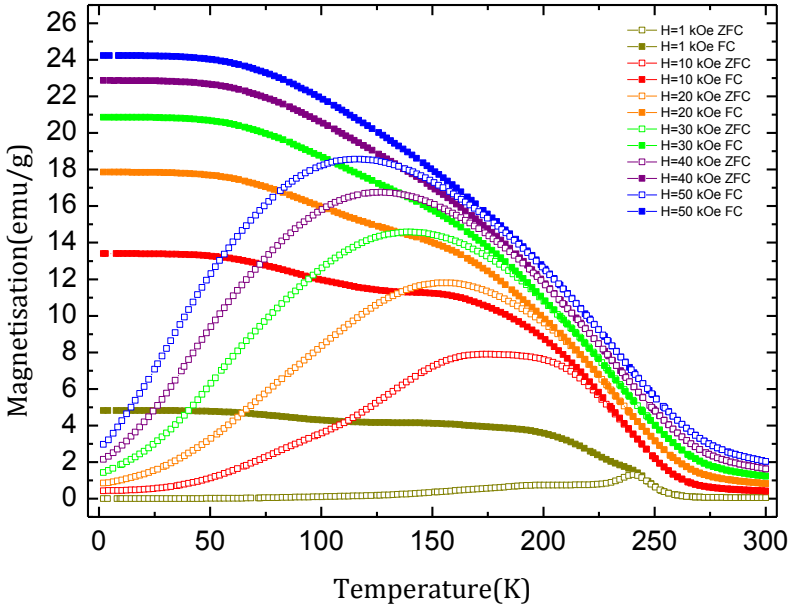

Fig. 3.6: ZFC and FC magnetisation of polycrystalline $LuFe_2O_{4-\delta}$ as a function of temperature, measured in applied magnetic fields ranging between 1kOe and 50kOe.

(ii) $CO_2/CO=3$ Single Crystal

The magnetisation results for the oriented single crystal grown in the $CO_2/CO=3$ atmosphere are shown in Fig.3.7. Measurements were taken for magnetic fields applied both parallel and perpendicular to the *c*-axis.

When a 1kOe field is applied parallel to the *c* axis, both the ZFC and FC magnetisations show a sudden increase below 240K followed by a peak in the ZFC magnetisation of ~1.1emu/g at 197K. The ZFC and FC magnetisations separate below this temperature. At low temperatures, a maximum value of ~2.7emu/g is reached by the FC magnetisation. The ZFC magnetisation decreases to a value close to zero at low temperatures. With the exception of the peak in the ZFC magnetisation both data plots are relativity smooth and do not show any other distinct features.

When stronger fields, >1kOe, were applied parallel to the *c*-axis, the temperature of the ZFC maximum was found to decrease. The ZFC peak moves from 172K in 10kOe to 109K in 50kOe. The maximum values reached by both the ZFC and FC magnetisations increases with increasing magnetic field strength, for example a 50kOe field increases the maximum in the ZFC and FC magnetisations to ~18.7emu/g and ~24emu/g, respectively. The overall size of the ZFC feature becomes enlarged and less defined in

high fields.

The magnetisation reached by both the ZFC and FC runs when magnetic fields are applied perpendicular to the *c*-axis are much smaller than those reached when fields are applied parallel to the *c*-axis. A peak of ~0.06emu/g is observed at 204K when a 1kOe filed is applied across the sample. The maximum reached by the FC magnetisation is less than ~0.1emu/g. The high and low temperature ZFC magnetisations are the same as those achieved at the temperature extremes when the field is applied parallel to the *c*-axis. The maximum values reached by both the ZFC and FC magnetisations increase with increasing magnetic field. The temperature of the ZFC peak continues to decrease with increasing field strength, however, the change in temperature is much less than when the field is applied parallel to the *c*-axis. For example, in a 10kOe field a ZFC maximum of ~0.55emu/g occurs at 196K which then reaches a value of ~2.6emu/g at 178K in a 50kOe field.

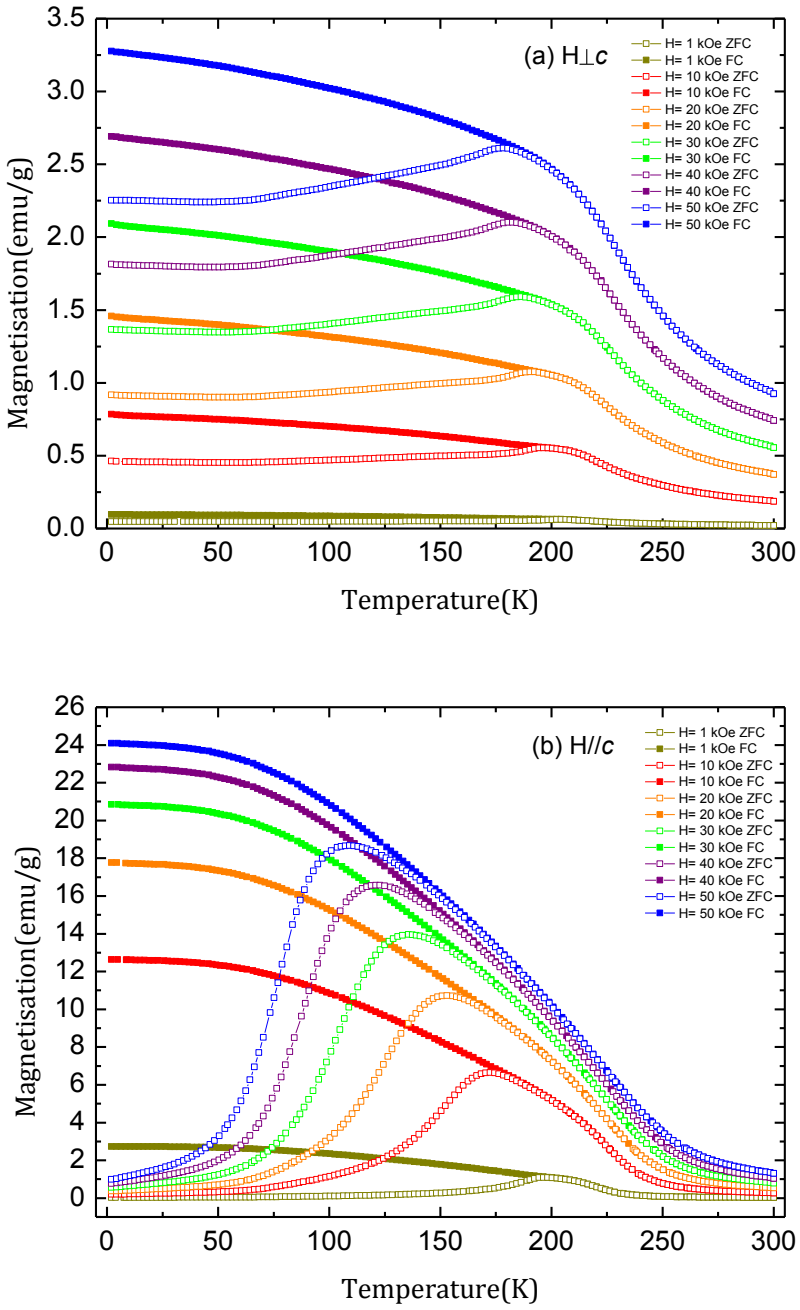

Fig. 3.7: Temperature dependence of the ZFC and FC magnetisation for single crystal $LuFe_2O_{4-\delta}$ grown in a $CO_2/CO=3$ gas environment. Measurements taken in magnetic fields applied (a) perpendicular and (b) parallel to the *c*-axis.

(iii) $CO_2/CO=5$ Single Crystal

The temperature dependence of the ZFC and FC magnetisation data collected from the $LuFe_2O_{4-\delta}$ single crystal grown in the $CO_2/CO=5$ atmosphere are shown in Fig.3.8. Magnetic fields were applied along each of the *a*, *b* and *c* crystallographic axes.

Both the ZFC and FC data show a sharp increase in the magnetisation below 250K for a 1kOe magnetic field applied parallel to the *c*-axis. The ZFC magnetisation reaches a maximum of ~4emu/g at 220K. The magnetisation decreases steadily below this temperature approaching zero at low temperatures, <50K. The ZFC magnetisation shows a step-like feature between 150K and 200K. The FC magnetisation exhibits a number of low temperature features, spread over a large temperature range. A maximum value of ~6emu/g is reached in the FC magnetisation below 50K. When fields greater than 1kOe are applied parallel to the *c*-axis the features in both the ZFC and FC magnetisations become enlarged and diffuse. A maximum value of ~25emu/g is reached by the ZFC magnetisation at 89K in a field of 50kOe. In this example, the FC magnetisation reaches a low temperature value of ~29emu/g.

When a 1kOe field is applied parallel to the *a*-axis, the ZFC and FC magnetisations show a sudden rise below 250K. A peak of ~0.095emu/g occurs in the ZFC magnetisation at 234K. The FC magnetisation does not reach as high a value at this temperature; instead a regional maximum of ~0.09emu/g is observed. At lower temperatures the FC magnetisation shows a broad feature between 150K and 225K; below 50K a maximum value of ~0.095emu/g is reached. The ZFC magnetisation also exhibits a feature within the 150-225K temperature range. The ZFC magnetisation continues to decrease below this temperature region reaching a low temperature value of ~0.04emu/g. As the strength of the applied magnetic field is increased, the value of both the ZFC and FC magnetisations is increased. The features observed in both the ZFC and FC data become broader and the temperature of the peak in the ZFC curve decreases with increasing field. For example, a peak of ~0.6emu/g occurs at 221K in a 10kOe field and a larger peak of ~2.83emu/g is observed at 178K in a 50kOe field. In fields greater than 1kOe, the ZFC and FC magnetisation curves separate close to the maximum of the ZFC curve, the FC curves then rise to higher magnetisations and a regional maximum is reached within the 150-200K temperature range. This regional maximum becomes the global maximum in fields greater than 20kOe.

The ZFC and FC magnetisations reached when a 1kOe field is applied along the *b*-axis are larger than those achieved when the same field is applied parallel to the *a*-axis. Both the ZFC and FC magnetisations show a notable rise below 250K where the ZFC curve reaches a maximum at 229K. At this same temperature the ZFC and FC curves separate, the FC magnetisation does not reach as high a value as the ZFC curve, ~0.26emu/g and ~0.29emu/g respectively. The FC magnetisation continues to rise reaching a low temperature maximum of 0.34emu/g. The ZFC magnetisation decreases from the

maximum to a value of ~0.06emu/g below 50K. The secondary features observed when fields are applied along the *a*-axis are not as definitive in this case. Slight changes in the gradient of the curves do exist within the same temperature range, however, they are not as well defined. These features become more apparent as the field strength is increased. The ZFC and FC magnetisations separate above the peak in the ZFC curve, below this temperature the ZFC exhibits a step-like feature between 150K and 200K followed by a decrease in magnetisation value below this temperature range. The FC magnetisation reaches a regional maximum within this same temperature range. This feature becomes more defined as the field is increased, reaching magnetisations close to the global maximum in high fields. The overall magnitudes of the ZFC and FC magnetisations increase while the temperature of the ZFC maximum decreases with increasing field strength. For example, the temperature of the ZFC maximum occurs at 218K in a 10kOe field and at 187K in a 40kOe field.

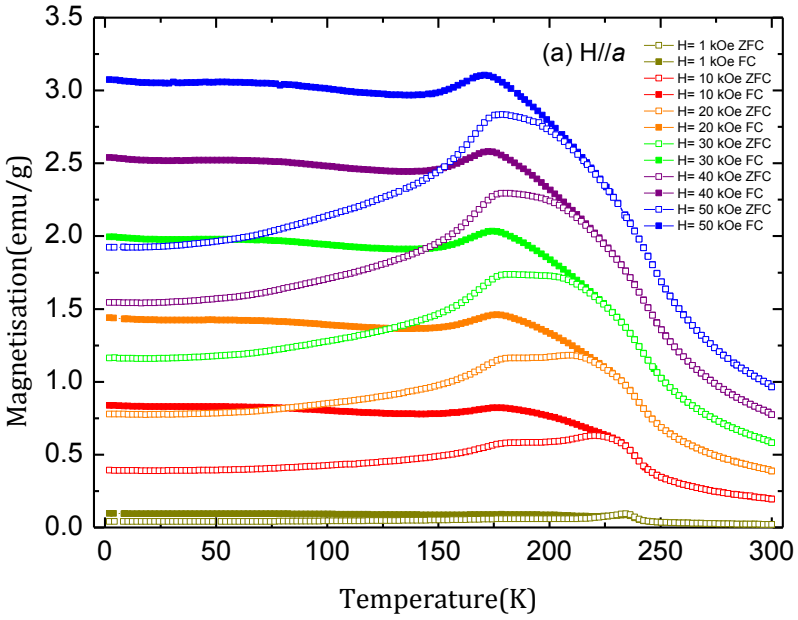

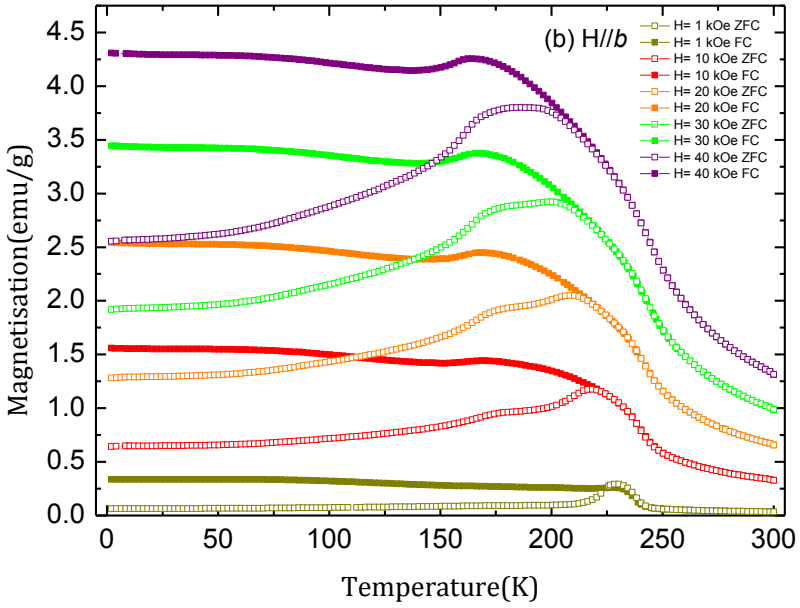

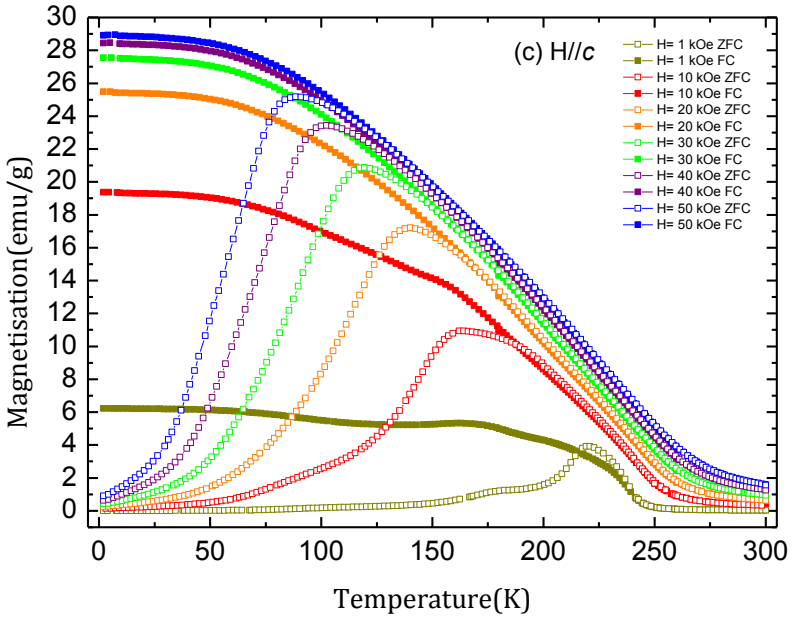

Fig. 3.8: Magnetisation as a function of temperature for single crystal $LuFe_2O_{4-\delta}$ grown in a CO_2/CO=5 gas environment. ZFC and FC measurements taken in magnetic fields applied along the (a) *a*, (b) *b* and (c) *c*-axis.

3.4 Dielectric Properties

The dielectric response of the polycrystalline and single crystal $LuFe_2O_{4-\delta}$ samples was investigated. Dielectric constant versus temperature data was collected for each sample as detailed in Section 2.6.2(i). Thin plates were cut from the single crystal samples such that electric fields could be applied along the crystallographic axes. The plates were

prepared for measurement as described in Section 2.6.2. Magnetic fields ranging up to 90kOe were applied along each of crystal axes.

Each sample was cooled in a magnetic field from 325K to 150K at a rate of 3K/min. The capacitance as a function of temperature was then measured during heating to 325K at a sweeping rate of 2K/min. The dielectric constant of each sample was calculated for 10, 20 and 30kHz measurements.

(i) Polycrystalline Sample

A strong frequency dependence was observed in the dielectric response of the polycrystalline sample. Fig.3.9 shows a large dispersion in the dielectric constant between low frequency measurements where the 10kHz measurements exhibits the highest dielectric constant. A number of features were observed in the zero magnetic field dielectric response. From the 20kHz data, the dielectric constant starts to rise to values of the order 10^3-10^4 above 190K. This steady rise is followed by a sudden increase in dielectric constant at 260K which reaches a peak of ~$9x10^4$ at 274K. The dielectric constant then decreases to a local minimum at 280K. Above this temperature, the dielectric constant increases sharply reaching very high values.

Magnetic fields of 1, 10, 30 and 90kOe were applied across the sample. The dielectric constant of the sample, shown in Fig.3.10, was found to increase when magnetic field were applied. A large dispersion in the magnetic response of the dielectric constant was observed between 260K and 300K. Both the temperature at which the peak was observed and the height of the peak increased with increasing field strength, for example, in a 90kOe field a peak of ~$1.2x10^5$ was recorded at 278K.

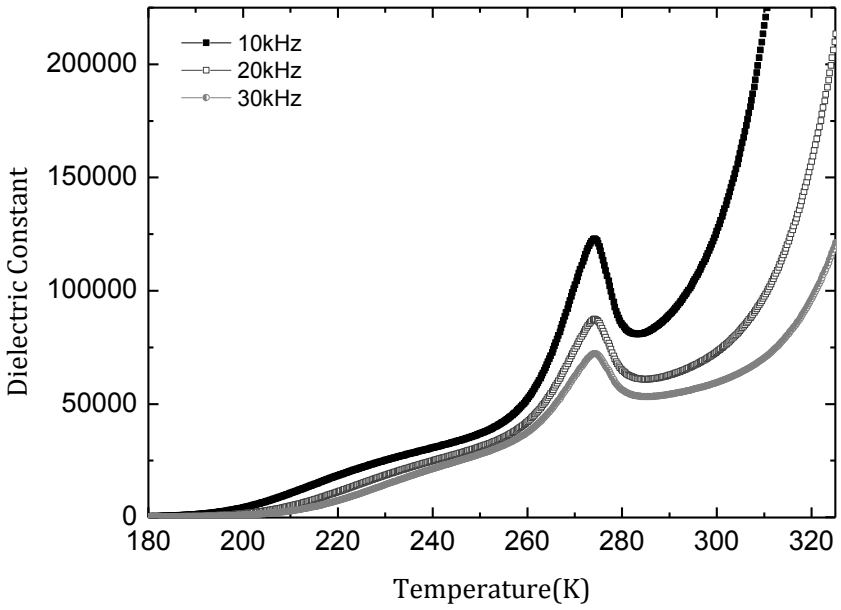

Fig. 3.9: Dielectric constant versus temperature for polycrystalline $LuFe_2O_{4-\delta}$ in zero magnetic field. Measurements made at 10, 20 and 30KHz show strong frequency dependence.

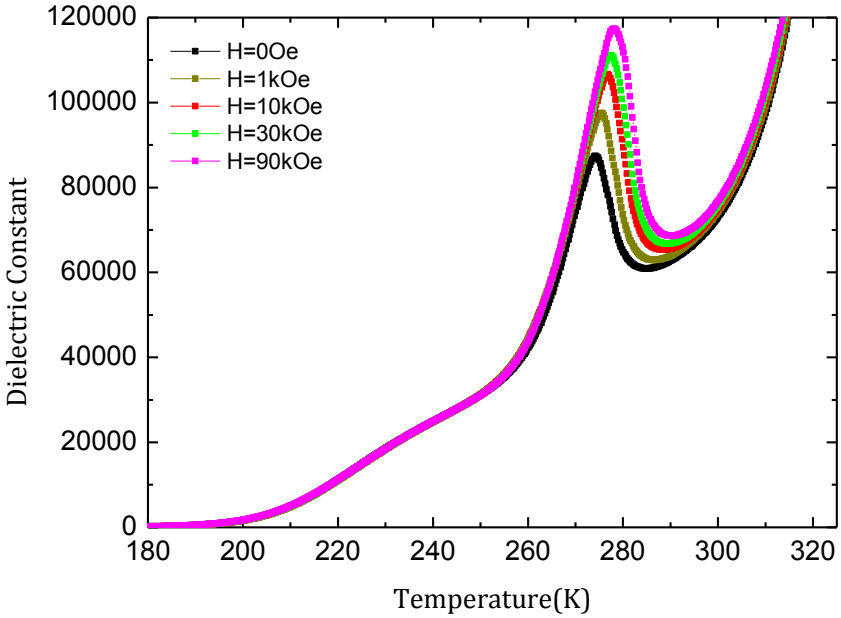

Fig. 3.10: Temperature dependence of the dielectric constant for polycrystalline $LuFe_2O_{4-\delta}$. Measurement made at 20kHz in applied magnetic fields of up to 90kOe.

(ii) $CO_2/CO=3$ Single Crystal

Only one orientated thin plate could be cut from the $CO_2/CO=3$ single crystal. The plate

was cut along the *a*-*b* plane, allowing for the electric field to be applied parallel to the *c*-axis. Magnetic fields were applied both parallel and perpendicular to the *c*-axis. The dielectric response of the crystal is shown in Fig.3.11.

A large dispersion in the dielectric constant is observed for the low frequency measurements. The 20kHz measurements shows a steady rise in the dielectric constant above 220K followed by a sudden increase around 274K. At room temperature, the dielectric constant shoots off to very high values. Within this high temperature region, the resistance of the sample is very low; consequently, the sample becomes conducting and can no longer be considered as a dielectric. At low temperatures, the dielectric constant is of the order of 10^1-10^2; this value increases close to $5x10^4$ at 274K. The very large values are believed to be an effect of the low resistance of the sample. Magnetic fields of 1, 10 and 30kOe were applied parallel to the *c*-axis. As the field strength is increased, the dielectric constant of the sample decreases. Below 274K, the dielectric responses are very close in value, at 274K the zero field response diverges from the in-field measurements. The magnetic field raises the temperature of the feature, for example the dielectric response of the 1kOe field shows a sudden rise at 275K whereas the 30kOe response does not increase in value until 277K. A similar dielectric response was observed when 10 and 30kOe fields were applied perpendicular to the *c*-axis.

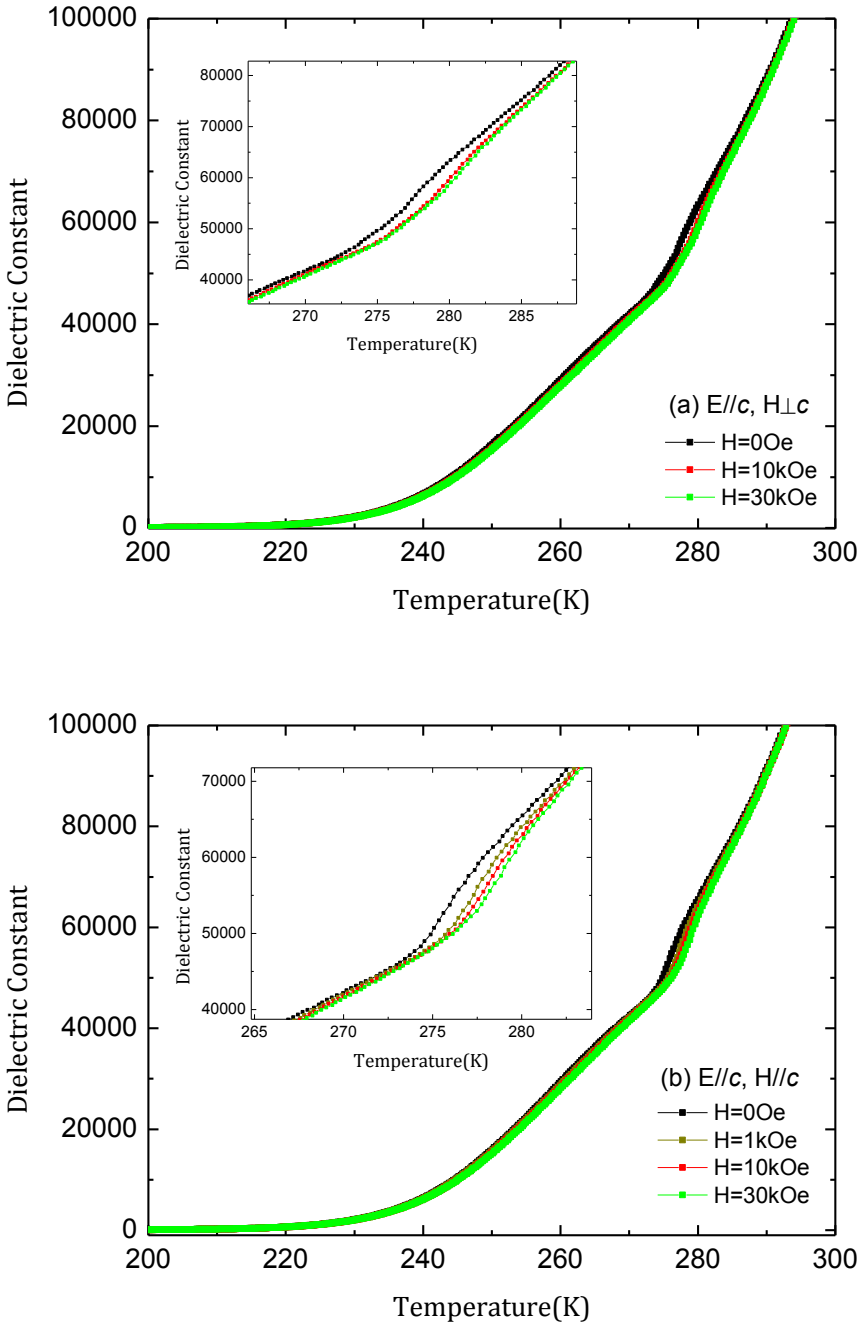

Fig. 3.11: Dielectric Constant as a function of temperature for single crystal $LuFe_2O_{4-\delta}$ grown in a $CO_2/CO=3$ gas environment. Measurement made at 20kHz along the *c*-axis in magnetic fields applied (a) perpendicular and (b) parallel to the *c*-axis. Insets show a magnified view of the feature between 270 and 280K.

(iii) $CO_2/CO=5$ Single Crystal

The dielectric response along each of the *a*, *b* and *c* crystallographic axes was examined. Three thin plates were cut from the $CO_2/CO=5$ single crystal. Each plate was oriented such that a magnetic field could be applied parallel to each principal axes. The dielectric

response of the crystal along the *a*, *b* and *c*-axes are shown in Fig. 3.12, 3.13 and 3.14, respectively.

The zero magnetic field response along the *a*-axis is very similar to that of the polycrystalline sample. The dielectric constant increases to values in the order of 10^3-10^4 above 180K. Between 180K and 240K a shallow step-like feature is observed. A notable change in gradient of the dielectric response at 245K leads to a peak in the data at 270K. The dielectric constant then decreases from ~6.5×10^4 to ~5.5×10^4 at 280K. Above room temperature, the dielectric constant continues to rise reaching very high values. A range of magnetic fields were applied along the *a*, *b* and *c*-axes. Below 240K, the dielectric response for fields applied along the *a* and *b*-axes show a decrease in dielectric constant with increasing field strength. Between 240K and 250K, the order of the responses change such that a higher dielectric constant is reached by a stronger field. Above 270K there is a large dispersion between the responses, the temperature and value of the peak both increase with increasing field strength. Magnetic fields applied along the *c*-axes were found, in general, to increase the value of the dielectric constant. Fields applied along either of the *a*, *b* and *c*-axes induce a similar change in temperature and dielectric constant of the high temperature features.

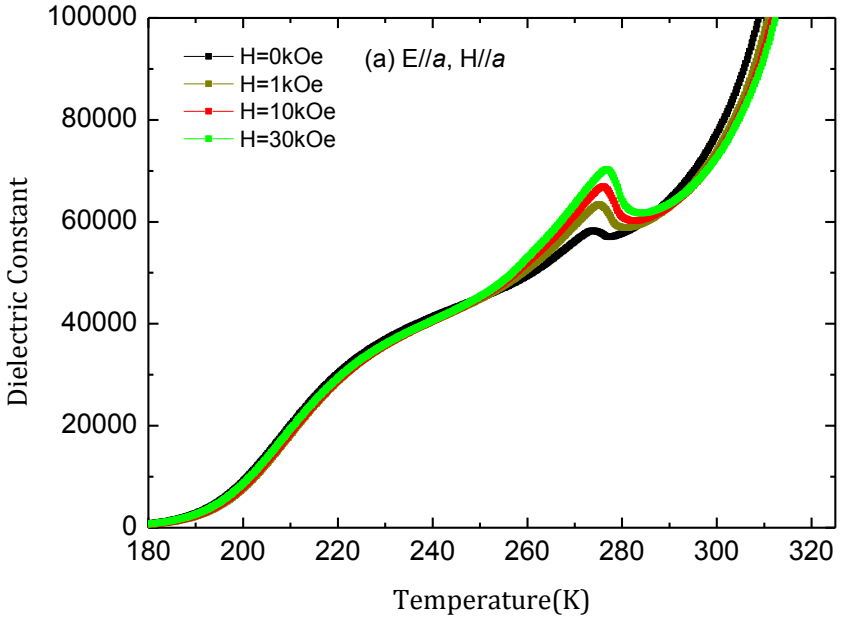

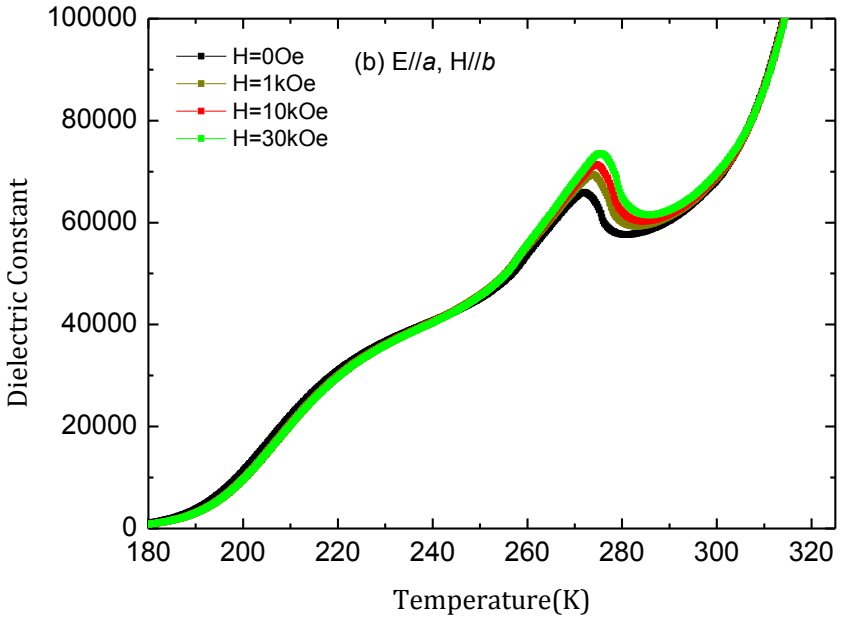

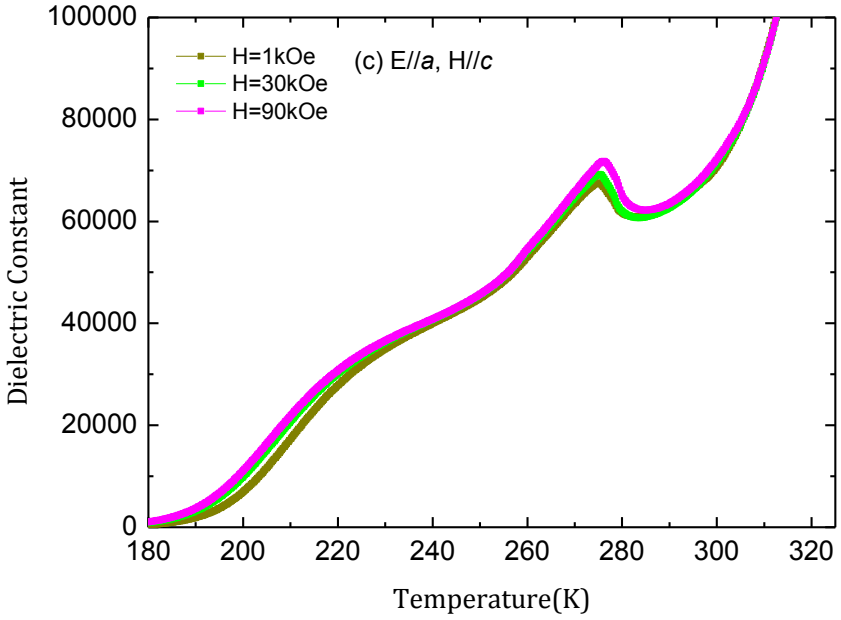

Fig. 3.12: Dielectric response measured along the *a*-axis as a function of temperature for single crystal $LuFe_2O_{4-\delta}$ grown in a CO_2/CO=5 gas environment. Measurement made at 20kHz in magnetic fields applied along the (a) *a*, (b) *b* and (c) *c*-axis.

Along the *b*-axis, the single crystal exhibits a low temperature dielectric response similar to that of the *a*-axis in zero magnetic field. The first notable increase in the dielectric constant occurs at 190K. Above this temperature a shallow step-like feature is observed. This feature is followed by a steeper rise in the dielectric constant at 250K. A local maximum of $\sim 4 \times 10^5$ is recorded at 270K. The response then shows an abrupt rise in the dielectric constant at 276K. Above this temperature the dielectric constant shoots off to

very high values. The sample recorded a very low resistance at room temperature. Magnetic fields of 10kOe and 90kOe were applied parallel to the *a*-axis. The dielectric responses in field are very similar to the zero field measurement at low temperatures. Above 250K, the gradient of the dielectric constant becomes dependent on the strength of the applied field; a higher dielectric constant is reached in a higher magnetic field. The temperature of the local maximum also increases with increasing field strength; the 90kOe response reaches ~$5x10^5$ at 279K. An almost identical response was observed when magnetic fields were applied parallel to the *c*-axis. The dispersion of the responses above 250K appears to be greater when magnetic fields are applied parallel to the *c*-axis. The increase in the local maximum from the zero field value when a 10kOe field was applied parallel to the *c*-axis was found to produce a response almost twice as large as when the field was applied along the *a*-axis. The dielectric response of the sample when magnetic fields were applied parallel the *b*-axis was also investigated. The dielectric constant is much lower in this case. Both the zero field and in-field measurements show shallow step-like features between 190 and 250K followed by a dispersion of the responses above 250K. The dielectric constant does not shoot off abruptly beyond the local maximum at 260K, instead it continues to rise with a much lower gradient. Both the value and temperature of this feature increase with increasing field strength. A second smaller feature at a slightly higher temperature is also observed when fields are applied parallel to the *b*-axis.

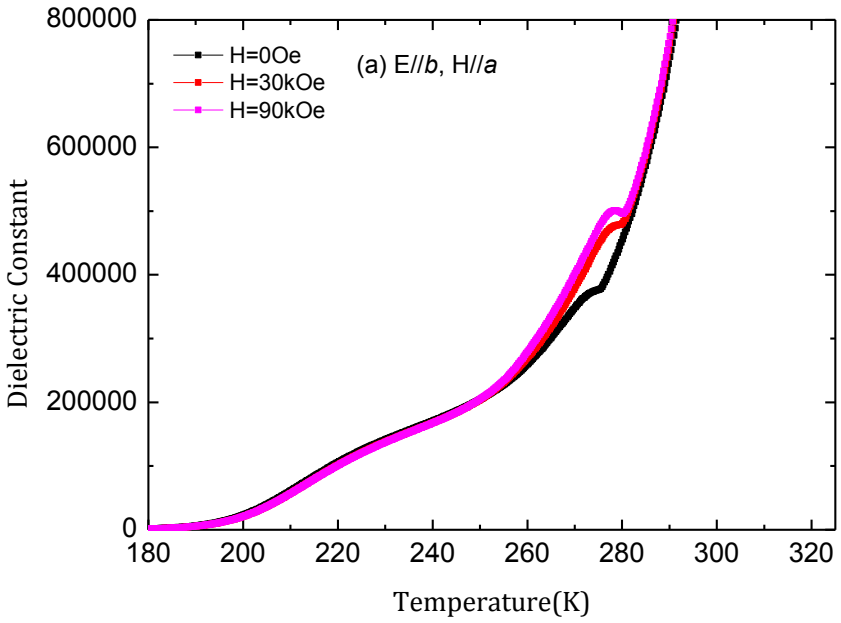

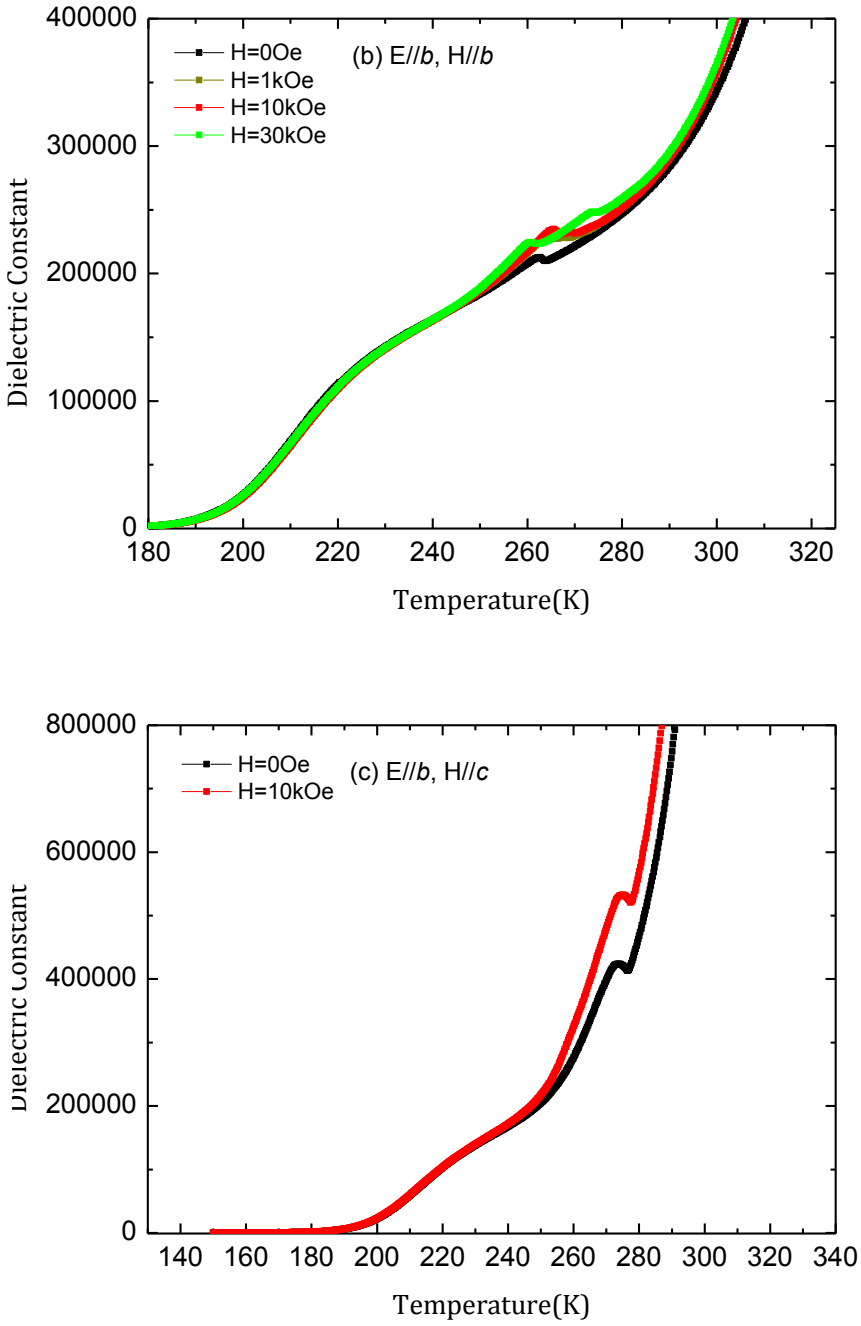

Fig. 3.13: Dielectric constant measured along the *b*-axis of the $LuFe_2O_{4-\delta}$ single crystal grown in a CO_2/CO=5 gas environment. Measurement made at 20kHz in magnetic fields applied along the (a) *a*, (b) *b* and (c) *c*-axis.

The dielectric response of the single crystal along the *c*-axis shows an increase in the dielectric constant above 240K in zero magnetic field. The dielectric constant continues to rise reaching a value of ~$4.5x10^4$ at 275K. Above this temperature, a small step-like feature is observed followed by an increase in the gradient of the curve. The temperature at which this feature occurs is dependant on the strength of the magnetic field. In general, both the temperature and value of the feature increases as the field

increases. For example, when a 1kOe field is applied parallel to the *c*-axis, the feature rises to ~5x10^4 at 277K. The dielectric responses are typically very close in value. It is only within the temperature range 270-285K that the curves diverge and the effect of magnetic field strength on the dielectric response can be seen. The clearest response is observed when magnetic fields are applied parallel to the *c*-axis.

All of the dielectric responses along each of the crystallographic axes exhibited a strong frequency dependence.

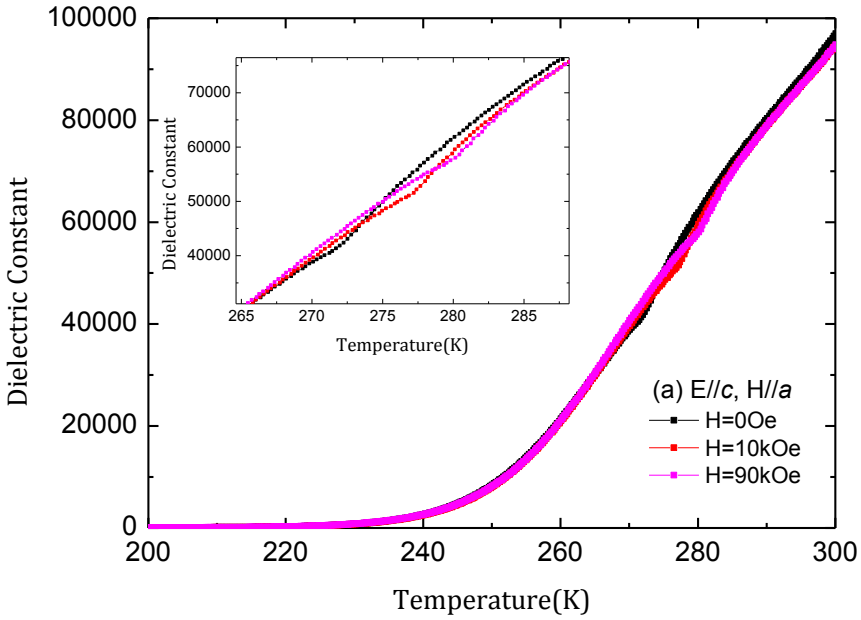

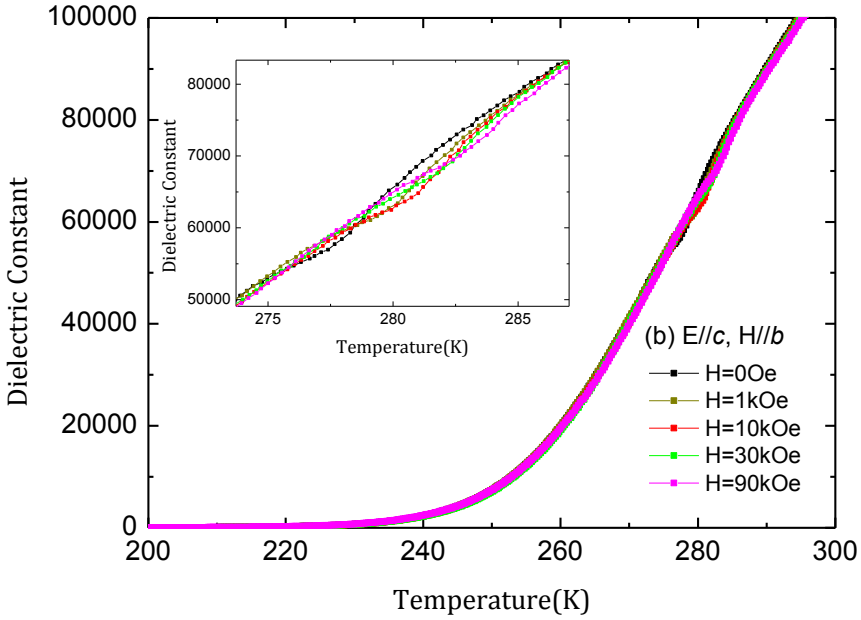

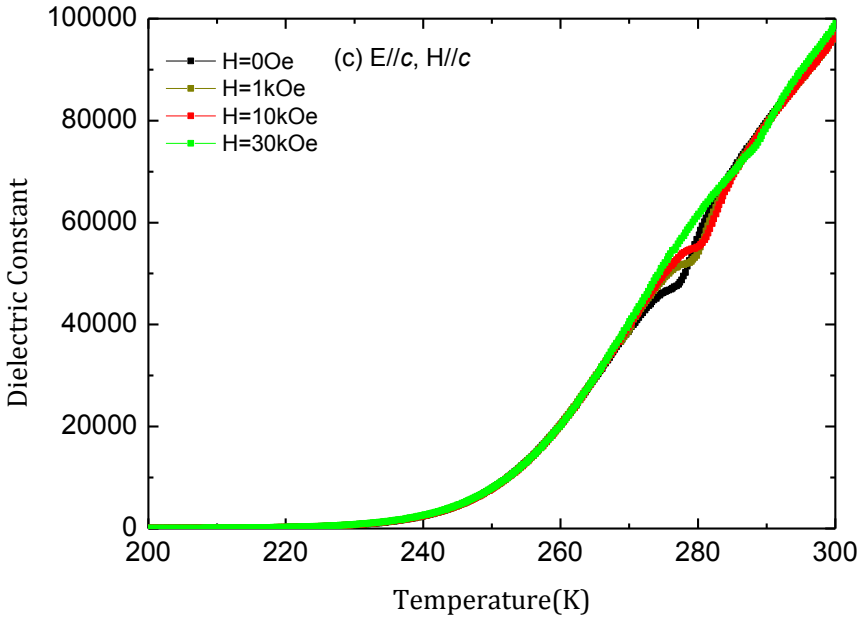

Fig. 3.14: Temperature dependence of the dielectric constant measured along the *c*-axis of the $LuFe_2O_{4-\delta}$ single crystal grown in a CO_2/CO=5 gas environment. Measurement made at 20kHz in magnetic fields applied along the (a) *a*, (b) *b* and (c) *c*-axis. Insets show a magnified view of the feature between 270 and 280K.

3.5 Polarisation

By measuring the pyroelectric current, the electric polarisation and thus the ferroelectric properties of the polycrystalline and single crystal $LuFe_2O_{4-\delta}$ samples were investigated. Data was collected from the same samples used to measure the dielectric constant. The experimental method used to determine the polarisation is described in Section 2.6.2(ii). Using the PPMS, magnetic fields of up to 30kOe were always applied parallel to the *c*-axis of the single crystal samples.

In preparation for the measurement, the samples were initially poled in an electric field. Using the same electrical contacts made for the dielectric constant measurements, a voltage of $+1kVmm^{-1}$ was applied across the sample before cooling. The sample was then cooled in a magnetic field from 320K to 200K at a rate of 3K/min. The applied voltage was then removed and the sample was connected to a bleed resistor for between 30 and 60 minutes in order to expel any surface charge built up from application of the electric field. The pyroelectric current as a function of time was then measured as the sample was heated to 320K at a sweeping rate of 2K/min.

(i) Polycrystalline Sample

The temperature dependence of the electrical polarisation of the polycrystalline sample in 0 and 30kOe applied magnetic fields is shown in Fig.3.15, respectively. In zero magnetic field, the polarisation increases markedly from zero at 275K to ~240μC/m^2 at 265K. A second, step-like feature is observed between 250 and 260K where the polarisation reaches a maximum value of ~260μC/m^2. Both the value of the polarisation and the temperature at which the sample becomes polarised increases when a 30kOe magnetic field is applied across the sample. The second feature is not as clear for the in-field measurements, however, an increase in polarisation from 450 to ~460μC/m^2 is observed from 265 to 255K.

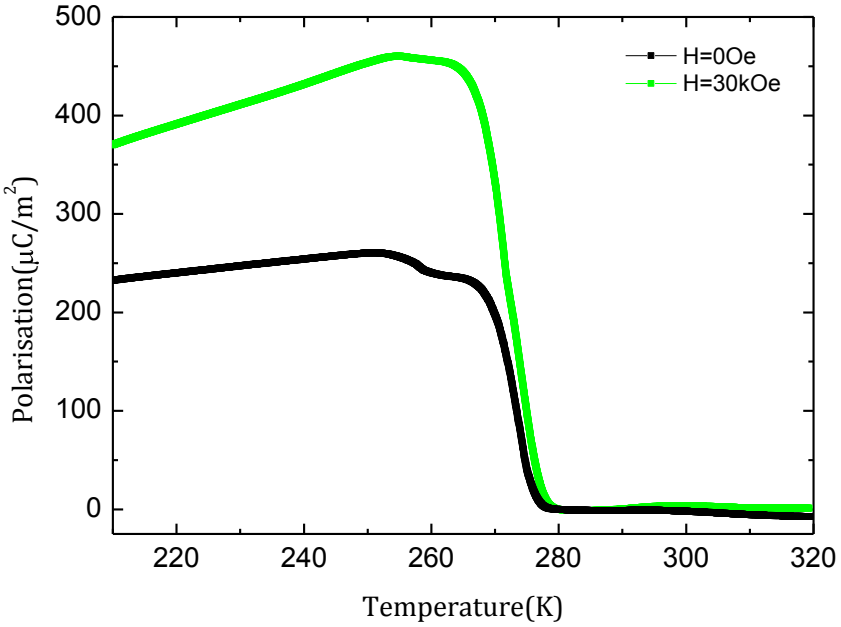

Fig. 3.15: Polarisation as a function of temperature measured for the polycrystalline $LuFe_2O_{4-\delta}$ sample in zero and 30kOe applied magnetic field.

(ii) $CO_2/CO=3$ Single Crystal

In zero magnetic field, an electrical polarisation was observed below 280K along the *c*-axis of the $CO_2/CO=3$ single crystal (Fig.3.16). A maximum polarisation of 370μC/m^2 was recorded at 265K. Below this temperature, the polarisation remains relatively constant and no addition features were observed. The maximum value of the polarisation was increased to ~390μC/m^2 when a magnetic field of 10kOe was applied parallel to the *c*-axis. The temperature of the onset of polarisation also increased with application of the

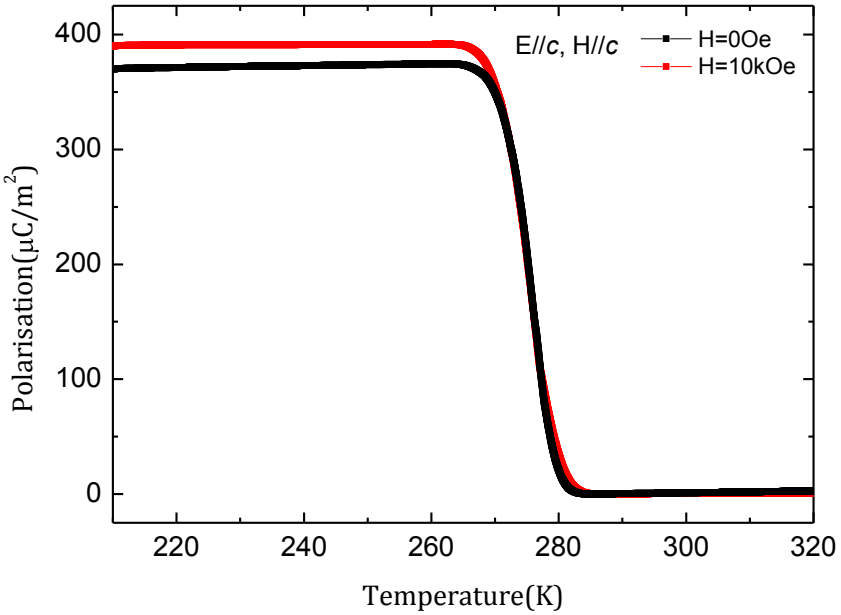

Fig. 3.16: Polarisation measured along the *c*-axis of the $LuFe_2O_{4-\delta}$ single crystal grown in a CO_2/CO=3 gas environment. Measurements made in zero and 10kOe magnetic fields applied along the *c*-axis.

magnetic field.

(iii) CO_2/CO=5 Single Crystal

The anisotropic behaviour of the polarisation along the *a*, *b*, and *c*-axes (E//*a*, *b* and *c*) was investigated for the CO_2/CO=5 single crystal, the results are shown in Fig.3.17. The zero magnetic field polarisation data along the *a*-axis shows a sharp rise at 282K. The polarisation reaches a value of ~55μC/m² at 270K and continues to rise steadily below this temperature. A slight change in the gradient is observed around 240K, this secondary feature is similar to the feature observed in the polycrystalline sample. The polarisation data collected along the *b*-axis in zero magnetic field also shows two features. An initial rise in the polarisation from zero to ~340 μC/m² between 278 and 265K is accompanied by a second feature between 240 and 245K which reaches a maximum polarisation of ~365μC/m². Only one feature is observed in the c-axis polarisation data. At 280K the sample becomes polarised and a maximum value of 220μC/m² is recorded at 270K. Below 270K, the polarisation remains relatively constant.

When magnetic fields of either 10 or 30kOe were applied parallel to the *c*-axis of the CO_2/CO=5 single crystal, the features observed in the polarisation along each crystallographic axes were found to increase in both value and temperature. For

example, the first feature observed in the polarisation along the *a*-axis increases in temperature to 285K. Similarly, the second feature in the *b*-axis polarisation reaches an increased maximum of ~380μC/m^2 at 245K. The largest change in polarisation is recorded along the *c*-axis. A magnetic field of 10kOe increases the temperature of the feature from ~280μC/m^2 to 285K and increases the maximum polarisation recorded at 270K to ~900μC/m^2.

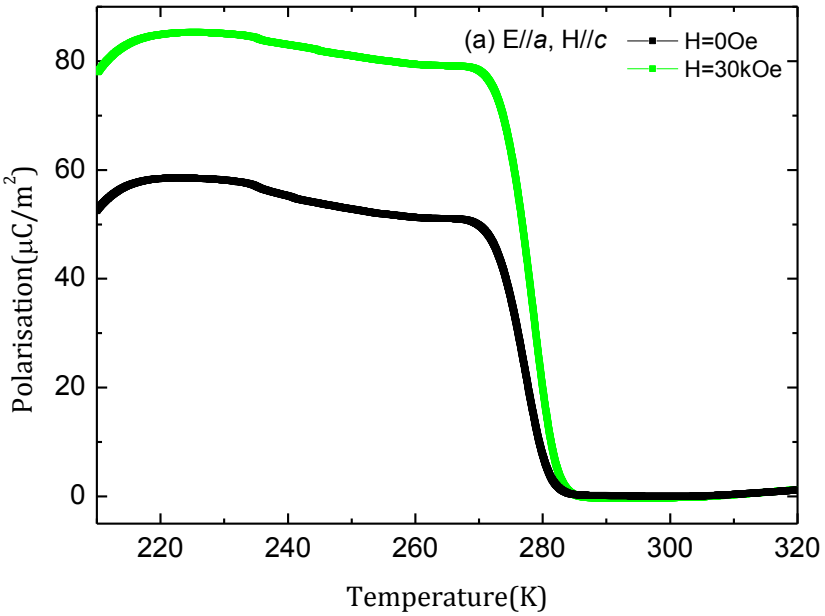

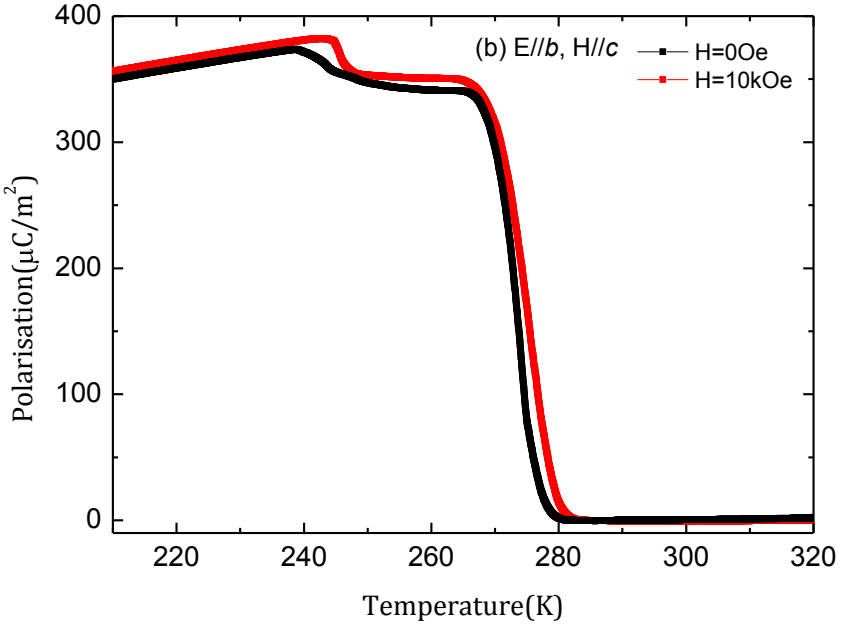

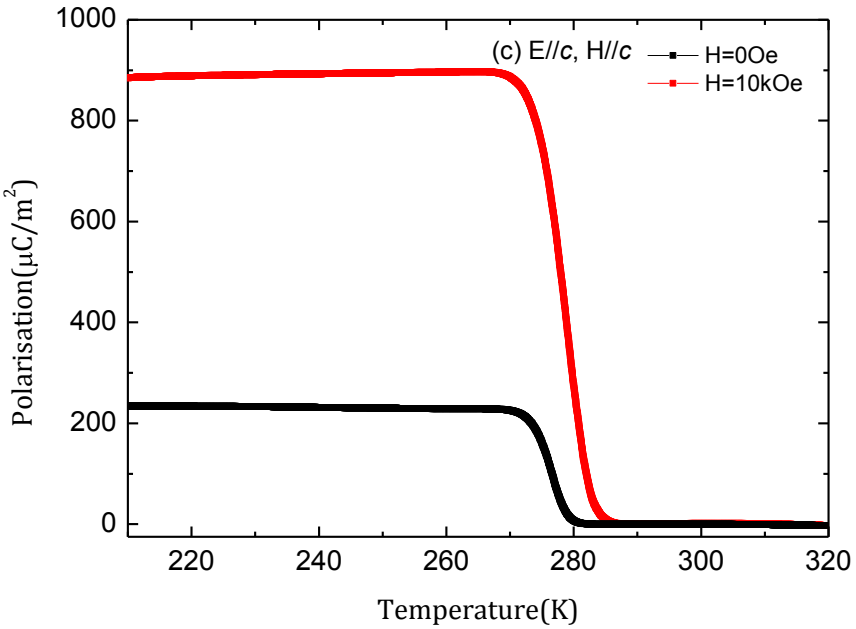

Fig. 3.17: Polarisation measured along the (a) *a*, (b) *b* and (c) *c*-axis of the $LuFe_2O_{4-\delta}$ single crystal grown in a CO_2/CO=5 gas environment. Measurements made in zero and incident magnetic fields applied along the *c*-axis.

3.6 Discussion

The difficulty in growing single crystals of $LuFe_2O_4$ with ideal oxygen stoichiometry has, in the past, hindered the understanding and development of the multiferroic properties exhibited by this material [18]. Good quality single crystals of $LuFe_2O_4$ can be grown in a floating zone furnace as has been done for the present study. The optimum conditions for sample preparation and growth, however, are not well defined. A number of different gas atmospheres and ratios have been used at the sintering stages of polycrystalline sample preparation in the reported literature. The atmosphere used during single crystal growth is a gas mixture of CO_2 and CO, however, the ratio reported to grow a crystal with ideal oxygen stoichiometry varies between papers. The sintering environments used to prepare the powders for crystal growth are rarely reported therefore it is difficult to compare the single crystal gas environments and determine the best procedure for stoichiometric growth. Iida et al. [13] is one of the few papers that gives a full account of the growth process i.e. sintering gas ratios, temperatures and times. However, this procedure does not produce the ideal stoichiometry. The sample preparation and growth procedure used in this report was decided on after a critical reading of the available literature supported by a private communication. A CO_2/CO sintering

atmosphere rather than a CO_2/H_2 atmosphere was advised to produce the ideal stoichiometry.

In order to determine whether the prepared polycrystalline and single crystal samples have the ideal oxygen stoichiometry, powder x-ray diffraction and magnetisation measurements were taken and compared with published results. The multiferroic properties were also investigated by measuring the dielectric constant and polarisation of the samples, as described in the previous sections.

In order to analyse the results and interpret the features in the data, reference has been made to published $LuFe_2O_4$ data. Ideally additional measurements should be carried out to accurately determine the spin and charge structures that occur within the samples. Future experiments are discussed in the future work section.

(i) Polycrystalline

The magnetisation data collected from the polycrystalline sample in an applied field of 1kOe (Fig.3.6), shows $LuFe_2O_{4-\delta}$ to undergo two magnetic phase transitions. The upturn of magnetisation around 260K indicates the appearance of a ferrimagnetic order between the Fe ions. The peak in the ZFC data marks the transition from paramagnetic to ferrimagnetic ordering within the Fe spin system. At this same temperature the ZFC and FC magnetisations separate as a result of the growth of magnetic domains along the direction of field cooling. The plateau observed in the ZFC data is believed to result from a modulation of Fe magnetic structure. This magnetostructural transition may account for the change in gradient observed in the FC data. Secondary features were also observed in the FC magnetisation, these features may be the result of spin glasses forming within the Fe lattice [24-26].

A number of papers have presented low field data on the ZFC and FC magnetisations in polycrystalline $LuFe_2O_4$ [38-41]. In particular, Yoshii et al. [41] have measured the magnetisation in an applied field of 1kOe. In Yoshii et al.'s paper, the ferrimagnetic ordering of the Fe spins appears around 250K . This feature is followed by a broad maximum in both the ZFC and FC data between 180 and 200K. Yoshii et al. have attributed this feature to a change in the structure of the magnetic ordering of the Fe lattice. The magnetostructural features observed by Yoshii et al. are more defined than the features measured as part of this thesis, maxima are observed in the ZFC data instead of plateaus and the FC feature reaches a global maximum instead of broad

change in gradient. This difference may be linked to the different $LuFe_2O_4$ stoichiometries, discussed later.

The magnetisation in applied fields greater than 1kOe has not been published for polycrystalline $LuFe_2O_4$. The results for the polycrystalline sample, presented as part of the present work, show the temperature at which the ferrimagnetic domains first appear to increase with increasing field strength (Fig.3.6). As discussed in Section 3.3(a), the features merge together in high magnetic fields. Both the temperature of the ZFC maxima and the temperature at which the FC data changes gradient decrease with increasing field strength. The low temperature features associated with the formation of spin glasses within the Fe spin system become less defined in high fields.

The magnetic transitions observed in the magnetisation are also present in the dielectric response of the polycrystalline sample. The correlated results are shown in Fig.3.18. The initial rise in dielectric constant occurs at the same temperature as the magnetostructural transition in the magnetisation. This is followed by a further increase in dielectric constant around 260K which coincides with the demise of the ferrimagnetic ordering with increasing temperature. The dielectric response of polycrystalline $LuFe_2O_4$ has previously been investigated by both Subramanian et al. [2] and Yoshii et al. [41]. The dielectric response in zero magnetic field presented by Subramanian et al. shows a similar rise in dielectric constant around 200K followed by a change in gradient above 250K. The origins of the features observed by Subramanian et al. have not been discussed in their paper. The dielectric response measured by Yoshii et al. shows a single rise in dielectric constant around 200K, no features were observed between 250 and 260K. In this thesis, a peak not observed in the magnetisation data, has been recorded in the dielectric response of the polycrystalline sample at 275K. A paper by Park et al. [39] shows a similar peak in the dielectric constant at this temperature. The dielectric responses recorded for this thesis, in general, have a very similar profile to Park et al's published data. Park et al. have associated the feature at ~280K with the ferroelectric transition. Charge ordering within the Fe lattice is expected to change from 2D to 3D as the temperature is decreased below 330K [3]. The dielectric frequency dispersion below 330K is dependent on the motion of the ferroelectric domain boundary. The feature observed by Park et al. moves to higher temperatures as the frequency of the ac current is increased. A similar dielectric dispersion was observed for the polycrystalline sample in this thesis (Fig.3.9). Park et al. also observed a monotonous increase in the dielectric constant closely related to the conductivity when $LuFe_2O_4$ enters the 2D charge ordered state. The dielectric constant for the polycrystalline sample in the present work shows a

similar response above 280K.

The magnetodielectric response of the polycrystalline sample was also investigated for this thesis (Fig.3.10). Contrary to results published by Subramanian et al. [2] the dielectric constant was found to increase upon application of a magnetic field. Below the magnetic ordering temperature the dielectric constant appears to be independent of the magnetic field. Dispersion amongst the responses only appears at temperatures above this transition. All the dielectric responses converge above 290K and continue to increase in the monotonous fashion expected of the 2D charge ordered state [39].

$LuFe_2O_4$ is ferroelectric within the 3D charge ordered state [3]; a polarisation is therefore expected to be induced at this transition. A polarisation was measured for the polycrystalline sample below 275K (Fig.3.15). This upturn in the polarisation coincides with the peak in the dielectric constant data, shown in Fig.3.18. The paramagnetic to ferrimagnetic ordering of the Fe spins is also observed as a step-like rise in the polarisation. The coexistence of these two features is indicative of a multiferroic. Park et al. [39] have measured the pyroelectric coefficient of their sample. The response measured by Park et al. contains two pronounced peaks: one at 250K and another at 340K. These peaks are associated with the spin and charge ordering of the Fe ions within the W layer. The peak at the magnetic ordering temperature in Park et al's pyroelectric coefficient data is much stronger than the peak representing the 2D to 3D charge ordering. In Park et al's results, the charge ordering appears to occur at the same temperature as the dip in the dielectric constant and not at the peak observed at ~280K.

The temperature of the ferroelectric transition, measured in this work, was found to increase when a magnetic field was applied across the polycrystalline sample. The peak in the dielectric constant was found to increase to a similar temperature (Fig.3.18).

(ii) Single Crystal

A Rietveld refinement of the X-ray powder diffraction data collected from the single crystals provided an estimate of the lattice constant for each crystal (Table 3.2). The refined lattice constants for the crystal grown in $CO_2/CO=5$ gas environment match the lattice constant reported by [21]. The lattice constant estimated for the $CO_2/CO=3$ single crystal are larger than those estimated for the $CO_2/CO=5$ single crystal.

The magnetisations of the $CO_2/CO=3$ and $CO_2/CO=5$ single crystals, measured for this

thesis, were found to be greatest when magnetic field were applied parallel to the *c*-axis (Fig. 3.7, 3.8). A magnetic anisotropy along the *c*-axis is expected as the Fe spins lie parallel to the *c*-axis inducing a ferrimagnetic moment along this direction [28]. The magnetisation, in general, was found to be greater for the CO_2/CO=5 crystal (Fig.3.8). The magnetic anisotropy within single crystal $LuFe_2O_4$ has previously been investigated by Kim et al. [28]. The temperature dependence of the ZFC and FC magnetisations reported by Kim et al. for magnetic field applied parallel and perpendicular to the *c*-axis are very similar to the response for the CO_2/CO=5 single crystal measured in this thesis. In an applied field of 1kOe, the magnetisation along the *a*, *b* and *c*-axes of the CO_2/CO=5 crystal show two magnetic phase transitions. The rise in the magnetisation around 250K marks the appearance of ferrimagnetic ordering within the Fe spins system and the peaks in the ZFC data along the *a*, *b* and *c* axes denotes the temperature of the paramagnetic to ferrimagnetic transition. The peaks are then followed by a plateau in the ZFC data and a broad maximum in the FC data. These features indicate the presence of a magnetostructural transition within the Fe lattice. The feature in the FC data is more pronounced in the CO_2/CO=5 single crystal than in the polycrystalline sample previously reported. The 1kOe magnetisations show a discrepancy between the ZFC and FC curves along all three axes of the CO_2/CO=5 single crystal. The peak in the ZFC data does not align with the FC data. A similar observation has been made by Park et al. [39]. They have attributed this discrepancy to the existence of short-range magnetic clusters above the ferrimagnetic ordering temperature.

Only one magnetic transition is observed for the CO_2/CO=3 single crystal grown in this study (Fig.3.7). A rise in magnetisation is recorded around 250K when a field of 1kOe is applied across the sample. The Fe spins order ferrimagnetically at 197 and 204K for fields applied parallel and perpendicular to the *c*-axes, respectively.

The magnetic behaviour of $LuFe_2O_4$ is qualitatively similar to YFe_2O_4 [18]. A previous investigation into the effect of oxygen concentration in YFe_2O_4 showed that stoichiometric samples are characterised by much sharper magnetic transitions [42]. This observation lead Christianson et al. [18] to take the sharpness of observed transitions as an indication of ideal oxygen stoichiometry within their $LuFe_2O_4$ single crystal samples. In this thesis, the CO_2/CO=5 crystal is expected to have a stoichiometry closer to the ideal than the CO_2/CO=3 single crystal. The stoichiometric study conducted by Michiuchi et al. [27] concluded that the crystal grown in the CO_2/CO=6 environment developed the most complete charge ordering with largest coherence length, properties indicative of ideal stoichiometry. The FC magnetisation reported by Michiuchi et al. for

their $CO_2/CO=6$ crystal shows a well defined feature at 200K, a feature absent in the other crystals reported in their paper.

The dielectric responses of the $CO_2/CO=3$ and $CO_2/CO=5$ single crystals measured along the *c*-axis in this thesis do not show features at the paramagnetic-ferrimagnetic ordering temperature or the magnetostructural transition (Fig.3.19, 3.22). The dielectric responses in zero magnetic field typically show an initial rise in dielectric constant between 220 and 230K, followed by an increase in gradient around 280K. The dielectric constant continues to rise monotonously above this temperature. This feature is accompanied by the development of a polarisation below 280K. Ikeda et al. [17] have also measured the dielectric constant and polarisation along the *c*-axis of a $LuFe_2O_4$ single crystal. The low temperature dielectric response measured by Ikeda et al. has a similar profile to the $CO_2/CO=3$ and $CO_2/CO=5$ single crystals measured in the present work. Ikeda et al.'s results, however, show a small dip in the 10kHz measurement at 280K followed by steady rise to a step-like jump at 330K. The polarisation, measured by Ikeda et al., was shown to accompany this room temperature feature. These observations lead Ikeda et al. to propose a 2D to 3D charge ordering temperature of 330K. The magnetic ordering of the Fe spins was also observed as an increase in polarisation at 250K. No room temperature (330K) features were observed in either of the dielectric constant or polarisation measurements taken from the $CO_2/CO=3$ or $CO_2/CO=5$ single crystals grown for this thesis. The dielectric response of the $CO_2/CO=3$ crystal along the *c*-axis shows a decrease in dielectric constant at 275K upon application of a magnetic field. A similar observation was made by Subramanian et al. [2] for polycrystalline $LuFe_2O_4$. Subramanian et al. related this decrease to the decrease in polarisability of the system. Fluctuating dipoles are frozen on cooling through the ferroelectric transition, polarisability is consequently lost and the dielectric constant decreases. The system is expected to become polarised upon application of a magnetic field as a result of the Fe^{3+} ions being more strongly attracted to the field than the Fe^{2+} ions. The system becomes more polarised therefore loosing polarisability [2]. In the present work, the magnetodielectric response along the *c*-axis of the $CO_2/CO=5$ crystal is not as clearly distributed. Magnetic fields applied along the *c*-axis appear to increase the dielectric constant at 270K. A change in gradient of the responses between 275 and 280K result in the lower fields having a higher dielectric constant than the high field measurements.

In this thesis, the dielectric responses along the *a* and *b*-axes of the $CO_2/C0=5$ single crystal have a similar profile to the polycrystalline sample reported in Section 3.4(a). The initial rise in the dielectric constant measured along the *a* and *b*-axes of the $CO_2/C0=5$

single crystal occurs at the same temperature as the magnetostructural feature in the magnetisation data, shown in Fig.3.20, 3.21. As the temperature is increased, the crest of a broad step-like feature in the dielectric constant coincides with the peak in the ZFC magnetisation. The upturn in magnetisation between 250 and 260K is also observed as a feature in the dielectric response and polarisation. Both of these features are related to the onset of ferrimagnetic ordering of the Fe spins and demonstrate the multiferroic behaviour indicative of $LuFe_2O_4$. The dielectric response measured along the *a*-axis shows a well defined peak at 270K, in zero magnetic field. A ferroelectric transition is observed in the polarisation measurements along the *a*-axis at this temperature. Above 280K the dielectric constant increases monotonously and the system enters a paraelectric state. The dielectric response along the *b*-axis also exhibits a ferroelectric transition around 270K, however, it appears as a cusp rather than a well defined peak. The dielectric constant then shoots off to very high values as it approaches 280K. Ikeda et al. have also measured the dielectric constant perpendicular to the *c*-axis. At low temperatures, the dielectric constant measured by Ikeda et al. [17] (Fig.1.12) appears to be independent of the temperature; it is only above 150K that the dielectric constant begins to rise. A step-like feature similar to that observed in this study for the CO_2/CO=5 single crystal occurs around the magnetic ordering transitions. The dielectric constant reported by Ikeda et al. reaches a plateau then continues to rise again around 350K marking the 3D to 2D charge order transition. The basic profile of the Ikeda et al's dielectric constant data is the same as the *a* and *b*-axes results obtain for this thesis, however, on closer inspection the features associated with magnetic transitions are at very different temperatures.

The magnetodielectric responses along the *a*-axis of the CO_2/C0=5 single crystal, measured for this study, clearly show that, independent of the direction of the applied field, a larger magnetic field induces a larger dielectric constant between 250 and 290K. Below 250K, the ordering of the responses appears to be dependent on the orientation of the field. For example, below 250K the dielectric constant decreases with increasing field strength along the *b*-axis whereas increasing magnetic strength along the *c*-axis increases the value of the response. Magnetic field applied along the *a*-axis reduce the dielectric constant below the zero field value, however, at this lower value the responses are generally larger for the stronger magnetic fields. Above 290K, all the responses converge. A similar pattern was observed for the *b*-axis of the CO_2/C0=5 single crystal. A pattern can be observed in the ordering of the dielectric responses along the *a* and *b*-axis with respect to field strength. Below 250K, the dielectric response induced along the *a*-axis when fields are applied along the *b*-axis has the same form as the response

measured along the *b*-axis when fields are applied along the *a*-axis. Similarly, magnetic fields applied along the *c*-axis induce the same pattern along the *a* and *b*-axis. A pairing can also be made between responses that are measured along the same axis as the applied field.

Two different plate thicknesses were used to measure the dielectric constant along the *b*-axis of the CO_2/CO=5 single crystal. The thickest plate was used when measuring the response of magnetic fields applied along the *b*-axis (Fig.3.13(b)). The cusp-like feature associated with the ferroelectric transition is lower in both temperature and value in this case. A second feature emerges and rises to higher temperatures as the magnetic field strength increases. Polarisation measurements were not taken for the thicker plate as the poling voltage required was beyond the limits of the power supply. The polarisation results for the thinner sample show the existence of a ferroelectric state below 280K which shows an increase in polarisation around 250K. These features suggest a 2D to 3D charge ordering of the Fe ions around 280K followed by a ferrimagnetic ordering of the spins below 250K.

The room temperature resistance of the *b*-axis plate was found to be much lower than the *a* and *c*-axis plates. Consequently, the conductivity along this axis is expected to be much higher. This may explain the large difference in dielectric constant values between the oriented plates and with other published results in general. The effect of conductivity on the dielectric constant has previously been noted in $YCrO_3$. Serrao et al. [43] have associated a monotonous increase in dielectric constant above the ferroelectric transition with the dc conduction of the sample. At high temperatures, Serrao et al. recorded a large dc leakage current for low frequency measurements. The dissipation factors at room temperature were also recorded as being much higher in thin films than the bulk samples [38]. Current leakage may account for the different dielectric constants recorded for the thick and thin CO_2/CO=5 *b*-axis plates prepared as part of this thesis. Sample conductivity also needs to be considered for polarisation measurements. When estimating the polarisation from the pyroelectric current data, Ikeda et al. [17] have assumed that the polarisation is zero above 350K to avoid any errors caused by the increase of electrical conductivity. The change in polarisation recorded at 330K by Ikeda et al. is much larger than the change recorded at 240K (Fig.1.11). The magnitudes of the pyroelectric coefficient peaks recorded by Park et al. [39] imply the opposite is true. Sample conductivity may be responsible for this discrepancy. Alternatively, the peak observed by Park et al. at 340K is a consequence of increased conductivity and is not a true representation of the polarisation of the system as no peak is observed in their

dielectric constant data at this temperature.

In this thesis, the dielectric constant and polarisation were initially recorded up to temperatures of 360K. No further features were observed in the dielectric response above 290K; the dielectric constant continued to increase reaching extremely high values. In the case of the polarisation, the pyroelectric current signal became increasingly noisy at high temperatures and no further features could be defined. The high conductivity of the samples at room temperature may distort or hide the true position of the 2D to 3D charge ordering transition. This may explain the difference in the results reported in this thesis and those published by other research groups.

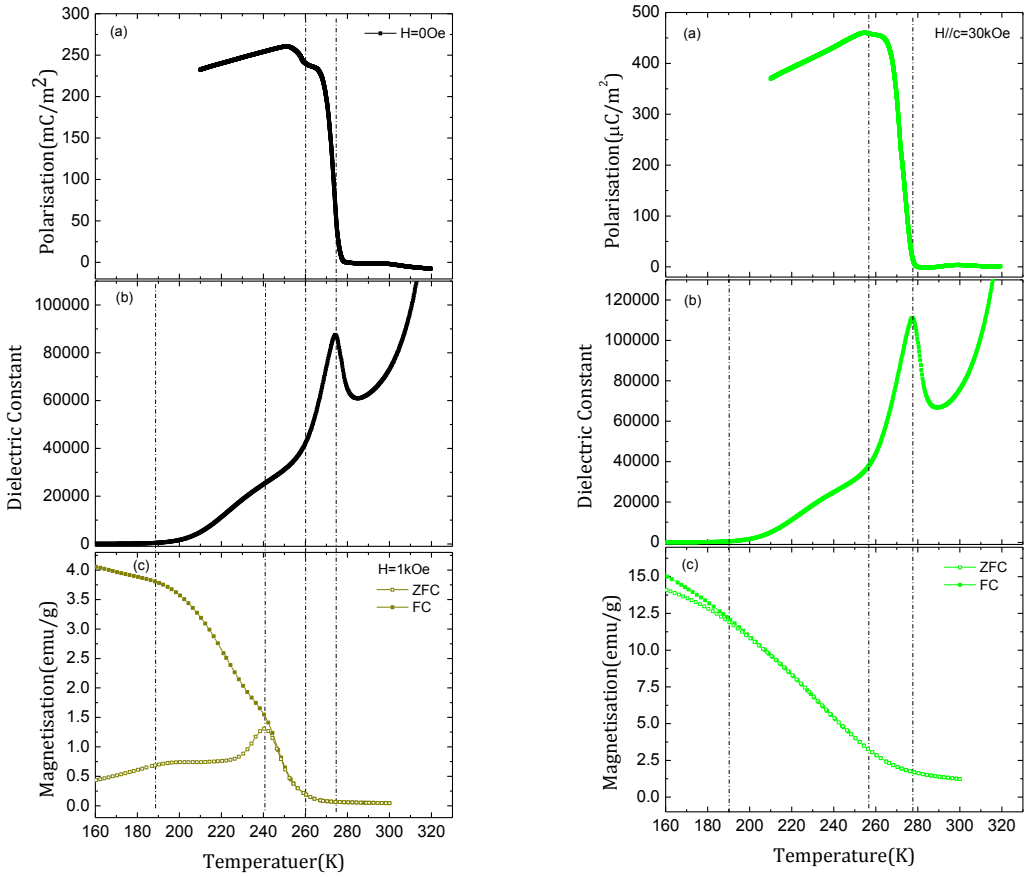

Fig. 3.18: (a) Polarisation and (b) dielectric constant and (c) ZFC and FC magnetisation of polycrystalline $LuFe_2O_{4-\delta}$ in (i) 0, 1kOe and (ii) 30kOe magnetic fields.

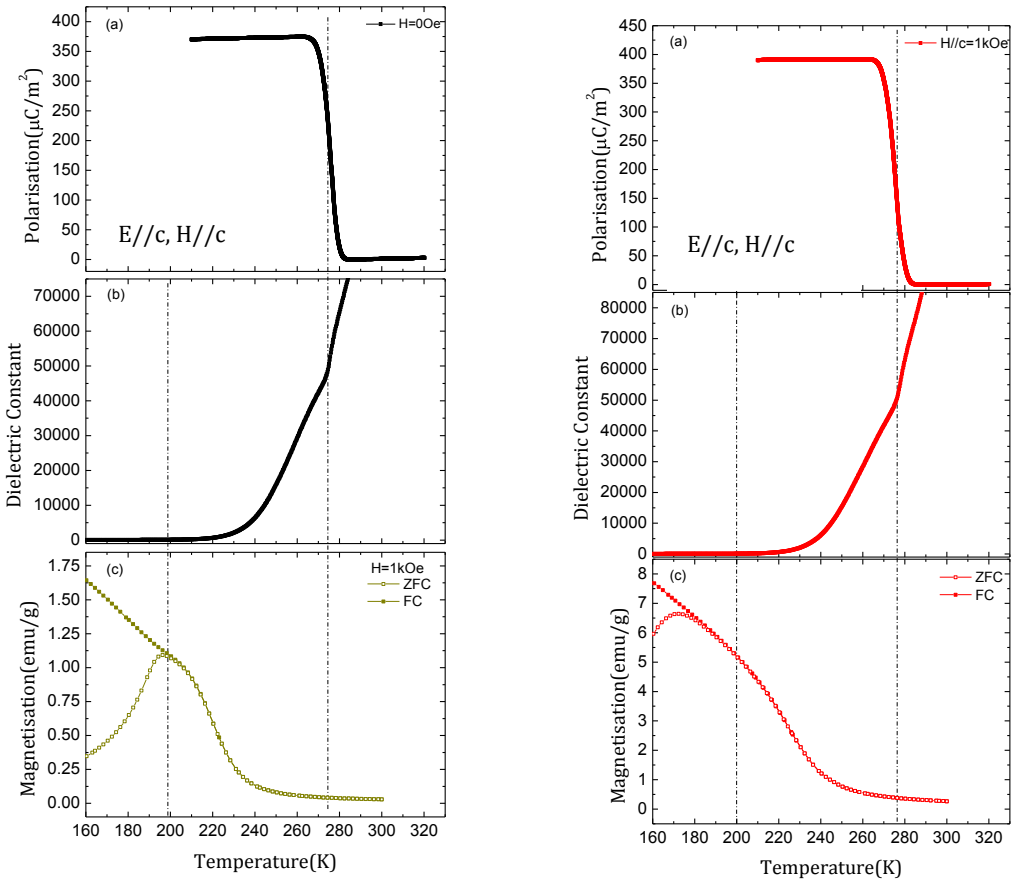

Fig. 3.19: (a) Polarisation and (b) dielectric constant and (c) ZFC and FC magnetisation measured along the *c*-axis of the CO_2/CO=3 $LuFe_2O_{4-\delta}$ single crystal in (i) 0, 1kOe and (ii)10kOe magnetic fields applied along the *c*-axis.

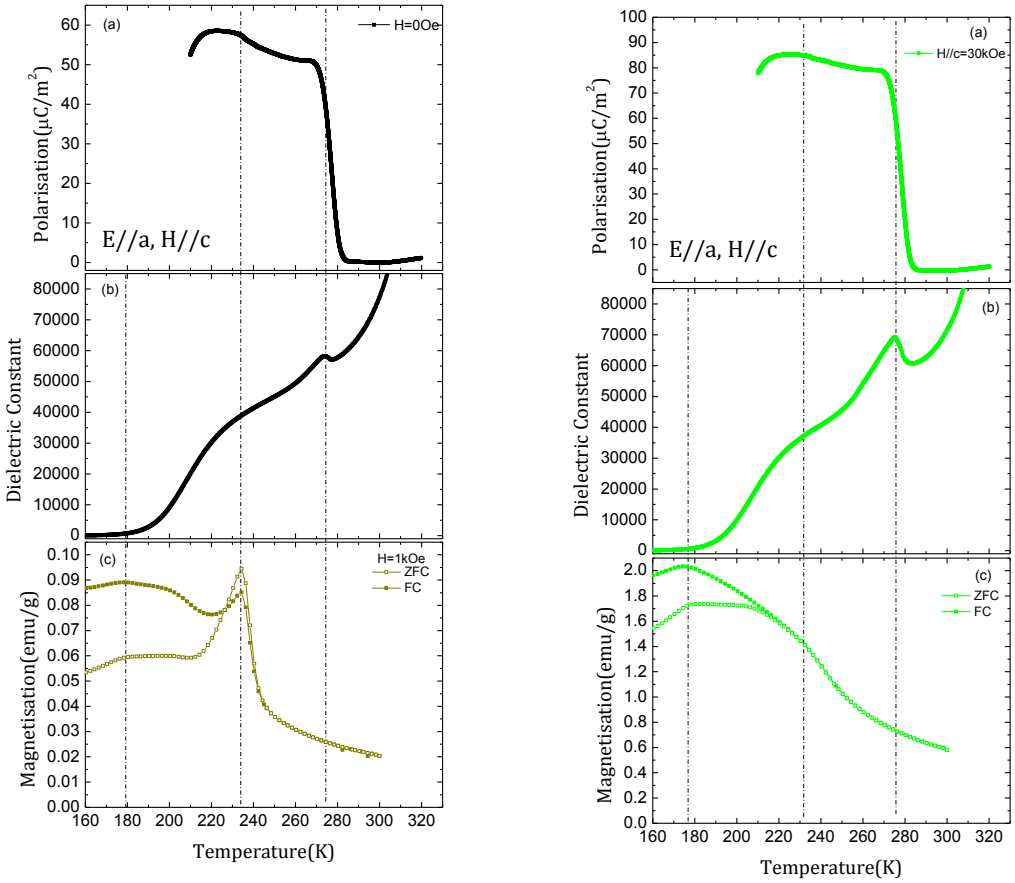

Fig. 3.20: (a) Polarisation and (b) dielectric constant and (c) ZFC and FC magnetisation measured along the *a*-axis of the CO_2/CO=5 $LuFe_2O_{4-\delta}$ single crystal in (i) 0, 1kOe and (ii)30kOe magnetic fields applied along the *c*-axis.

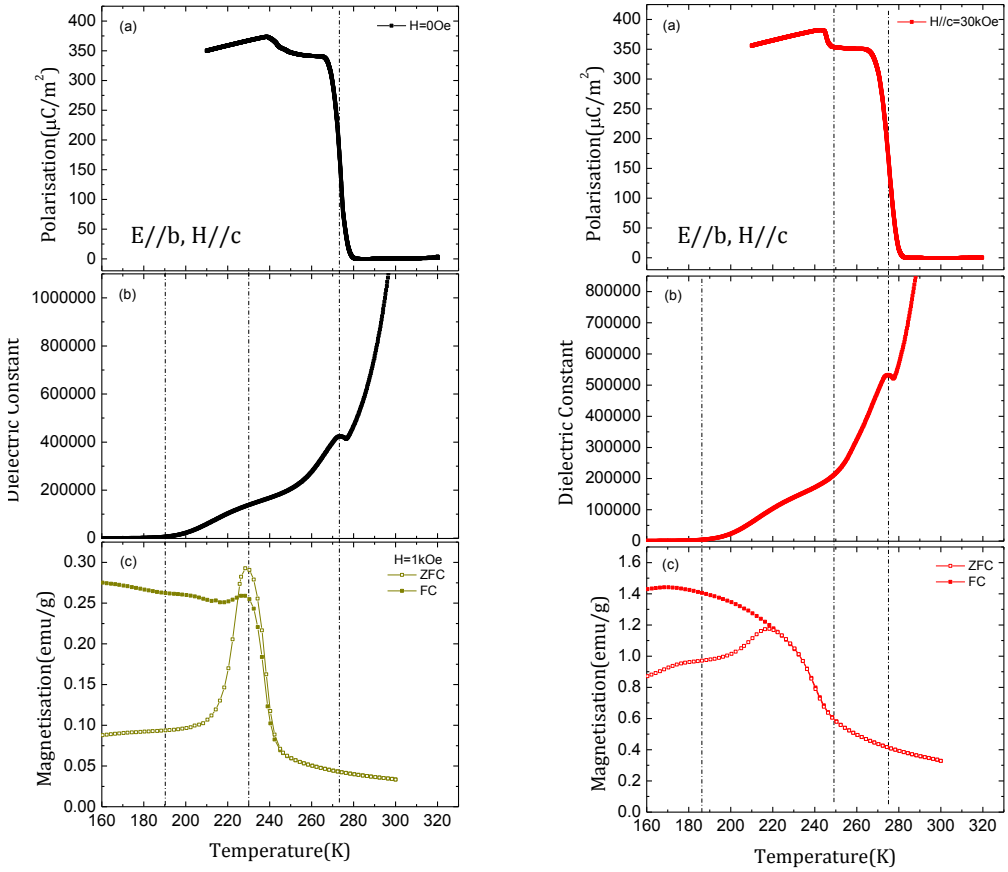

Fig. 3.21: (a) Polarisation and (b) dielectric constant and (c) ZFC and FC magnetisation measured along the *b*-axis of the CO_2/CO=5 $LuFe_2O_{4-\delta}$ single crystal in (i) 0, 1kOe and (ii)10kOe magnetic fields applied along the *c*-axis.

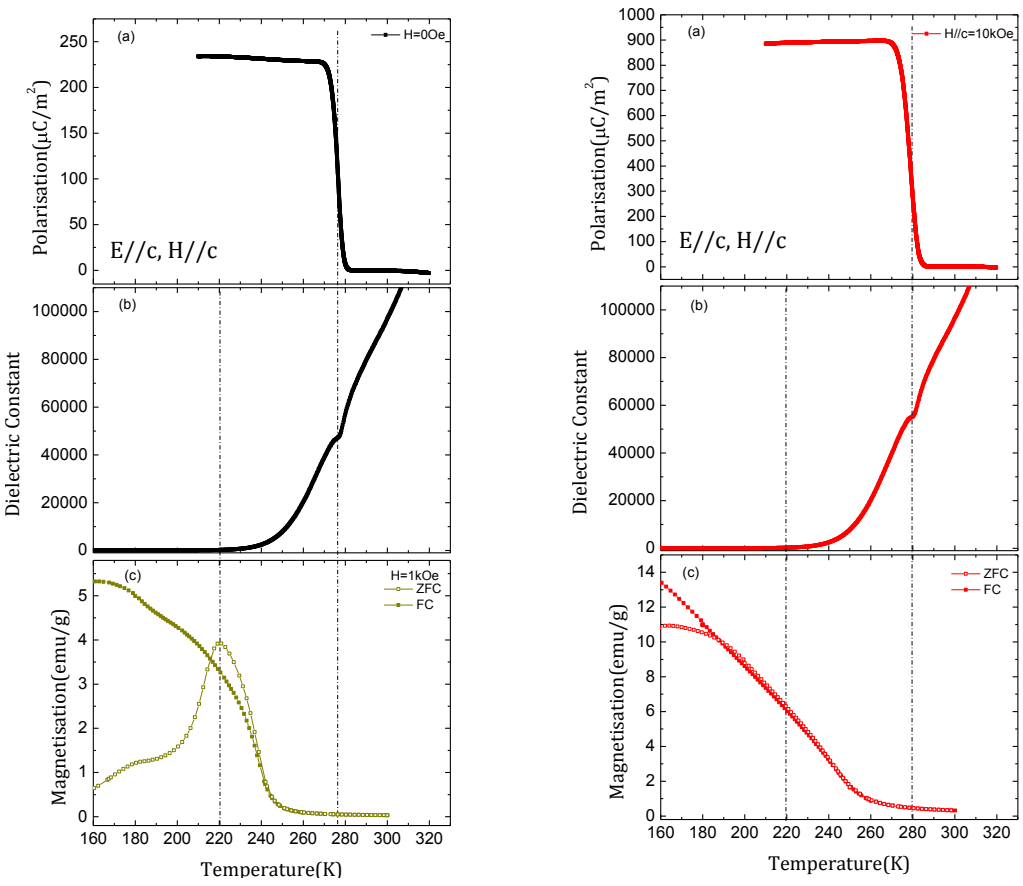

Fig. 3.22: (a) Polarisation and (b) dielectric constant and (c) ZFC and FC magnetisation measured along the *c*-axis of the CO_2/CO=5 $LuFe_2O_{4-\delta}$ single crystal in (i) 0, 1kOe and (ii)10kOe magnetic fields applied along the *c*-axis.

4.7 Conclusion

A study investigating the multiferroic properties of polycrystalline and single crystal $LuFe_2O_{4-\delta}$ has been presented.

Two single crystals of $LuFe_2O_{4-\delta}$ were successfully grown at the University of Warwick using the floating zone method. By altering the atmosphere in which they were grown, single crystals of different stoichiometry have been prepared. Crystals were grown in two different CO_2/CO gas atmospheres: CO_2/CO=3 and CO_2/CO=5. Powder X-ray diffraction data collected from the single crystals showed single phase formation. Refinement of this data allowed for an estimate of the lattice parameters to be obtained. Laue X-ray diffraction was used to accurately orientate the single crystals for experimentation.

A magnetic anisotropy along the *c*-axis was demonstrated in both of the $LuFe_2O_{4-\delta}$ single crystals. The ferrimagnetic ordering of the Fe moments along the *c*-axis was typically

observed below 250K. A magnetostructural transition was also observed below 200K in the magnetisation data collected from the polycrystalline sample and the single crystal grown in the $CO_2/CO=5$ gas atmosphere. The absence of this feature in the data collected from the single crystal grown in the $CO_2/CO=3$ gas atmosphere is an indication of poor oxygen stoichiometry within this crystal. The ferrimagnetic ordering and magnetostructural transitions were also present in the dielectric constant and polarisation data collected from the samples, thereby confirming the multiferroic nature of $LuFe_2O_4$.

A ferroelectric state was observed in the polycrystalline and single crystal samples below 280K. The polarisation data presented in this thesis demonstrate very clearly the onset of the ferroelectric order. This is the only unambiguous data, presented after the initial data reported by Ikeda et al. [17], that has ever been reproduced in the literature. $LuFe_2O_4$ is reported in the literature to enter a ferroelectric 3D charge ordered state below 330K. The disagreement with the literature may be caused by the high conductivity expected due the very low resistance of the samples at room temperature. Current leakage may distort the polarisation and account for the very high dielectric constant measured in the samples at room temperature. Further work should confirm if conductivity is an issue with these samples. The exact oxygen content of these samples has still to be confirmed, which may explain any discrepancies with the published data.

4.8 Further Work

The exact oxygen stoichiometry of the two $LuFe_2O_{4-\delta}$ single crystals was originally going to be determined by thermogravimetric analysis(TGA). This technique uses information from the mass of oxygen lost when $LuFe_2O_{4-\delta}$ decomposes into Lu_2O_3 and Fe. The combination of the high temperature and the H_2 in the H_2:Ar reducing atmosphere required for TGA of this material [25] was found to damage the sensor, consequently stoichiometric analysis of the crystals could not be completed in time for this thesis. Alternatively, neutron powder diffraction can be used to accurately determine the oxygen occupancies in the crystal structure. The oxygen content of the single crystals will be estimated using this technique in due course using the GEM Express service at ISIS.

Pieces of single crystals grown as part of this work have been given to a number of other research groups. The chemistry department at the University of Warwick is currently investigating the high temperature phase changes which occur in $LuFe_2O_4$ when heated

in an oxygen rich atmosphere. A group at the University of Boston, MA, will be carrying out optical spectroscopy experiments on the crystals and Prof. Jianqi Li at the Institute of Physics, Chinese Academy of Science is using electron microscopy to investigate the $LuFe_2O_{4-\delta}$ charge ordering.

A paper on the single crystal growth of $LuFe_2O_{4-\delta}$ and the experimental investigation made as part of this thesis is currently in production.

Chapter 4

Multiferroic Properties of $Gd_{0.9}Lu_{0.1}MnO_3$

The coexistence of ferroelectricity and magnetism within the orthorhombic perovskite manganites $RMnO_3$ was first discovered in $TbMnO_3$ [29]. The magnetic and electric properties within this series have been found to depend strongly on the magnitude of the Mn-O-Mn bonding angle [33]. By tuning the MnO_6 structure through changes in the rare-earth ionic radius, the series transforms from non-magnetoelectric to magnetoelectric with decreasing ionic radii [44]. The ability to control this structural parameter and therefore the multiferroic properties within this series has created much interest in these materials.

This chapter builds on work from a PhD thesis investigating rare-earth manganite materials of the form $RMnO_3$ and $R_{1-x}Y_xMnO_3$, where R is a rare earth element, which has recently been completed by D. O'Flynn in the Superconductivity and Magnetism Group at the University of Warwick [10, 36]. In particular, the discovery by O'Flynn of a new group of multiferroic compounds of the form $Sm_{1-x}Y_xMnO_3$ (x=0.4, 0.5), discussed in Section 1.3, has motivated research at Warwick into the effect of doping at the rare-earth site of other members of the orthorhombic series which lie near the multiferroic boundary. Studies into the multiferroic properties of single crystals of $Gd_{1-x}Y_xMnO_3$ and $Gd_{1-x}Lu_xMnO_3$ are ongoing within the department.

This thesis reports on the magnetisation, heat capacity, dielectric constant and polarisation measurements which have been carried out on an oriented single crystal of $Gd_{0.9}Lu_{0.1}MnO_3$. Powder x-ray diffraction data has also been collected for the polycrystalline feed rod used to grow the single crystal, completing Mn-O-Mn bond angle analysis on this material. The $Gd_{1-x}Lu_xMnO_3$ series are a new member of orthorhombic manganites; no data has been published on this series. Preliminary investigations have indicated that the compounds with a Lu content of x=0.1 show the most interesting magnetic and electric properties. For this report, we restrict ourselves to investigations on the x=0.1 single crystal.

4.1 Powder x-ray diffraction

A high resolution powder x-ray diffraction pattern of the polycrystalline $Gd_{0.9}Lu_{0.1}MnO_3$ sample used to grow the single crystal was collected using a Panalytical X'Pert Pro multipurpose x-ray diffraction system. By performing a Rietveld refinement on the diffraction data, shown in Fig.4.1, information on the lattice constants and Mn-O-Mn bond angles were obtained. The ratio of Lu and Gd occupying the rare-earth sites was also determined. The results are shown in Table 4.1. The $RMnO_3$ crystal structure contains two different Mn-O-Mn bond angle, φ_1 and φ_2 [10]. In order to calculate the average Mn-O-Mn bond angle, φ, the correct weighting must be given to each angle, thus $\varphi = (2\,\varphi_1 + 4\,\varphi_2)/6 = 145.39(78)°$.

	$Gd_{1-x}Lu_xMnO_3$
***a*(Å)**	5.84246(5)
***b*(Å)**	7.42233(5)
***c*(Å)**	5.30455(4)
φ_1 (°)	143.40(62)
φ_2 (°)	146.38(48)
Nominal x	0.1
Refined x	0.0921(394)

Table 4.1: Lattice parameters and Mn-O-Mn bond angles for $Gd_{0.9}Lu_{0.1}MnO_3$ from refined powder x-ray diffraction data.

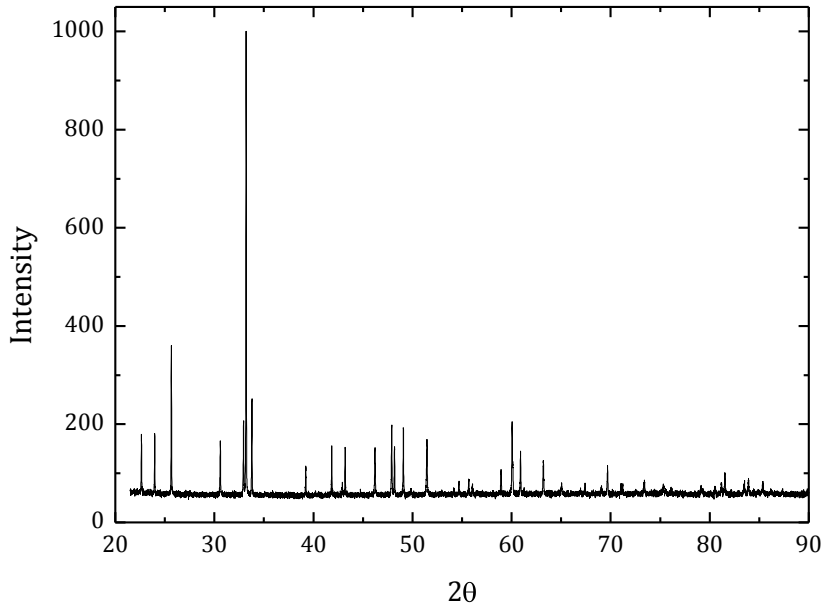

Fig.4.1: Powder X-ray diffraction pattern for polycrystalline $Gd_{0.9}Lu_{0.1}MnO_3$.

4.2 Magnetic Properties

In order to understand the magnetic response of the $Gd_{0.9}Lu_{0.1}MnO_3$ single crystal, the magnetisation as a function of temperature was measured along the crystallographic *a* and *b*-axes. Field cooled measurements ranging from 1 to 50kOe were carried out using the SQUID, described in Section 2.5. Magnetisation data was collected during heating from 2K to 60K at a sweeping rate of 1K/min. The magnetic response along the *a* and *b*-axes, shown in Fig.4.2, are very similar, both show a gradual increase in magnetisation with decreasing temperature. No sudden jumps are observed. The data shows a systematic increase in magnetisation with increasing magnetic field along both orientations.

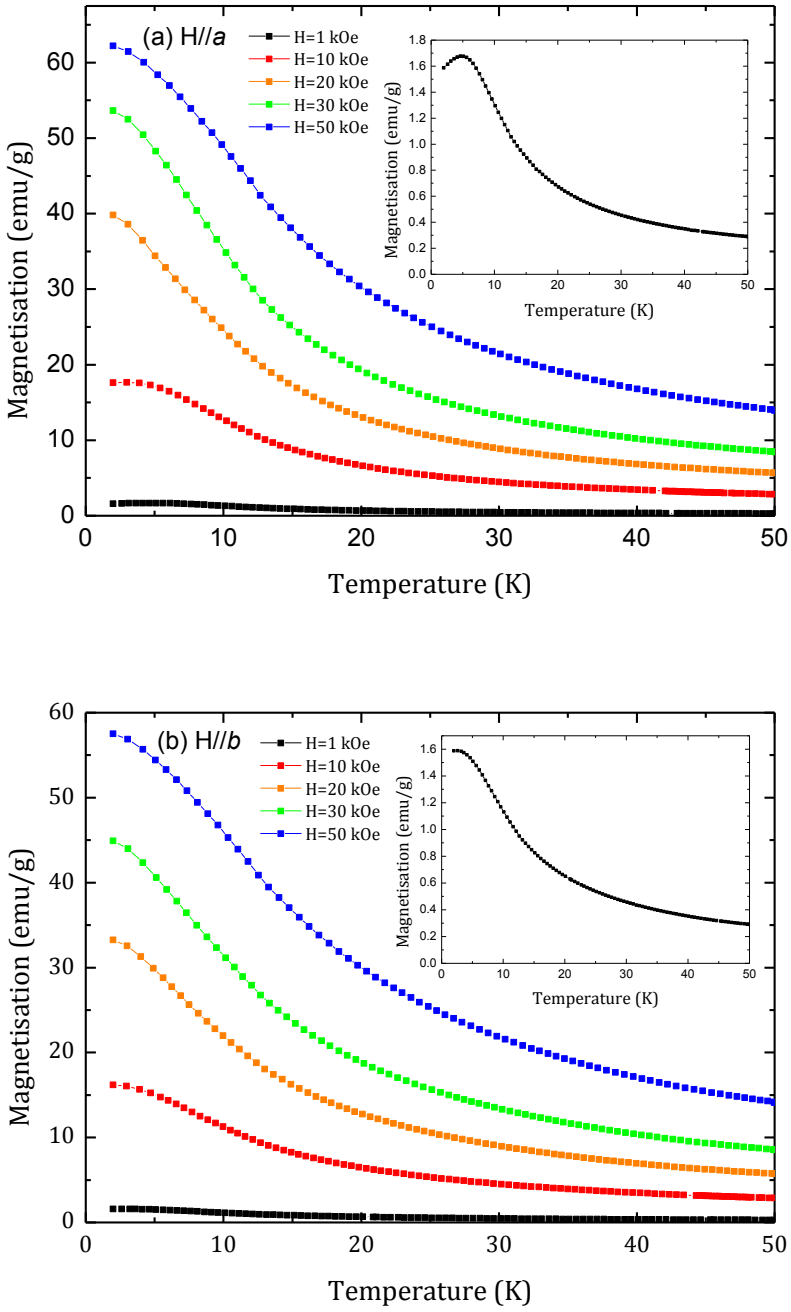

Fig. 4.2: Temperature dependence of the FC magnetisation for single crystal $Gd_{0.9}Lu_{0.1}MnO_3$. Measurements taken in magnetic fields applied along the (a) *a* and (b) *b*-axes. Insets show a magnified view of the data collected in a 1kOe field.

4.3 Heat Capacity

The heat capacity of the $Gd_{0.9}Lu_{0.1}MnO_3$ single crystal in zero magnetic field was measured using the method described in Section 2.6.1. In order to fit the addenda, data was collected over a large temperature range, 1.85 to 290K. Fig.4.3 shows the heat capacity between 1.85 and 60K, the region of particular interest. The heat capacity data shows two features below 60K: a sharp peak at 41.7K followed by a shallow rise in heat capacity below 13K which reaches a broad peak at 5.8K.

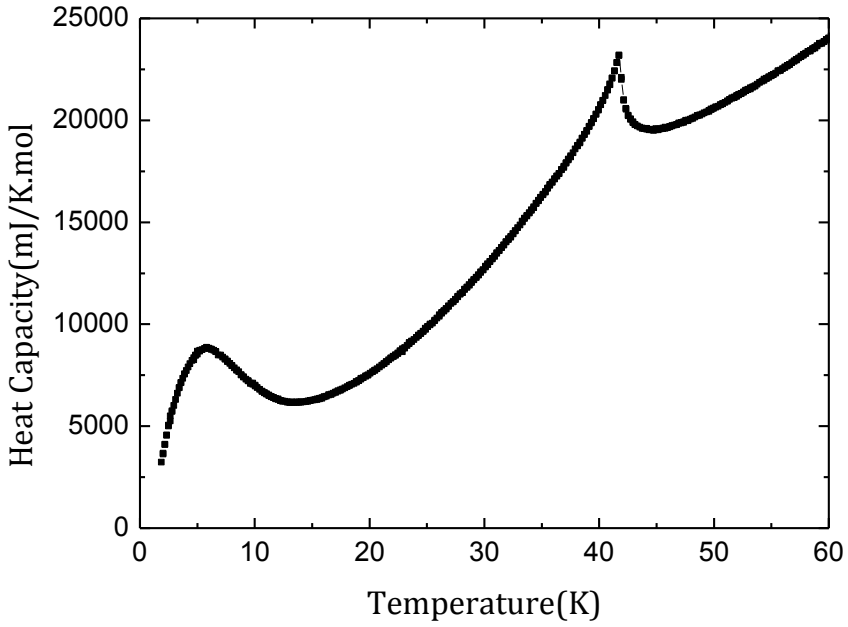

Fig. 4.3: Heat Capacity as a function temperature for single crystal $Gd_{0.9}Lu_{0.1}MnO_3$ measured in zero magnetic field.

4.4 Dielectric Properties

Using the method detailed in Section 2.6.2, dielectric constant versus temperature data was collected for the $Gd_{0.9}Lu_{0.1}MnO_3$ single crystal. The dielectric response was investigated for electric fields applied along the *a*-axis, the direction reported as showing the greatest response in pure $GdMnO_3$. A thin plate was cut from the single crystal along the *b*-*c* plane, allowing for an electric field to be applied parallel to the *a*-axis. Electrical contacts identical to those described in Section 2.6.2 were made with the oriented crystal. Using the PPMS insert, measurements were carried out in magnetic fields of up to 90kOe applied along each of the principle crystallographic axes.

The sample was cooled in a magnetic field from 60K to 10K at a rate of 5K/min then further cooled at a rate of 2K/min down to 2K. The capacitance as a function of temperature was then measured from 2K to 60K at a sweeping rate of 1K/min. The dielectric constant of the sample was calculated for the 10kHz measurements. The magnetodielectric response along the *a*-axis is shown in Fig.4.4.

(i) Zero field

In zero magnetic field, the dielectric constant data for $Gd_{0.9}Lu_{0.1}MnO_3$ shows two features: a step-like jump below 10K followed by a peak in the response at ~16K. The dielectric constant has an initial value of ~27 at 2K which rises to ~33 at the first feature then reaches a maximum value of ~62 at the second feature. Above 16K, the value of the dielectric constant exponentially decreases to a constant value of ~24 at 43K.

(ii) H//a

Magnetic fields of 10, 30, 50 and 90kOe were applied parallel to the *a*-axis, the data is shown in Fig.4.4(a). The dielectric response of the 10kOe field is almost identical to the zero field measurement; the features occur at a similar temperature and value to those described for the zero field data. However, subtle differences do exist between the two results. A small reduction in the maximum value of the dielectric constant occurs when the 10kOe field is applied along the *a*-axis. Also, the step-like feature observed in the 10kOe response is not as sharp as the feature present in the zero field data. This feature disappears for fields greater than 10kOe. Only one feature is present in the dielectric response when 30, 50 and 90kOe magnetic fields are applied. The higher magnetic fields reduce the maximum value of the dielectric constant, lowering it to ~57, ~37 and ~33 for 30, 50 and 90kOe fields, respectively. The temperature at which the feature occurs is also dependent on the strength of the magnetic field. Initially, the feature moves to lower temperatures, ~14K in a 30kOe field. The feature then shifts to higher temperatures in larger magnetic fields, ~17K and ~20K for 50 and 90kOe fields, respectively. The general shape of the feature also changes with increasing magnetic field. The feature in the 30kOe response is broader than that observed in the zero and 10kOe field data. This is in stark contrast to the features in the 50 and 90kOe responses

which are much sharper. All of the dielectric responses reach a constant value of ~24 at 43K.

(iii) H//b

The largest dielectric constants were observed when magnetic fields were applied parallel to the *b*-axis. Measurements were taken for 10, 30, 50, 70 and 90kOe fields, the results are shown in Fig.4.4(b). The 10kOe dielectric response exhibits the two features observed in the zero field data. The gradient of the step-like jump is shallower in this case and only reaches a dielectric constant value of ~31. The dielectric constant of the second feature, however, is slightly higher than the value reached in zero field. This trend continues with increasing magnetic field: the maximum value of the dielectric constant steadily increases reaching a value of ~73 in a 90kOe field. The stronger magnetic fields also shift this feature to higher temperatures: the feature positioned at ~16K in zero field occurs at ~22K in a 90kOe field. The step-like jump is not present in the 30-90kOe responses, however, a small feature is observed in the 90kOe response at ~4K. All of the dielectric responses converge to a constant value at ~43K.

(iv) H//c

The dielectric response, shown in Fig.4.4(c) was measured when 10, 20, 30, 50 and 90kOe magnetic fields were applied parallel to the *c*-axis. At 2K, the zero and 10kOe responses have a dielectric constant value of ~27. This value is lowered as the magnetic field is increased. The 20kOe response has an initial dielectric constant of ~24 and the 30-90kOe responses have an initial value of ~22. Both features observed in the zero field data are present in the high field dielectric responses. As the magnetic field is increased, the step-like jump, which disappears for fields greater than 10kOe along the *a* and *b*-axes, becomes less defined. The dielectric constant of this feature decreases from ~33, in zero field, to ~27 in a 90kOe field. The temperature of the feature increases with strengthening field, reaching ~13K in a 90kOe field. The peak in the response, the second feature, follows a similar pattern to the step-like jump: as the field is increased, the dielectric constant decreases and the peak moves to higher temperatures. A large change in dielectric constant occurs when the field applied along the *c*-axis is increased to 20kOe: the feature shrinks from a dielectric constant value of ~61, in a 10kOe field, to ~42. This change in dielectric constant is not as large for higher fields. Application of a 90kOe field produces a different response than lower

fields, a small increase in the dielectric constant occurs when the field is increased from 50kOe to 90kOe. A constant value of ~24 is reached in all the responses at temperatures above 40K.

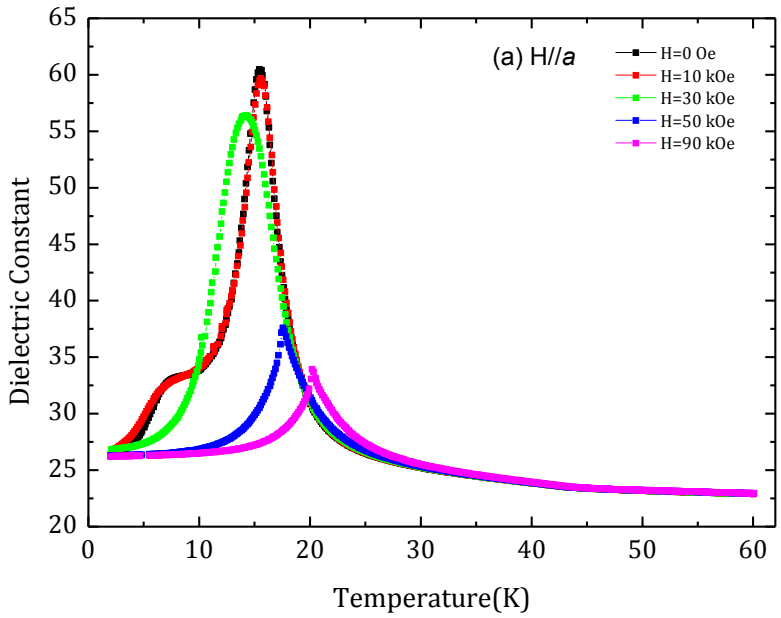

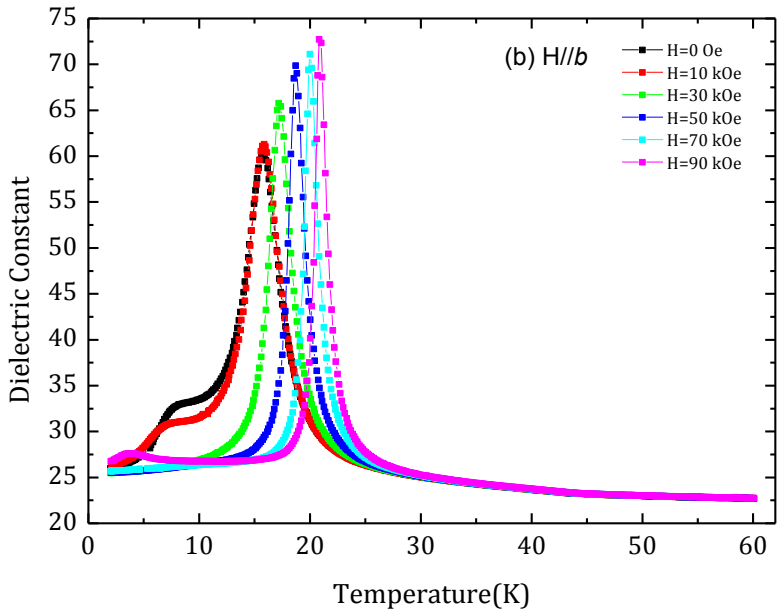

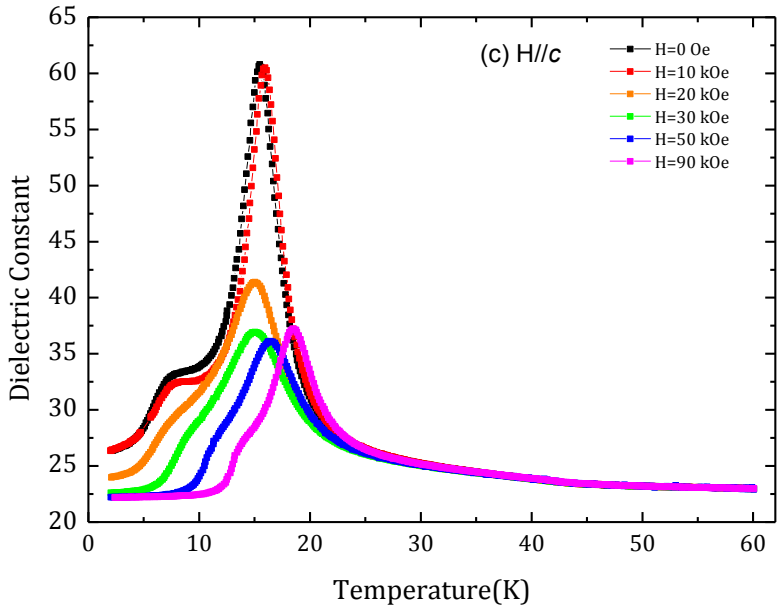

Fig. 4.4: Dielectric response measured along the a-axis as a function of temperature for single crystal $Gd_{0.9}Lu_{0.1}MnO_3$. Measured at 10kHz in magnetic fields applied along the (a) *a*, (b) *b* and (c) *c*-axis.

4.5 Polarisation

The ferroelectric properties of the $Gd_{0.9}Lu_{0.1}MnO_3$ single crystal were investigated by measuring the change in the electric polarisation of the crystal with temperature. The polarisation along the crystallographic *a*-axis was calculated from the pyroelectric current of the sample measured as a function of time. Data was collected from the same oriented sample used to measure the dielectric constant. The experimental method used to determine the polarisation is described in Section 2.6.2(ii). Using the PPMS, magnetic fields of up to 90kOe were applied along each of the *a*, *b* and *c*-axes, enabling a full study of the anisotropic behaviour of the polarisation along the *a*-axis.

Using the same electrical contacts made for the dielectric constant measurements, a voltage of $+220 Vmm^{-1}$ was applied across the sample before cooling, poling the crystal in an electric field. The sample was then cooled in a magnetic field from 60K to 5K at a rate of 3K/min. At 5K, the applied voltage was removed. In order to expel any surface charge built up from application of the electric field, the sample was left connected to a bleed resistor for 15 minutes. The pyroelectric current as a function of time was then measured as the sample was heated to 60K at a sweeping rate of 2K/min. The resulting electrical polarisation is shown in Fig.4.5.

(i) Zero field

A small spontaneous polarisation is observed along the crystallographic *a*-axis in zero magnetic field. $Gd_{0.9}Lu_{0.1}MnO_3$ enters a ferroelectric state below 16K. At ~12K, the state reaches a maximum polarisation of ~200μC/m^2. The shape of the feature indicates that this state may disappear below 5K. Above 16K, the polarisation falls to zero and $Gd_{0.9}Lu_{0.1}MnO_3$ enters a paraelectric state.

(ii) H//a

The ferroelectric response of $Gd_{0.9}Lu_{0.1}MnO_3$ was measured when 10, 30, 50 and 90kOe magnetic fields were applied parallel to the *a*-axis, the results are shown in Fig.4.5(a). A polarisation, similar to that observed in zero-field, occurs in a 10kOe field: a ferroelectric state is induced below 16K and a maximum polarisation of ~245μC/m^2 is recorded at ~12K. A small spontaneous polarisation also occurs in higher magnetic fields, however, the maximum value of the polarisation decreases with increasing field strength, i.e. P=~130μC/m^2 in a 30kOe field and ~55μC/m^2 in a 90kOe field. From the polarisation data in a 30kOe field, $Gd_{0.9}Lu_{0.1}MnO_3$ is paraelectric above 15K. In general, the temperature at which $Gd_{0.9}Lu_{0.1}MnO_3$ enters the ferroelectric state increases with increasing magnetic field. The temperature of the transition from a paraelectric to a ferroelectric state increases from ~18K to above 20K when the field is increased from 50 to 90kOe. As with the zero field response, the polarisation appears to fall close to zero below 5K for all of the field measurements.

(iii) H//b

The largest ferroelectric response was recorded when magnetic fields are applied parallel to the *b*-axis, shown in Fig.4.5(b). $Gd_{0.9}Lu_{0.1}MnO_3$ is strongly ferroelectric in magnetic fields of 20kOe and above. At 5K, a polarisation of over 800μC/m^2 is recorded in a 20kOe field. The polarisation increases with increasing magnetic field reaching a value of ~1250μC/m^2 for a 90kOe field. A spontaneous polarisation of ~400μC/m^2 is also observed in a 10kOe field, however, the ferroelectric state is suppressed below 5K. The temperature of the ferroelectric state is highly dependant on field. A steady increase of the paraelectric-ferroelectric transition temperature is observed as the field

is increased from 0 to 90kOe. Strong fields induce a ferroelectric response within $Gd_{0.9}Lu_{0.1}MnO_3$ at temperatures above 20K.

(iv) H//c

Magnetic fields of 10, 20, 30, 50 and 90kOe were applied parallel to the *c*-axis. The results for fields applied along this direction are shown in Fig.4.5(c). The spontaneous polarisation recorded in zero field is enhanced when a 10kOe field is applied, reaching a maximum value of ~300μC/m². Higher fields suppress the value of the polarisation. The ferroelectric state in $Gd_{0.9}Lu_{0.1}MnO_3$ vanishes when the field reaches a magnitude of 30kOe. A very small feature is observed in the polarisation when a field of 50kOe is applied, this feature becomes more pronounced as the field is increased reaching a maximum value of ~40μC/m² for a 90kOe field. The temperature of the ferroelectric state in the 10, 20 and 30kOe fields is very similar to the zero field response, only the 90kOe field moves the transition to a noticeably higher temperature, ~18K.

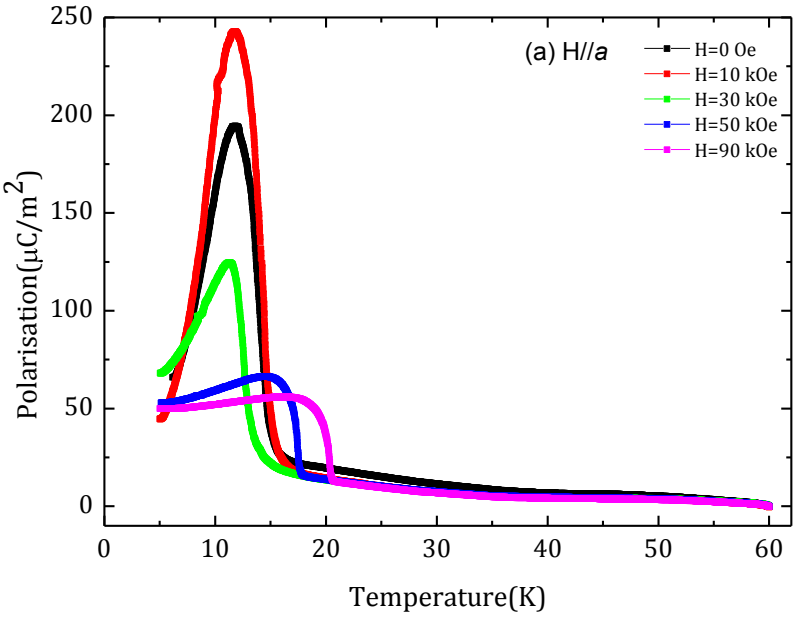

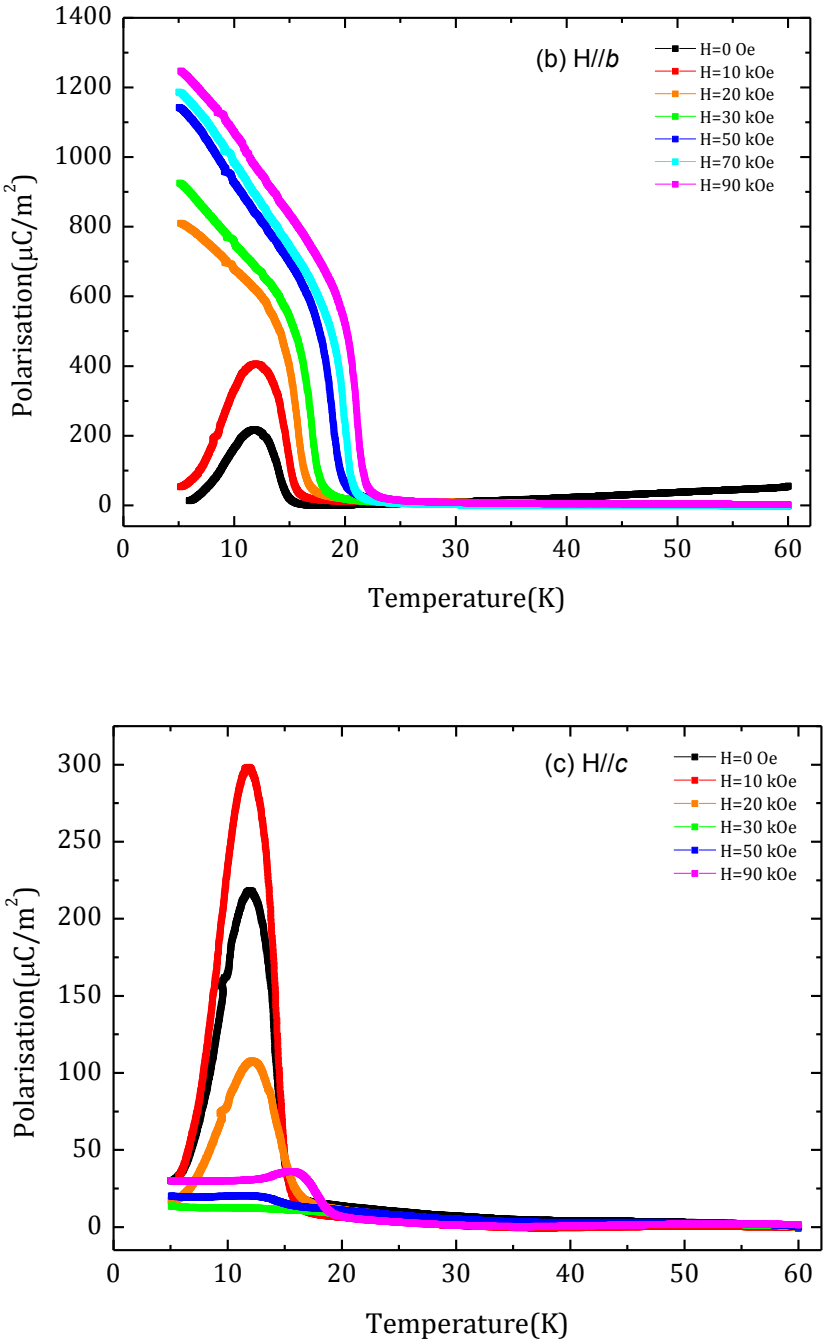

Fig. 4.5: Polarisation measured along the a-axis as a function of temperature for single crystal $Gd_{0.9}Lu_{0.1}MnO_3$. Measured at 10kHz in magnetic fields applied along the (a) *a*, (b) *b* and (c) *c*-axis.

(a)

4.5 Discussion

In order to understand the effect of Lu-doping at the rare-earth site of $GdMnO_3$, the results published by Kimura et al. [33], Hemberger et al. [34, 32], Feyerherm et al. [45] and Noda et al. [46] for pure and Tb-doped $GdMnO_3$ as well as Y-doped $EuMnO_3$ are initially summarised. The experimental results obtained as part of this work are then compared with the published data.

(i) $GdMnO_3$

Using the magnetoelectric phase diagram proposed by Kimura et al. [33], the spin and charge ordering states observed in $GdMnO_3$ are summarised.

Ordering of the Mn moments, T_{Mn}, from a paramagnetic to an incommensurate (IC) antiferromagnetic (AF) state is found to occur at ~43K within $GdMnO_3$. The dielectric constant data published by Kimura et al. shows a change in the gradient at this temperature. Below T_{Mn}, the Mn moments develop a sinusoidal magnetic spin structure which propagates along the *b*-axis. Any FM components that exist within the Mn structure are macroscopically averaged out. Consequently, a net magnetic polarisation of the Gd sites cannot be induced by the sinusoidal structure of the Mn spins. The Gd sublattice therefore remains paramagnetically ordered below T_{Mn}. The magnetisation data for $GdMnO_3$ do not show an anomaly at T_{Mn} when magnetic fields are applied both parallel and perpendicular to the *c*-axis. Heat capacity measurements of $GdMnO_3$, conducted by Hemberger et al. [34], show a well defined feature, largely independent of external magnetic field, close to 40K. These observations confirm the onset of an IC AF spin structure with zero net FM moment. No features are observed in the polarisation data at this temperature as $GdMnO_3$ is paraelectric within this sinusoidally ordered state.

Decreasing the temperature from T_{Mn}, the dielectric constant of $GdMnO_3$ begins to increase with a steep rise towards a maximum at ~23K. The magnetoelectric phase diagram, reported by Kimura et al. [33], shows $GdMnO_3$ to enter a canted AF state at this temperature. Hemberger et al. [34] also describe the Mn moments as entering a canted A-type AF phase with a small FM component oriented along the *c*-axis. This spin canting results in the antiferromagnetic alignment of the Gd moments with the internal field of the Mn moments. As the FM component of the Gd spins is stronger than the FM

component of the Mn spins, the Gd moments are directed parallel to the external magnetic field. Below 23K, the dielectric constant drops to lower values. As the temperature is lowered, a further anomaly is observed below 10K. The dielectric constant exhibits a step-like increase towards lower temperatures showing two features at ~8 and ~5K. These features coincide with the weak spontaneous electric polarisation observed along the *a*-axis. Kimura et al. have attributed this spontaneous ferroelectric state to a minor long-wavelength nearly-lock-in AF phase. The polarisation which developed at 8K becomes suppressed below 5K. Using ac-susceptibility data, Kimura et al. recorded a Gd moment ordering temperature, T_{Gd}, of ~5.1K. At T_{Gd}, the Gd sublattice sets up an additional canted antiferromagnetic (Gd-Gd) ordering with a ferromagnetic (FM) component antiparallel to the FM moment of the canted Mn spins. The canted Mn and Gd structures are AF coupled. This long-range ordering of the Gd moments appears to suppress the ferroelectric state. Below T_{Gd} , $GdMnO_3$ becomes paraelectric and renters the canted AF sate.

Application of an external magnetic field along the *a*, *b* and *c*-axes alters both the position and shape of the features in the dielectric response and the polarisation along the *a*-axis. In general, the temperature of the IC AF - A-type AF transition increases with increasing field strength, of which, the most prominent dependence occurs when H is parallel to the *c*-axis. The dielectric constant develops a secondary step-like feature between the IC AF and canted AF states when a field is applied along the *c*-axis. This feature is accompanied by a small anomaly in the polarisation data which is suppressed at the canted AF ordering temperature. Below 10K, the final anomaly in the dielectric constant vanishes when magnetic fields are applied along either the *a* or *c*-axes. When a field is applied along the *b*-axis, the feature marking the onset of the electric polarisation remain, however, it is suppressed and shifted to higher temperatures as H is increased. The small feature which occurs at ~5K in zero field measurements appears to vanish when the magnetic field is applied. Hemberger et al. [34] observed a reduction in the canting angle of the Gd spins when external fields of 10kOe and above were applied. The Gd ordered state becomes suppressed as the full Gd moment aligns along the direction of the external magnetic field. From the polarisation data, the ferroelectric state is no longer spontaneous and persists below 2K. Both the ferroelectric transition temperature and the maximum value of the polarisation increase with increasing magnetic field. The magnetoelectric phase diagram proposed by Kimura et al. [33] suggests a ferroelectric phase with a polarisation along the *a*-axis induced by a magnetic field along the *b*-axis (Fig.1.17).

A later paper by Feyerherm et al. [45] suggests a slightly different origin for the ferroelectric state in pure $GdMnO_3$. X-ray resonant magnetic scattering has been used to build a picture of the ferroelectric phase in pure $GdMnO_3$. Feyerherm et al. confirm the antiferromagnetic ordering of the nearest neighbour Gd spins along the *c*-axis in zero field previously suggested by Hemberger et al. [34]. They also confirm that this ordering becomes ferromagnetic when an external magnetic field greater than 10kOe is applied along the *b*-axis. The zero field low temperature transitions reported by Kimura et al. [33] around the Gd ordering temperature have also been observed. In contrast with Kimura et al, Feyerherm et al. have assigned the upper transition, at ~8K, to the long-range ordering of the Gd moments and the lower transition, at T*=~5K, to a modification of the magnetically ordered Gd structure. In this case, the Gd ordering coincides with the spontaneous ferroelectric state. Ferroelectricity in $GdMnO_3$ is assumed to have the same origin as $TbMnO_3$ where the spiral ordering of the Mn moments, not the Gd moments, induces the ferroelectric state. Feyerherm et al., however, suggest that a specific field modified Gd moment arrangement is also related to the occurrence of ferroelectricity in $GdMnO_3$. A significant interplay between the Gd and Mn ordering at low temperatures has previously been reported by Hemberger et al. From these observations Feyerherm et al. have suggested a brief cycloidal ordering of the Mn moment between T_{Gd} and T*. Below T* the ordering is believed to become unstable and so disappears. The change in Gd ordering that occurs when an external magnetic field is applied along the *b*-axis may stabilize this cycloidal ordering of the Mn moments leading to the observed ferroelectricity in $GdMnO_3$. The ordering of the Mn moments are still directly responsible for the electric polarisation but the Gd moments are important in stabilizing the ferroelectric state in $GdMnO_3$.

(i) $Gd_{1-x}Tb_xMnO_3$

The effect of doping at the rare earth site on the ferroelectric phase of $GdMnO_3$ has been investigated by Noda et al. [46]. The polarisation and dielectric properties of $Gd_{1-x}Tb_xMnO_3$ single crystals were investigated as a means to clarify the crossover between the two distinct $GdMnO_3$ and $TbMnO_3$ phase diagrams. The publication drew a different conclusion to Kimura et al. [33] on the origin of the ferroelectric state in pure $GdMnO_3$. Doping levels of x=0, 0.1, 0.3, 0.4, 0.5 and 1 where achieved and a compositional phase boundary between $GdMnO_3$ and $TbMnO_3$ was found to exist around a doping level of $0.3<x<0.4$. A similar phase boundary was achieved within

$Gd_{0.9}Tb_{0.1}MnO_3$ when external magnetic fields of 30-40kOe where applied along the *b*-axis. Noda et al. observed the procession of two different ferroelectric states, FE1 and FE2, within $Gd_{1-x}Tb_xMnO_3$. An electric polarisation along the *a*-axis was detected for both the x=0 and 0.3 crystals in zero field. The ferroelectric state in pure $GdMnO_3$, FE1, is believed to originate from the magnetic ordering of the Gd moments whereas the ferroelectric state in $Gd_{0.7}Tb_{0.3}MnO_3$ is attributed to the spiral ordering of the Mn spins found in $TbMnO_3$. Noda et al. found that the ferroelectric state in pure $GdMnO_3$ disappeared if the crystal was not cooled to temperatures below 6K, the Gd ordering temperature. No such dependence was found for $Gd_{0.7}Tb_{0.3}MnO_3$.

Investigation into the field-effect for $Gd_{0.9}Tb_{0.1}MnO_3$ saw the re-emergence of the FE1 state when a field above 20kOe was applied along the *b*-axis. The transition temperature for this state, in zero field, is thought to occur at a very low temperature. Application of a magnetic field is believed to shift this transition to higher, attainable, temperatures. FE2, a ferroelectric state similar to that observed in $Gd_{0.7}Lu_{0.3}MnO_3$ is also induced within $Gd_{0.9}Tb_{0.1}MnO_3$ for fields above 40kOe. The polarisation measurements show two successive phase transitions: an abrupt jump around the sinusoidal AF-spiral AF transition temperature, found in $TbMnO_3$ which corresponds to the FE2 phase followed by a gradual increase around 15K corresponding to the FE1 phase. From their observations, Noda et al. [46] suggest a coexistence of both FE1 and FE2 states for $Gd_{0.9}Tb_{0.1}MnO_3$ in a magnetic field. The complex nature of the phase changes in $Gd_{0.9}Tb_{0.1}MnO_3$ expel the belief of a simple systematic change from $GdMnO_3$ to $TbMnO_3$ character.

(iii) $Eu_{1-x}Y_xMnO_3$

Hemberger et al. [32], in a more recent paper, have investigated the effect of doping with non-magnetic Y on the ferroelectric properties of $EuMnO_3$. They found that for low doping concentrations, $x<0.15$, $Eu_{1-x}Y_xMnO_3$ exhibits the same magnetoelectric ordering as pure $EuMnO_3$. For high concentrations, $x\geq3$, $Eu_{1-x}Y_xMnO_3$ has a phase diagram similar to $TbMnO_3$ where the Mn moments show a sinusoidal AF-spiral AF transition between 20 and 30K, depending on the doping level. The orientation of the polarisation changes from $GdMnO_3$-like (*a*-axis) to $TbMnO_3$-like (*c*-axis) with increasing *x* [33]. A concentration of $x\sim0.2$ was expected to reproduce the properties of pure $GdMnO_3$, however, $Eu_{0.8}Y_{0.2}MnO_3$ was found to have both a weak ferromagnetic moment and a relatively large polarisation, $\sim500\mu C/m^2$, in zero magnetic field. Hemberger et al.

concluded that $Eu_{0.8}Y_{0.2}MnO_3$ enters a spiral AF state at ~30K followed by a possible canted spiral AF state at ~22K which combines both of the observed finite spontaneous magnetic moment and ferroelectricity. The development of this new magnetic phase lead Hemberger et al. to suggest that the role of the magnetic rare earth is restricted to the distortion of the magnetic structure connected with the magnetic A-site ordering at low temperature. The modulation of the magnetic structure related to the onset of ferroelectricity is only realized by the Mn sublattice. Hemberger et al. also point out the importance of disorder effects caused by the doping. This disorder may influence the properties of $Eu_{0.8}Y_{0.2}MnO_3$.

(iv) $Gd_{1-x}Lu_xMnO_3$ – Present Study

Lu^{3+} has a smaller ionic radius than Gd^{3+}, 0.861Å and 1.04Å respectively. Doping with Lu decrease the R site volume of $GdMnO_3$ altering its properties. The Rietveld refinement preformed on the polycrystalline $Gd_{0.9}Lu_{0.1}MnO_3$ sample estimated an average Mn-O-Mn bond angle, φ, of 145.39(78)°. The average Mn-O-Mn bond angle of the $Gd_{0.9}Lu_{0.1}MnO_3$ single crystal was previously estimated by Liao et al. [47] using single crystal x-ray diffraction data. An average Mn-O-Mn bond angle of 145.16(1)° was estimated for the crystal. This is smaller than the Mn-O-Mn bond angle in $GdMnO_3$, φ=145.60(9)°[47].

Initially, the phase transitions observed by Kimura et al. [33] in $GdMnO_3$ were thought to be the same for $Gd_{0.9}Lu_{0.1}MnO_3$. From the heat capacity data reported in this thesis, a Mn moment ordering temperature similar to that observed in $GdMnO_3$ was recorded for $Gd_{0.9}Lu_{0.1}MnO_3$. However, the features in the dielectric constant reported by Kimura et al. for pure $GdMnO_3$ and those observed in this thesis for $Gd_{0.9}Lu_{0.1}MnO_3$ become dissimilar below the IC ordering temperature. The paraelectric canted state expected of $GdMnO_3$ is not present in the magnetisation or dielectric constant data presented here for $Gd_{0.9}Lu_{0.1}MnO_3$. The reduced Mn-O-Mn bond angle positions Lu-doped $GdMnO_3$ closer to $TbMnO_3$ (φ=145.26(4)°) in the magnetoelectric phase diagram (Fig.1.17, Introduction). $Gd_{0.9}Lu_{0.1}MnO_3$ is therefore expected to exhibit multiferroic properties similar to that of $TbMnO_3$. The correlation between the features in the heat capacity, dielectric constant and polarisation in zero magnetic field and the magnetisation in a 1kOe field are summarised in Fig.4.6.

Low level doping with Lu is believed to produce a crossover between the $GdMnO_3$ and $TbMnO_3$ states. Although Tb has a larger ionic radius than Lu, a Mn-O-Mn bond angle similar to $Gd_{0.9}Lu_{0.1}MnO_3$ can be achieved within $Gd_{1-x}Tb_xMnO_3$, a comparison can therefore be made between the two doped compounds. The dielectric response and polarisation results reported by Noda et al. [46] for $Gd_{0.9}Tb_{0.1}MnO_3$ along the *a*-axis when a magnetic field of 40kOe is applied along the *b*-axis, are similar to that measured in $Gd_{0.9}Lu_{0.1}MnO_3$. This similarity may suggest the existence of two separate ferroelectric states in $Gd_{0.9}Lu_{0.1}MnO_3$ similar to the FE1 and FE2 states proposed by Noda et al. for $Gd_{1-x}Tb_xMnO_3$.

An explanation similar to that suggested by Feyerherm et al. [45] for the onset of ferroelectricity within $GdMnO_3$ may also be applied to $Gd_{0.9}Lu_{0.1}MnO_3$. As discussed in Section 4.5, $Gd_{0.9}Lu_{0.1}MnO_3$ enters a spontaneous ferroelectric state at ~ 16K which decreases below ~12K in zero-field. The dielectric constant shows a plateau in the data at this temperature followed by a continuous decrease in the dielectric value below ~7K. In addition, heat capacity measurements for $Gd_{0.9}Lu_{0.1}MnO_3$ show a minimum in the data around 13K followed by a broad peak at ~6K. Using Feyerherm et al.'s theory the following scenario is suggested for $Gd_{0.9}Lu_{0.1}MnO_3$: at ~16K, the Mn moments in $Gd_{0.9}Lu_{0.1}MnO_3$ develop a spiral magnetic spin structure similar to $TbMnO_3$. Below ~12K, the spin structure of the Mn moments changes as a result of the long-range ordering of the rare earth ion. In pure $GdMnO_3$, long range ordering of the Gd moments occurs around 8K. The Gd moments interact with the Mn moments changing the magnetic ordering of Mn moments from a spiral spin structure to cycloidal spin structure. This cycloidal ordering is both time and spatially invariant allowing for the ferroelectric state to persist. Below 7K the Gd magnetic structure is altered, the cycloidal ordering becomes unstable and the ferroelectric state disappears.

A similar explanation can be applied for magnetic fields applied along the *c*-axis. The dielectric constant results show the same features observed in the zero field measurement. In particular, the 90kOe measurements show $Gd_{0.9}Lu_{0.1}MnO_3$ to enter a brief ferroelectric phase at ~18K. The Mn moments are believed to form a spiral spin structure at this temperature which evolves into a cycloidal ordering at ~16K, the ordering temperature of the Gd moments. A sharp decrease in the dielectric constant at ~13K is accompanied by the loss of polarisation. The change in magnetic structure of the Gd moments at this temperature weakens the cycloidal ordering and therefore extinguishes the ferroelectric state.

The low temperature feature assigned to the destabilisation of the cyclodial Mn ordering is not observed when magnetic fields greater than 20kOe are applied along the *b*-axis. The dielectric constant data shows a peak at the spiral ordering temperature of the Mn moments followed by a feature similar to that observed at ~12K in the zero-field measurement. The corresponding polarisation data also shows a change in shape at this temperature. A specific field modified ordering of the Gd moments is believed to occur at this temperature which is accompanied by a cycloidal ordering of the Mn moments. The field dependant Gd ordering stabilises the ferroelectric state allowing it to persist below the 7K.

When magnetic fields are applied along the *a*-axis, the low temperature feature observed in zero field disappears. As the field is increased, the dielectric constant takes a similar form to the *b*-axis magnetic field measurements. Although the polarisation is small it does not appear to fall to zero as is the case when magnetic fields are applied along the *c*-axis. The polarisation reaches a maximum at the Gd ordering temperature where the spiral Mn order changes to a cycloid. The field-induced Gd ordering appears to stabilise the cycloidal ordering, however, it is much weaker than the cycloidal ordering induced as a result of magnetic fields applied along the *b*-axis. This weakening of the ferroelectric Mn ordering may explain the slight decrease in polarisation below the spiral-cyclodial transition temperature.

The magnetoelectric phase transitions proposed for $Gd_{0.9}Lu_{0.1}MnO_3$ are based on the conclusions of both Noda et al. [46] and Feyerherm et al. [45]. Both papers cite the importance of the long range ordering of the Gd moments on the ferroelectric state in $GdMnO_3$, however, they are in dispute of the exact origin of the state. Noda et al. associate the state with the ordering of the Gd moments whereas Feyerherm et al. suggest an ordering of the Mn moments influenced by the Gd ordering. Feyerherm et al's suggestion is more in keeping with theoretical results and the ferroelectric states observed in other orthorhombic rare earth manganites. As demonstrated by Hemberger et al. [34] $GdMnO_3$, like $DyMnO_3$, shows a magnetic coupling between the rare earth and Mn ions at low temperatures. Structural distortions caused by interference between the rare earth and Mn ions have also been observed within the series. It is important to point out that unlike Tb, Lu is non magnetic, consequently, the effect of R-site volume on the multiferroic phase of $GdMnO_3$ can be observed without influence from an additional magnetic moment caused by doping with a magnetic rare-

earth ion. The effect of magnetic ordering of the Tb moments on the multiferroic properties of lightly doped $GdMnO_3$ has not been discussed by Noda et al. Doping with magnetic Tb will have a different effect on the Gd ordering than non-magnetic Lu. In order to draw similar conclusions as Noda et al., $Gd_{0.9}Lu_{0.1}MnO_3$ must be compared with another non-magnetically doped member of the orthorhombic manganite series.

The influence of the ordering of the Gd moments on the ferroelectric state in $Gd_{0.9}Lu_{0.1}MnO_3$, should be reconsidered in light of Hemberger et al.'s [32] observation in Y doped $EuMnO_3$. As previously explained, doping with non-magnetic Lu allows for a systematic variation of the ionic radii and the Mn-O-Mn angle without the additional influence of a magnetic rare-earth moment. The long-range ordering of the rare earth ions are expected to be unaltered by a non-magnetic dopant. The Gd ordering temperature in $Gd_{0.9}Lu_{0.1}MnO_3$ should therefore be similar to that of pure $GdMnO_3$. The features observed at 12K, initially thought to be the Gd ordering temperature, may result from a change in the magnetic structure of the Mn system caused purely by a change in the R-site volume and uninfluenced by any rare-earth ordering. The Mn moments may then acquire a new ferroelectric type ordering, not observed in pure $GdMnO_3$, below this temperature. No features are observed in the magnetisation therefore the canted spiral AF state observed for $Eu_{0.8}Y_{0.2}MnO_3$ is not expected to occur in $Gd_{0.9}Lu_{0.1}MnO_3$. The feature around 6K may result from the ordering of the Gd moments. The heat capacity results show a broad peak at this temperature similar to that observed by Hemberger et al. [34] for pure $GdMnO_3$. The magnetisation results for $Gd_{0.9}Lu_{0.1}MnO_3$ show a cusp like feature at this temperature in low fields. The Gd lattice is expected to induce an additional AF ordering at the Gd ordering temperature in low fields.

A number of different theories can be deduced from the results obtained from the $Gd_{0.9}Lu_{0.1}MnO_3$ single crystal. This report only covers a small number of possible experiments needed to determine an accurate magnetoelectric phase diagram.

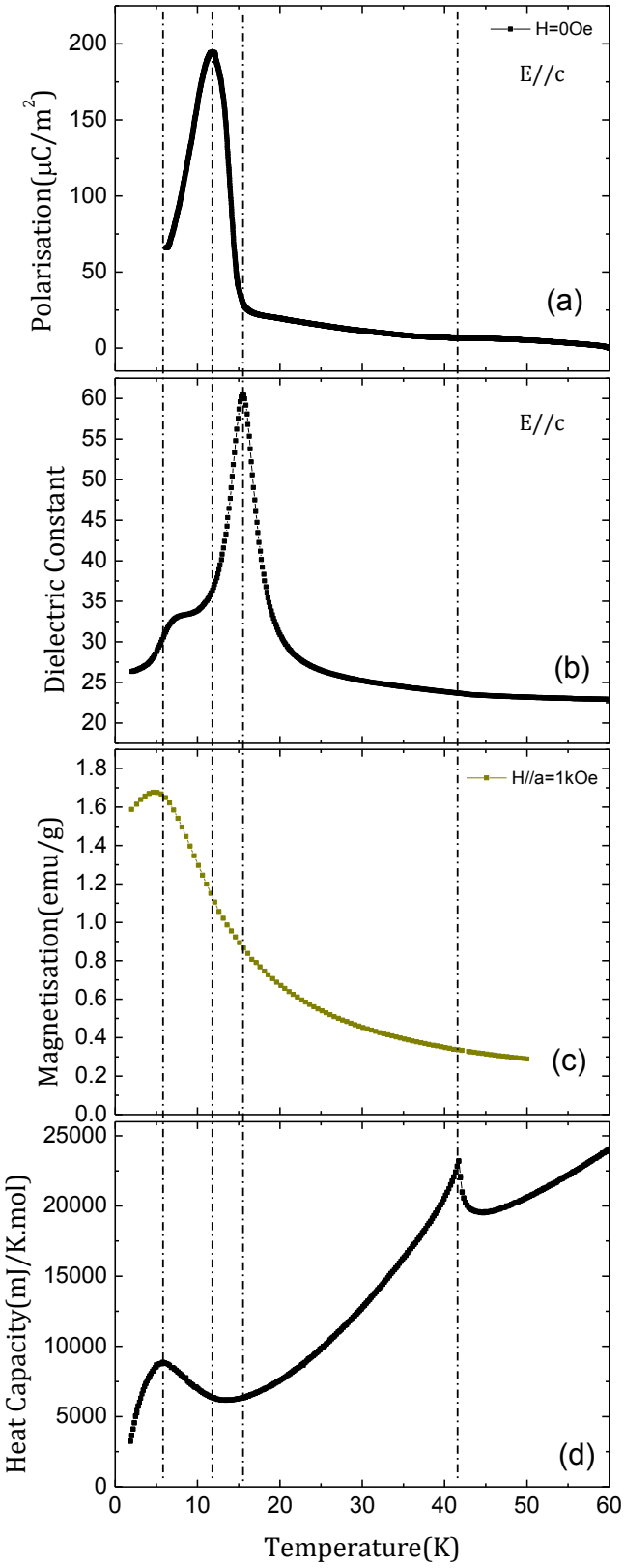

Fig. 4.6: (a) Polarisation and (b) dielectric constant measured along the *a*-axis of single crystal $Gd_{0.9}Lu_{0.1}MnO_3$ in zero magnetic field. (c) FC magnetisation in a 1kOe magnetic field applied along the *a*-axis and (d) heat capacity measured in zero applied field.

4.6 Conclusion

A study investigating the magnetic and electric properties of an oriented single crystal of $Gd_{0.9}Lu_{0.1}MnO_3$ has been presented.

Doping with Lu at the rare-earth site of orthorhombic $GdMnO_3$ (φ=145.60(9)°) has been found to alter the properties of the parent compound. A Mn-O-Mn bond angle of 145.16(1)° was previously estimated by Liao et al. for the $Gd_{0.9}Lu_{0.1}MnO_3$ single crystal. The reduced Mn-O-Mn bond angle positions the Lu-doped $GdMnO_3$ closer to multiferroic $TbMnO_3$ (φ=145.26(4)°) in the spin ordering phase diagram. The close proximity to the spiral magnetic ordering/ferroelectric state observed in $TbMnO_3$ has created a number of unique features in the experimental results of the $Gd_{0.9}Lu_{0.1}MnO_3$ single crystal.

Ordering of the Mn moments attributed to a transition from a paramagnetic to sinusoidal incommensurate antiferromagnetic state is observed in the heat capacity of single crystal $Gd_{0.9}Lu_{0.1}MnO_3$ at 41.7K. The single crystal is found to enter a spontaneous ferroelectric state below 16K along the crystallographic *a*-axis. A feature in the dielectric constant indicative of a spiral AF ordering of the Mn moments is also observed at this temperature. A ferroelectric state is present in all the polarisation data collected for magnetic fields applied along each of the *a*, *b* and *c*-axes. The multiferroic state previously observed in $GdMnO_3$ along the *a*-axis when magnetic fields are applied along the *b*-axis is enhanced in the lightly doped crystal. The absence of a canted A-type AF state in the magnetisation, normally present for the parent compound, and the persistence of a ferroelectric state in the polarisation data allow for the suggestion of a new magnetically ordered ferroelectric state, influenced by the ordering of the Gd moments, to occur within $Gd_{0.9}Lu_{0.1}MnO_3$.

4.7 Further Work

In order to analyse the results and interpret the features in the data, reference has been made to published pure and Tb-doped $GdMnO_3$ and Y-doped $EuMnO_3$ data. Ideally additional measurements such as neutron diffraction and x-ray resonant scattering should be carried out to accurately determine the magnetic spin structures that occur in the single crystal. X-ray resonant scattering would be the preferred technique as Gd

is a highly absorbing nucleus for neutrons. In order to complete the magnetoelectric phase diagram, dielectric constant and polarisation measurements should be carried out along the *b* and *c*-axes in zero and applied magnetic fields. Heat capacity measurements in magnetic fields applied along each of the crystallographic axes should also be carried out in order to complete thermal analysis of the crystal.

The work completed as part of this thesis will supplement a larger paper on the structural, magnetic and dielectric properties of polycrystalline and single crystal $Gd_{1-x}Lu_xMnO_3$ ($x \leq 0.2$) currently in preparation.

References

[1] S.-W. Cheong and M. Mostovoy, Nature Materials **6**, p13-20 (2007).

[2] M.A. Subramanian, T. He, J. Chen, N.S. Rogado, T.G. Calvarese and A.W. Sleight, Adv. Mater. **18**, 1737-1739 (2006).

[3] N. Ikeda, H. Ohsumi, K. Ishii, T. Inami, K. Kakurai, Y. Murakami, K. Yoshii, S. Mori, T. Horibe and H. Kitô, Nature **436**, 25(2005).

[4] M. Fiebig, J. Phys. D: Appl. Phys. **38,** R123-152 (2005).

[5] H. Schmid, Multiferroic Magnetoelectrics, Ferroelectrics **162**, 317.

[6] S. Blundell, *Magnetism in Condensed Matter*, Oxford Master Series in Condensed Matter Physics.

[7] D.I. Khomskii, Journal of Magnetism and Magnetic Materials **306**, p1-8 (2006).

[8] W. Eerenstein, N.D. Mathur and J.F. Scott, Nature **442**, p759-765 (2006).

[9] S. Picozzi and C. Ederer, J. Phys.: Condens. Matter **21**, 303201 (2009).

[10] D. O'Flynn, Ph.D. thesis, University of Warwick (2010).

[11] H.Lewtas, Ph.D. thesis, University of Oxford (2010).

[12] J. van der Brink and D.I. Khomskii, J.Phys.: Condens. Matter **20**, 434217 (2008).

[13] J. Iida, S. Takekawa and N. Kimizuka, Journal of Crystal Growth **102**, p398-400 (1990).

[14] N. Ikeda, J. Phys.: Condens. Matter **20**, 434218 (2008).

[15] Y. Yamada, K. Kitsuda, S. Nohdo and N. Ikeda, Phys. Rev. B **62**, 18 (2000).

[16] K.-T. Ko, H.-J. Noh, J.-Y. Kim, B.-G. Park, J.-H. Park, A. Tanaka, S.B. Kim, C. L. Zhang and S.-W. Cheong, Phys. Rev. Lett. **103**, 207202 (2009).

[17] N. Ikeda, K. Kohn, N. Myouga, E. Takahashi, H. Kitôh and S. Takekawa, J. Phys. Soc. Jpn. **69**, 5 p1526-1532 (2000).

[18] A.D. Christianson, M.D. Lumsden, M. Angst, Z. Yamani, W. Tian, R. Jin, E.A. Payzant, S.E. Nagler, B.C. Sales and D. Mandrus, Phys. Rev. Letts. **100**, 107601 (2008).

[19] M. Angst, R.P. Hermann, A.D. Christianson, C. Lee, M.-H. Whangbo, J.-W. Kim, P.J. Ryan, S.E. Nagler, W. Tian, R. Jin, B.C. Sales and D. Mandrus, Phys. Rev. Lett. **101**, 227601 (2008).

[20] X.S. Xu, M. Angst, T.V. Brinzari, R.P. Hermann, J.L. Musfeldt, A.D. Christianson, D.Mandrus, B.C. Sales, S. McGill, J.-W. Kim and Z. Islam, Phys. Rev. Lett. **101**, 227602 (2008).

[21] M. Isobe, N. Kimizuka, J. Iida and S.Takekawa, Acta Cryst. C **46**, 1917-1919 (1990).

[22] J. Iida, M. Tanaka, Y. Nakagawa, S. Funahashi, N. Kimizuke and S. Takekawa, J. Phys. Soc. Jpn. **62**,5, 1723-1735 (1993).

[23] S. Funahashi, J. Akimitsu, K. Siratori, N. Kimizuka, M. Tanaka and H. Fujishita, J. Phys. Soc. Jpn. **53**, 2688-2696 (1984).

[24] W. Wu, V. Kiryukhin, H.-J. Noh, K.-T. Ko, J.-H. Park, W. Ratcliff II, P.A. Sharma, N.Harrison, Y.J. Choi, Y. Horibe, S. Lee, S. Park, H.T. Yi, C.L. Zhang and S.-W. Cheong, Phys. Rev. Lett. **101**, 137203 (2008).

[25] F. Wang, J. Kim, Y.-J. Kim and G.D. Gu, Phys. Rev. B **80**, 024419 (2009).

[26] M.H. Phan, N.A. Frey, M. Angst, J. de Groot, B.C. Sales, D.G. Mandrus and H. Srikanth, Solid State Communications **150**, p341-345 (2010).

[27] T. Michiuchi, Y. Yokota, T. Komatsu, H. Hayakawa, T. Kuroda, D. Maeda, Y. Matsuo, S. Mori, K. Yoshii, N. Hanasaki, T. Kambe and N. Ikeda, Ferroelectrics 378, p175-180 (2009).

[28] J. Kim, S.B. Kim, C. U. Jung and B.W. Lee, IEEE Transactions on Magnetics **45**,6 (2009).

[29] T. Kimura, T. Goto, H. Shintani, K. Ishizaka, T. Arima and Y. Tokura, Nature **426**, 55 (2003).

[30] S. Ishihara, J. Phys. Soc. Jpn **79**, 1 (2010).

[31] T. Kimura, S. Ishihara, H. Shintani, T. Arima, K.T. Takahashi, K. Ishizaka, and Y. Tokura, Phys. Rev. B **68**, 060403 (2003).

[32] J. Hemberger, F. Schrettle, A. Pimenov, P. Lunkenheimer, V. Yu. Ivanov, A.A. Mukhin, A.M. Balbashov and A. Loidl, Phys. Rev. B **75**, 035118 (2007).

[33] T. Kimura, G. Lawes, T. Goto, Y. Tokura and A.P. Ramirez, Phys. Rev. B **71**, 224425 (2005).

[34] J. Hemberger, S. Lobina, H.-A. Krug von Nidda, N. Tristan, V. Yu. Ivanov, A.A. Mukhin, A.M. Balbashov and A. Loidl, Phys. Rev. B **70**, 024414 (2004).

[35] V. Yu. Ivanov, A.A. Mukhin, V.D. Travkin, A.S. Prokhorov, Yu. F. Popov, A.M. Kadomtseva, G.P. Vorob'ev, K.I. Kamilov and A.M. Balbashov, Phys. Stat. Sol. B **243**, 1, 107-111 (2006).

[36] D. O'Flynn, C.V. Tomy, M.R. Lees, A. Daoud-Aladine and G. Balakrishnan, Phys. Rev. B **83**, 174426 (2011).

[37] V.K. Wadhawam, *Introduction to Ferroic Materials*, Gordon and Breach Science Publishers, p.10.

[38] Y. Zhang, H.X. Yang, Y.Q. Guo, C. Ma, H.F. Tian, J.L. Luo and J.Q. Li, Phys. Rev. B **76**, 184105 (2007).

[39] J.Y. Park, J.H. Park, Y.K. Jeong and H.M. Jang, Appl. Phys. Lett. 91, 152903 (2007).

[40] S. Taran, C.C. Chou, J.L. Her, C.P. Sun, C.C. Lin, C.L. Chan, C.L. Huang and H.D. Yang, J. Phys.: Conference Series **150**, 042205 (2009).

[41] K. Yoshii, N. Ikeda, Y. Matsuo, Y. Horibe and S. Mori, Phys. Rev. B **76**, 024423 (2007).

[42] M. Inazumi et al., J. Phys. Soc. Jpn. **50**, 438 (1981).

[43] C.R. Serrao, A.K. Kunda, S.B. Krupanidhi, U.V. Waghmare and C.N.R. Rao, Phys. Rev. B **72**, 220101 (2005).

[44] W.S. Ferreira, J. Agostinho Moreira, A. Almeida, M.R. Chaves, J.P. Araújo, J.B. Oliveira, J.M. Machado Da Silva, M.A, Sá, T.M. Mendonça, P. Simeão Carvalho, J.Kreisel, J.L. Ribeiro, L.G. Vieira, P.B. Tavares and S. Mendonça, Phys. Rev. B **79**, 054303 (2009).

[45] R. Fayerherm, E. Dudzik, A.U.B. Wolter, S. Valencia, O. Prokhnenko, A. Maljuk, S. Landsgesell, N. Aliouane, L. Bouchenoire, S. Brown and D.N. Argyriou, Phys. Rev. B **79**, 134426 (2009).

[46] K. Noda, S. Nakamura and H. Kuwahara, IEEE Transactions on Magnetics **41**, 10 (2005).

[47] D. Liao, M.R. Lees, D.M. Paul, D.S. Keeble and G. Balakrishnan, (*in preparation to be published*).